Dissertation

DTI-Based Multiscale Models for Glioma Invasion

Alexander Hunt

Vom Fachbereich Mathematik der Technischen Universität Kaiserslautern zur Verleihung des akademischen Grades Doktor der Naturwissenschaften (Doctor rerum naturalium, Dr. rer. nat.) genehmigte Dissertation

Datum der Prüfung: 30.11.2017
Erster Gutachter: Prof. Dr. C. Surulescu
Zweiter Gutachter: Prof. Dr. C. Rohde

Kaiserslautern 2018
(D 386)

Lern im Leben die Kunst, im Kunstwerk lerne das Leben,
Siehst du das Eine recht, siehst du das andere auch.

Friedrich Hölderlin

Acknowledgement

I would like to express my gratitude to my supervisor Prof. Dr. Christina Surulescu for the interesting topic to work on and for plenty of valuable comments and suggestions.

I would also like to thank Prof. Dr. Christian Engwer for invaluable advice with programming in general and the framework of Dune in special.

Further I want to thank my colleagues at the TU Kaiserslautern for rich discussions and a great working atmosphere.

Moreover I appreciate the support of my family and friends over the time, but especially in the last years.

15th August 2018 Alexander Hunt

Abstract

Certain brain tumours are very hard to treat with radiotherapy due to their irregular shape caused by the infiltrative nature of the tumour cells. To enhance the estimation of the tumour extent one may use a mathematical model. As the brain structure plays an important role for the cell migration, it has to be included in such a model. This is done via diffusion-MRI data. We set up a multiscale model class accounting among others for integrin-mediated movement of cancer cells in the brain tissue, and the integrin-mediated proliferation. Moreover, we model a novel chemotherapy in combination with standard radiotherapy.

Thereby, we start on the cellular scale in order to describe migration. Then we deduce mean-field equations on the mesoscopic (cell density) scale on which we also incorporate cell proliferation. To reduce the phase space of the mesoscopic equation, we use parabolic scaling and deduce an effective description in the form of a reaction-convection-diffusion equation on the macroscopic spatio-temporal scale. On this scale we perform three dimensional numerical simulations for the tumour cell density, thereby incorporating real diffusion tensor imaging data. To this aim, we present programmes for the data processing taking the raw medical data and processing it to the form to be included in the numerical simulation. Thanks to the reduction of the phase space, the numerical simulations are fast enough to enable application in clinical practice.

Zusammenfassung

Gehirntumore, insbesondere solche in einem fortgeschrittenen Stadium wie etwa Glioblastoma multiforme, sind sehr schwer mit Radiotherapie zu behandeln, ein Umstand, der von der stark irregulären Ausbreitung und Form dieser Tumoren herrührt. Die Ursache dafür ist die Infiltration des umliegenden Gewebes durch die Tumorzellen. Um deren Ausbreitung besser abschätzen zu können, schlagen wir die Verwendung einer Klasse von mehrskaligen mathematischen Modellen vor. Da die Gehirnstruktur für die Zellbewegung von entscheidender Bedeutung ist, muss sie in einem solchen Modell berücksichtigt werden. Hier werden wir dies unter Verwendung von Diffusions-MRT Daten bewerkstelligen. Wir schlagen einen mehrskaligen Modellierungszugang vor, der unter Anderem die Bewegung der Tumorzellen und Proliferation berücksichtigt, beides initiiert durch die Bindung der Tumorzellen an das umliegende Gewebe. Zudem modellieren wir eine neuartige Chemotherapie, die betreits in klinischen Tests ist oder war und die genau diese Zell-Gewebe Bindungen hemmen soll. Das Therapiemodell ergänzen wir mit der aktuell standardmäßigen Wahl von Radiotherapie, beschrieben durch das LQ-Modell.

Wir starten auf der zellulären Ebene, um Migration zu modellieren, skalieren das resultierende Partikelsystem auf die mesoskopische (Zelldichte-) Skala und inkludieren hier die Proliferation. Um den hochdimensionalen Phasenraum zu reduzieren, setzen wir parabolische Skalierung ein und leiten eine Reaktions-Advektions-Diffusionsgleichung als makroskopisches (nur von Ort und Zeit abhängiges) Modell her. Dieses simulieren wir in 3 Dimensionen auf realen MRT Daten. Dafür präsentieren wir auch Programme, um medizinische Daten für unseren Modellierungszugang aufzubereiten.

Die numerischen Simulationen sind aufgrund der Reduktion des Phasenraumes schnell genug, um relevante Informationen für die klinische Anwendung zu liefern.

Contents

1 Introduction **1**

1.1 Biological background 2

1.2 Outline 3

2 Modelling **7**

2.1 Introduction 7

2.2 Tumour Modelling 8

2.3 Previous Models, State of the Art 10

2.4 Multiscale Models 13

2.4.1 Microscopic Description 13

2.4.2 Mesoscopic Description 20

2.4.3 Modelling Proliferation via Cell-Tissue Interaction 23

2.4.4 From Mesoscopic to Macroscopic Description 25

2.4.5 First Multiscale Model Relying on the Mesoscale Description (2.10) . 26

2.4.6 Second Multiscale Model Relying on the Mesoscopic Description (2.11) 33

2.5 Appendix: Well-posedness theory 39

3 Data **41**

3.1 Information contained in the data 42

3.1.1 Assessment of q 43

3.1.2 Assessment of Q 46

3.1.3 Test cases 48

3.2 Appendix: Data preprocessing in detail 48

3.2.1 Data formats used 49

3.2.2 Software 49

3.2.3 Known problems 50

3.2.4 Example codes 50

4 Numerical simulation **59**
4.1 Introduction . . . 59
4.2 Discretization of the macroscopic equations . . . 60
4.2.1 Discretization of the diffusion term . . . 61
4.2.2 Discretization of the convection term . . . 69
4.2.3 Time stepping . . . 70
4.3 Processing the data . . . 71
4.3.1 The single integral . . . 72
4.3.2 The double integral . . . 72
4.4 Assessing the parameters . . . 74
4.5 Numerical Simulations . . . 75
4.5.1 Implementation . . . 75
4.5.2 Results . . . 77

5 Therapy **91**
5.1 Description . . . 92
5.2 Extracting the macroscopic behaviour . . . 95
5.3 Simulation . . . 99

6 Discussion **105**
6.1 Modelling . . . 105
6.2 Data . . . 107
6.3 Numerics . . . 108
6.4 Therapy . . . 109

List of Figures

3.1 Linear vs. non-linear fit 1 . . . 43
3.2 Linear vs. non-linear fit 2 . . . 44
3.3 FA and Q . . . 48

4.1 Initial condition on slice 26 . . . 78
4.2 Simulations of (2.23) and (2.40) . . . 83
4.3 Difference between 2D and 3D simulations . . . 84
4.4 Difference between semi-implicit and fully implicit calculations . . . 84
4.5 Comparison of different values for λ_1 in (2.23) . . . 85
4.6 Comparison of different values for λ_1 in (2.40) . . . 86
4.7 Simulations of model (2.23) and (4.9) . . . 87
4.8 Difference between (4.9) and (2.23) without subcellular dynamics at time $t = 400$ days . . . 88
4.9 Difference between (4.9) and (2.23) with subcellular dynamics at time $t = 400$ days . . . 88
4.10 Simulation of (2.23) and (4.10) . . . 89
4.11 Comparing ODF to bimodal von-Mises-Fisher . . . 90
4.12 Comparison between model (4.10) to (2.23) with subcellular dynamics . . . 90

5.1 Simulations of (2.23) and (5.5) . . . 102
5.2 Larger initial tumour for therapy . . . 103
5.3 Comparing the therapy strategies . . . 104

List of Tables

4.1 Convergence results for the non-monotone method 69
4.2 Convergence results for the monotone method 69
4.3 Convergence of the single integration code for the test case 72
4.4 Convergence of the double integration code for the test case 74
4.5 Model parameters used in the numerical simulation 75

5.1 The parameters for the LQ model for different cell types 99

Chapter 1

Introduction

In recent years, the understanding of tumours in general and brain tumours in special evolved a lot. So in surgery the neoplastic areas are often marked in order to enhance the contrast between healthy and affected tissue. This enables the surgeon to resect the tumour in a more exhaustive way. In radiotherapy external beam radiation is delivered in such a way that also complex shapes of tumours get a deadly dose, while side-effects for the patient are minimized. For certain tumours also brachytherapy is applied, where a radiating substance is implanted in the cavity left by the resection in order to irradiate tumour cells that infiltrated the healthy tissue near the tumour site. However, even today with all of these possibilities to treat tumours, high grade glioma (for example *glioblastoma multiforme*) are not curable in general. This is due to the highly infiltrative behaviour of glioma cells in a high grade tumour. A key feature thereby is the migration of glioma cells along fibre tracts in the brain. So, in order to determine the actual tumour extent (or a good approximation of it) it is of particular importance either to track the migrating cells, which is not possible in the brain, or to use data-based mathematical modelling that enables to simulate the tumour spread into the brain tissue in order to get a better assessment of the infiltrated regions. Clearly this task is highly non-trivial, and this present text is a step in the direction of data-based (and patient specific) mathematical modelling of tumour growth. We focus here on cell migration and proliferation – important features during the infiltration. Especially the cell migration is hard to describe exhaustively, because there is a multitude of processes involved in cell movement; for more details, we included in the following section a short description of the most important ones.

The main reason for personalized mathematical modelling of high grade glioma is enabling better treatment by predicting the tumour spread in the brain. As the resection volume is constrained by the surrounding brain components, the prediction will not enhance the resection, but will render available additional information such that the target volumes in

radiotherapy can be adapted to enhance the treatment. There are three prominent target volumes: the gross target volume (GTV), which is the region that is identified as tumour by diagnostics; the clinical target volume (CTV), which is the adaptation of the gross target volume to include further possible regions at risk from the point of view of tumour spread relying on the expertise of clinicians. For example it is more probable that a tumour invades certain regions like white matter tracts due to their special structure. Finally the planning target volume (PTV), which is the clinical target volume augmented by a security margin. The latter is necessary in order to control uncertainties in the positioning of the patient and in the therapeutic dose delivery.

The most interesting part where mathematical modelling can help is the assessment of clinical target volume upon starting from the gross target volume. Here additional information can support the expertise of the medical doctors, because numerical predictions reveal finer structures in the tumours, that are not visible by standard diagnosis (see figure 4.2 in chapter 4).

This text is largely based on the publications [EHS15] and [HS16] with some adaptation to clarify the presentation.

Key properties of the multiscale model class presented here are very few free parameters (in fact, a single one), thus increasing the reliability of the final simulation outcomes, along with a biologically motivated mesoscopic proliferation description that does without introducing further free parameters. Additionally, we present a complete working pipeline ranging from the medical data (available by the common diagnostics in clinical practice) to the data meeting the requirements of the mathematical model. The numerical simulations of the model are done in three dimensions in order to enable direct interpretation of the results. This is a step forward from the previous works [EHKS14, EKS16], which are a source of inspiration for this text.

1.1 Biological background

The process of cell migration can be divided into five major steps (see [HW03, PDY09, PD99] for general information on cell migration and [BBPSP14] for a very detailed overview of the involved subcellular processes):

- **Polarization:** This refers to the distinction between a cell front (the direction in which the cell selects for migration) and its rear. The polarization is triggered by environmental diffusion and non-motile signals as chemoattractants and variations in the substrate, leading on the macroscale to chemotaxis and haptotaxis, respectively.
- **Protrusion:** By polarization, the cell acquires an orientation (front, rear). This is the base of the de novo formation of protrusions (like lamellopodia and filopodia) at the

front. Here we have to differentiate between three processes: extension of the plasma membrane, formation and reinforcement of a cell skeleton supporting cell membrane extension, and forming cell-substrate contacts.

- **Adhesion:** After the formation of cell-substrate contacts, the cell adheres to the extracellular matrix (ECM) with the aid of so-called integrin receptors, a large superfamily of heterodimeric cell surface receptors that are able to bind to different ligands on the ECM. Moreover, cell-cell adhesions are mediated by cadherins, a class of transmembrane proteins.

- **Regulation and integration:** Intracellular signalling cascades triggered by the bindings of integrins and other receptors retain the cell polarity and drive subcellular processes like actin polymerization leading to a cell membrane stabilization.

- **Cell body translocation and retraction of the rear:** After reinforcement of the cytoskeleton the cell contracts and relocates the nucleus. Then the rear is retracted and the cell moves in the previously selected front direction.

The influence of these processes has been described in quite a few mathematical models (see for example [GO04] for a continuum model describing cell movement based on viscoelastic descriptions, [AP08] for adhesion mechanisms based on the modelling of the ECM as elastic material, [SLR12] for a cell motility model including actin flow and adhesion and [AZ16] for a further mathematical model taking actin dynamics into account). Here we focus on the cell-substrate (especially cell-ECM) bindings as key for the migration. This will allow to include haptotaxis and it remains for future work to include cell-cell adhesion, chemotaxis, and more into a multiscale model for cell migration. Several of these processes are discussed in more detail in chapter 6. Cell-tissue interactions are essential for all dynamics performed by cells in vivo, including migration, proliferation, and even mere survival [GG04, UGR99, GW96]. Haptotaxis - the motion of cells in the direction of the gradient of a non-diffusing environmental cue (here tissue) - plays an essential role in tumour spread [GKL$^+$96, UGR99], the more so in the case of glioma moving in the highly anisotropic brain tissue. Therefore, we concentrate our modelling effort on the description of these interactions.

1.2 Outline

Aiming at simulating a brain tumour in its natural environment, we set up a data-based multiscale model class or a multiscale modelling cascade ranging from the cellular level incorporating subcellular dynamics to the macroscopic one, where the tumour bulk is observed. We use for the transition between the scales the classical tools of averaging (cellular

$\rightarrow$ meso, known from the deduction of the Boltzmann equation), and parabolic scaling (meso $\rightarrow$ macro, a standard approach in the kinetic theory of active particles [Bel08]).

- **Chapter 2 (Modelling):** This chapter starts motivating brain tumour models followed by a short glimpse on some of the existing ones. Then we set our foundation, a cellular model incorporating subcellular dynamics. Here we employ two different driving processes: the velocity jump process, explored in connection to cell migration e.g. in [Alt80, EO05, PH13, EHKS14, EKS16, EHS15, HS16], and a Gaussian process. From the microscopic processes, we deduce mesoscopic equations using the standard tools for mean field equations. On this intermediate scale we include proliferation via cell-tissue interactions (published in [EHS15]) and deduce from the so augmented mesoscopic equations some effective ones on the macroscopic scale by parabolic scaling. One key property of this modelling is the incorporation of real data, so we include patient specific information about the tumour environment. Yet missing in the context of modelling is the rigorous proof of the convergence of the averaging as well as the parabolic scaling; especially the latter is a non-trivial task, although there is a new result proving convergence of a similar model to a hyperbolic system of limit equations [NU16].

- **Chapter 3 (Data):** We dedicate this chapter to the description and processing of the available medical data, so we explain which data types (CT and MRI) are available in the context of brain tumour diagnosis and how they can be exploited in the context of mathematical modelling. Thus we are able to estimate the directional distribution of fibres with the aid of the so-called orientation distribution function, a well-known and often assessed quantity in medical computer vision. Then a method of estimating the overall volume fraction of tissue fibres based on diffusion measurements is presented (published in [EHS15]). The data chapter closes with a collection of example codes and recommendations of software packages useful for the data processing.

- **Chapter 4 (Numerics):** We present a method of discretizing the macroscopic equations describing the tumour spread. We focus on the preservation of several features (non-negativity, local mass conservation) expected from the simulated cell density. This is of particular importance for the later real world interpretation of the results. We provide a numerical convergence analysis of the building blocks of the code and present outcomes of numerical simulations, all done in three space dimensions (we use a single two dimensional simulation for comparison purposes).

- **Chapter 5 (Therapy):** We present a related model, where a novel idea of chemotherapy concurrently to radiotherapy is modelled (published in [HS16]). There we proceed

through the same steps (parabolic scaling) in order to arrive at a macroscopic description that is handled with the numerical scheme presented in chapter 4. We show then numerical outcomes of different therapy strategies motivated by the standard choice of radiotherapy in clinical practice.

Chapter 2

Modelling

2.1 Introduction

Although cell migration and dispersal happen directly in nature and are observable at least in vitro, there are reasons to use and prefer mathematical modelling. On the one hand mathematical research, here we mean modelling, analysis and simulation of the corresponding models, involve lower costs in comparison to biological or chemical research, for no laboratories, neither materials other than a computer, are necessary. On the other hand one may concentrate on one single effect and perform analysis without observing cross interactions. While biologists need cell populations with gene-knockouts, which are to be produced first, mathematicians just model the desired effect having the possibility to reduce or increase the complexity. In this way a sensitivity analysis can be done both in a cost-effective and fast way. Nevertheless, the biological verification of the mathematical findings has to be yet assessed in comparison with reality, but the precomputation step done by mathematical modellers can save resources and provide more insight into the phenomenon of interest. The described way culminates in testing different hypotheses about complex biological systems in order to identify the crucial ingredients involved (see e. g. [HHB$^+$07], where structural forming of the liver was analyzed with respect to the key processes leading to the observed pattern).

Nevertheless, there are different pitfalls, which have to be circumvented. One of them is the use of abundant parameter sets. While these actually deliver the degrees of freedom in a model, they have to be chosen in such a way that they can be measured in a reliable manner, or at least the majority of them. There is no point in having a complex mathematical description involving lots of unknowns, because models including many parameters can exhibit completely different behaviour, so they are not tailored to the problem (an essential property of a model) rendering the results questionable. Contrariwise, if the model has only one free parameter that cannot be assessed by measurements, this has a few advantages:

The flexibility is preserved so the free parameter and hence the model itself can be adjusted to real data; the reliability of the model is increased, because there are no cross influences stemming from further free parameters. So the model behaviour is preserved in a better way through large ranges of the actual value of the parameter. Thus we will set up models which are as simple as possible with respect to their number of free parameters but still including the desired aspects.

Another pitfall in mathematical modelling are the scales, on which the phenomena of interest are described. Many processes in nature occur on largely varying scales. An example is cell migration. While the cells migrate on the scale of micrometres per minute [CS95], the subcellular processes like binding of chemical substances to cell surface receptors as well as nutrient exchange between the environment and the cell are clearly taking place on another scale, where the cell surface receptors or signalling channels are of importance. These are very small compared to the size of a cell and the involved biochemical processes are much faster than the actual migration.

A mathematical model has to take this into account, resulting in different (sub)models for different scales. Averaging and scaling procedures are typically used to connect the scales, leading to mean-field equations and effective descriptions on the higher scale of interest. In the above example of cell migration, there are two different scales influencing each other. There is the possibility to break down the larger scale onto the finer one to have an integrated model on the finest scale. This is typically done via introducing free parameters and unnecessary complexity, which is clearly not optimal in the eyes of a mathematician. Another approach is to sacrifice the fine dynamics for a coarser model on a large scale, hence rewriting the fine effects as macroscopic terms. This is not the best way to go either, as it leads to a mathematical model where the terms on the macroscopic scale are imposed without the aid of a derivation. So then we have to abstain from the direct motivation of these terms. As we do not want to relinquish important information, we use the technique of multiscale modelling, where the scales are connected appropriately into a single model. Recently quite a few models of this type were proposed (see e. g. [Bel08, BD08, BBNS12, EO05]).

2.2 Tumour Modelling

Now we are moving on towards the core of the present work, tumour modelling. Because there are many cell types and hallmarks involved [HW00, HW11], an exhaustive description is out of reach, but concentrating on certain relevant aspects may help obtaining useful results. We focus in this work only on brain tumours and especially glioblastoma multiforme (GBM), where as mentioned the brain structure plays an essential role in tumour development and spread. In clinical applications it is not important to know the local variation of the cell types contained in a certain tumour bulk; much more relevant for the therapy planning is

the reliable information about the location and hence the extent of the tumour at a certain time. Thus the model has to be a spatio-temporal description of the tumour mass. The main characteristics of GBM are the high migration speed of the cells (around $0.21\ \mu$m/s [CS95]) along with a highly infiltrative behaviour, thus a highly anisotropic spread. Due to these traits, GBM has a very poor prognosis – clinical studies suggest a median survival rate of about one year (12.1 months) after diagnosis [YJDS15], but GBM account for around 15 % of all diagnosed neurologic neoplasia [SMvdB$^+$05]. One of the consequences of the mentioned infiltrative behaviour is that a high number of brain tumours cannot be located in a reliable manner, because the techniques of non-invasive imaging cannot reveal the true magnitude of the tumour extent [WSP$^+$14, HNRW15]. Thus there is an urgent need to enhance the diagnostic instruments in order to refine the spatial information, so that it can be used for better therapy planning, particularly applicable to radiotherapy, where such information is essential. Hence this is quite an active field of research.

In the last years, image processing and segmentation techniques evolved in order to enhance the visual contrast between the healthy brain and the tumour tissue (see e.g. [WSP$^+$14] for a tumour progression mapping and [HNRW15, FBZ$^+$16, KIN$^+$01]). This clearly has the advantage that only a few images are needed; however, this is also the main disadvantage, as only single distinct time points are taken into account, while it would be desirable to have evolutionary information. However, registering image sequences is economically often not feasible. Another problem with the imaging techniques is that they can only be applied to a specific image and hence are confined to the given resolution, while finer structures, which are not represented, may also be of importance. One possibility to overcome these issues is to set up a biologically motivated and physically reasonable mathematical model describing the tumour growth. Such an instationary model can be simulated up to every time point of interest, while these simulations are typically cheap, fast, repeatable, and do not have any side effects for the patient.

However, each mathematical model has to be validated in order to get the simulation results as near to reality as possible. This validation is quite a hard task for certain models, because reliable information is sparse and often not accessible. However, in clinical practice so-called follow-ups are typically made. They are images taken at a later time point after treatment, and they can be used to train mathematical models. Especially in the brain, where the inherent structure is of tremendous importance to the actual shape of the tumour, it is important to personalize not only therapy, but also the corresponding mathematical models. As mentioned, the diagnostics provides image data, which can be used to account for the individual brain structure. For the extraction of usable information from typical medical data sets we refer to chapter 3 in this work.

What is important?

- A tumour model has to rely on physical and biological assumptions, like finite cell speed or Newton's law of motion (here we neglect the relativistic changes to a motion, because cells are very slow compared to the speed of light).
- Due to the complexity involving lots of modelling scales, the resulting model should be a multiscale one.
- The model should be compatible with patient data stemming from the standard diagnostic process.
- The model has to be simple enough to do model validation and verification using real data.

What should be avoided?

- A tumour model should not contradict causality or other principles of physics.
- A model should not have too many free parameters, which cannot be assessed by measurements.

2.3 Previous Models, State of the Art

Before we set up the multiscale model class used in this thesis, we want to present different kinds of tumour models or more correctly, different kinds of modelling techniques. Thereby we try to state the different advantages and disadvantages in an objective and clear way.

- **Individual based, agent based & cellular automaton models**

  These are approaches where the individual cell behaviour is modelled. The main advantage (which may also turn out to be a disadvantage, if the model is not set up carefully) is for sure the flexibility. Different forces and interactions of the agents can be prescribed in a descriptive and concise way. Nevertheless one may be tempted to rely on biologically wrong assumptions in order to generate presumptive patterns and traits. This claims for a very careful introduction of the modelling assumptions with a verification that the desired property is not already introduced right at the beginning, but to let it evolve out of reasonable presumptions. The model class under consideration can also be used for the in silico replication of in vitro experiments rendering the

model validation and parameter estimation a simpler task to accomplish. So the connection between the biological experiment and the mathematical model is much more direct as in the other types of models. Cellular automaton models (see e. g. [MBG+06] for in vitro cell network formation, [OGR+03] for biological cell simulation, [SP12] for a multiscale cellular Potts model and [RK08] for a glioma invasion model) are based on physical principles like energy minimization expressed by the so-called Hamiltonian. It is connected to Hamiltonian systems, that are understood very well, contrary to the equations arising from complex multiscale models. The most important practical advantage of this type of modelling is the computational stability. The implementation is very straightforward and less error-prone when compared to PDE models, where essential properties have to be preserved. The most important one, but also in general the hardest to acquire, is the non-negativity of a solution. On the individual level, however, problems like preservation of non-negativity do not occur. So from this point of view, the agent-based models are optimal, but they are based on the simulation of single trajectories. Unfortunately, if a density describing the population of agents is of interest, many trajectories are needed, dramatically impacting the overall computation time. Even if many trajectories are simulated, these may form a null set or differ in certain properties from the desired cell density. So the outcome may not be as reliable as for other types of models.

- **Pure macroscopic models**

  Here, in contrast to the previous paragraph, we will focus only on models for glioma spread in brain tissue. They consist of different types of macroscopic PDEs describing the evolution of densities and concentrations involved in the relevant processes. Among them, those forming the class of reaction-diffusion or reaction-convection-diffusion equations for a cell density $\rho(t,x)$ are the most prominent ones. The prototype of such an equation is

  $$\partial_t \rho - \operatorname{div}\left(D(x)\nabla\rho\right) + \operatorname{div}\left(u(x)\rho\right) = g(\rho).$$

  The diffusion coefficient D may be a spatially dependent tensor, as introduced in [JMD+05], or a diffusion coefficient depending on the position, especially on white and grey matter [RAJRS09, HCS+12]. This latter approach is a bit counterintuitive, because the labelling of white and grey matter is not a sharp one; especially subject to the lacking spatial resolution in real patient data, such an assumption is not realistic. D may also represent a fixed constant diffusion rate. The term involving the coefficient u describes drift, which is often omitted, but can be selected in a way to approximate a prescribed shape in the simulation. The reaction term $g(\rho)$ accounts for the tumour growth, where most often either a logistic or even an exponential growth is employed. Examples of models using this prototype of equations are

[JJHD+15, RAJRS09, HCS+12, ARGQ09]. A simple example, taken from [HCS+12], is the model

$$\partial_t \rho = \operatorname{div}(D\nabla\rho) + C\rho\left(1 - \frac{\rho}{k}\right) - \mathcal{T}(\rho), \tag{2.1}$$

where $\mathcal{T}$ describes a therapy term using the LQ model [HCS+12], D is a single valued diffusion coefficient and the growth is standard logistic. This is oversimplified, because it generates symmetric outcomes not observed in clinical practice [SC+12], but has very few free parameters (the parameters of the therapy term are available in data) for which it is sufficient to use only two segmentation images for the estimation. So the authors of [HCS+12] are able to optimize the therapy to arrive at the lowest simulated tumour. This is very difficult (if possible at all) to achieve with some more complicated models like the multiscale ones. The question, however, is how adequate such simplified models as in (2.1) are to account for the actual tumour growth. The multiscale model presented in this work leads to a macroscopic equation as depicted here, however, the parameters D, u and g are more sophisticated, as they originate from the interaction between the model scales and are deduced formally out of biologically and physically plausible assumptions. Further extensions would include the description of the remodelling of the tissue and more complicated diffusion terms, as non-linear and also degenerate diffusion [ZSU16, ZSH].

- **Kinetic models**

  Kinetic models, especially kinetic velocity jump processes were introduced to describe migration of bacteria [Alt80], but have also been applied to mesenchymal motion, which is part of the invasion process of gliomas, in [Hil06] and even for glioma migration using real patient data in [PH13]. These models are simpler than the presented multiscale model is, as there is only one modelling scale, but this makes the analysis more intuitive than in the case involving subcellular dynamics. However, from an idealistic perspective, this is exactly what is missing in the monoscale models. They cannot be based on biological principles, which is for the assumed aim a necessity. Nevertheless, modelling assumptions have to be made and the kinetic models are a valuable tool for describing the migratory behaviour of cells. Extensions of the kinetic models using a multiscale modelling approach were proposed in the context of the kinetic theory of active particles [Bel08]. The model class presented in this text is stated in this modelling framework; thereby we chose specific forms for the parameter functions and did the explicit scaling of the model to the macroscopic scale.

- **Hybrid models**

  Hybrid models try to combine the advantages of the individual models with those of the pure PDE approach by introducing some quantities as continuum variables, while

others are assumed to be discrete. Anderson and Chaplain [AC98] started hybrid modelling for angiogenesis and blood vessel growth in the presence of a tumour resulting in the expected formation of blood vessels. Later on, hybrid modelling was applied to tumour growth and invasion [ARGQ09]. However, as hybrid models combine individual processes with PDE models, they inherit also the disadvantages of the agent-based descriptions. Hence they simulate only one single trajectory at once, leading to the same computational problems as their pure discrete analogues.

As all model types presented in this subsection have strong disadvantages, we do not employ them directly, but opt for a multiscale approach. This has also some disadvantages: the mathematical theory has not evolved as far as for the other model classes, and the numerical simulation of the models is often infeasible, so that it is necessary to rescale them in order to obtain correct macroscopic descriptions which can be well handled numerically

2.4 Multiscale Models

Here we want to lay the very foundations of the multiscale model to be analyzed in the following. The model basis stems from [KS12b, SS10] with slight modifications. It was analyzed in [KS12b, EHKS14, EKS16, EHS15] and also in a slightly changed mesoscopic form in [HS16].

2.4.1 Microscopic Description

The task is now to model tumour cell migration on the microscopic scale. With this we mean the scale on which cell migration (for an observer) takes place, namely the cell scale. The aim is to deduce a macroscopic model including real medical data, hence finally, we are interested in spatial scales of around 2 mm, which is very large in comparison to the size of an individual cell. We do not want to make the microscopic description too complex, so the standing assumption is that a cell can be described as a point. At first glance, this is very restrictive, but we do not want to describe interactions on the microscopic scale, so there is no need to track the actual shape and extent of a cell; for models including them see for example [WO16]. For the description of the movement of such point particles, we will employ Newton's law. While this is problematic for higher speeds as argued in the relativity theory, where a Newtonian particle can exceed the speed of light, cells are slow enough, so that relativistic effects are negligible. So let now $x(t)$ be the position of a single cell and $v(t)$ its corresponding velocity. Then Newton's law reads (for a normalized cell mass)

$$\mathrm{d}x = v\,\mathrm{d}t$$
$$\mathrm{d}v = F\,\mathrm{d}t.$$

Remark 2.4.1. *We mentioned the normalized cell mass, but this statement can be recast from an algebraic viewpoint equivalently as a normalized force F. The classical Newton law can be written as*

$$\begin{aligned}\dot{x} &= v\\ \rho\dot{v} &= F,\end{aligned}$$

hence using the transform $F \to F/\rho$ will result in the previously stated equations.

Subcellular dynamics, in particular receptor bindings are essential for the migration of a cell, because the only possibility of a cell to interact with its environment is through the membrane, which plays thus the important role of transmitter of forces necessary for migration. In general, these forces are exerted on other cells, myelinated axon bundles and the extracellular matrix (ECM). We focus only on the latter one, since Guo and Giancotti [GG04] conclude that the ECM is of crucial importance for migration as well as proliferation (a process modelled later on). Cells interact with the ECM through cell surface receptors, of which the so-called integrins, a class of heterodimeric surface receptors, are the most prominent ones [GG04]. We neglect as a first step towards a multiscale model the bindings to other cells (cell-cell adhesion, see discussion) and myelinated axons, although the latter form a substrate of low resistance to migrating cells [GW96]. This simplification is done, because the interaction with the ECM is the most crucial (and ubiquitious) ingredient in cell behaviour, especially in migration and proliferation [GG04] (see also table 3 in [UGR99] for known effects of a variety of integrins in glioma biology).

The forces necessary for migration and acceleration (pulling of the cells at the ECM, other cells, and myelinated axons) have to be included in Newton's law. However, the mentioned forces are only imposed on the subcellular scale, but they transmit as a small contribution to the cellular one. So there are two possibilities to succeed: first, one can adjust the modelling scale and opt for a subcellular-scale model, where the forces are directly included. However, this increases complexity (typically by introducing additional unknowns) and is harder to interpret on a reasonable spatial scale (given by the medical data). Second, one may incorporate the net effect of the forces exhibited at the subcellular scale into Newton's law (on the cellular scale) with the aid of a stochastic process $S(t)$ depending on events occurring on the subcellular scale (we choose a velocity jump and alternatively a Gaussian process). This distances us from incorporating the forces explicitly as acceleration ($\dot{v} = F$), however, due to the large variety of different cell surface receptors and ECM ligands (see table 1 in [UGR99]), we incorporate the forces using a stochastic process. This means that we do not need to track the whole complexity of the subcellular scale, which is hidden in the noise, but only the large scale effect. It still remains to discuss in which equation the stochastic term should be included. Candidates are the x-equation, meaning stochastic perturbations

of the position, and the v-equation leading to velocity perturbations. This is connected to the question of whether to use the Einsteinian (x) or the Ornstein-Uhlenbeck (v) theory of Brownian motion[1]. A critical discussion is available in [Nel67], but in essence the Ornstein-Uhlenbeck theory has several advantages, especially on short time scales, so we adopt it and include the stochastic process into the v-equation. This leads to

$$\begin{aligned} \mathrm{d}x &= v\,\mathrm{d}t \\ \mathrm{d}v &= \mathrm{d}S(t), \end{aligned}$$

where the latter equation is so far only written in a symbolic way.

As mentioned before, we opt for simplicity of the subcellular scale and do not model it in a quantitative way, as it is very hard to get exact numbers of the different integrins, since they are abundant (around 10^5 per cell [BTZ$^+$05]); instead we write a model accounting for essential features. So the extracellular matrix, although containing a variety of different macromolecules, is represented by a single variable. As the ECM by its own is very difficult to acquire, but abundant in all body tissues, we approximate the ECM by the macroscopic volume fraction of tissue fibres, here denoted by Q. The latter quantity is estimated as described in the data chapter 3. The other needed variable has to be connected to the integrins. As mentioned before, it is pointless to use a quantitative approach measuring the binding state of each individual receptor (here it would be necessary to distinguish between different components of the ECM, as certain receptors bind only to specific ligands (see e. g. table 1 in [UGR99])). Hence we use a single variable y for the density of bound integrins over a cell. Although the number of receptors is not conserved in general, the consideration of a unitless (mathematical) density y (so $y \in [0,1]$) has the advantage that its range is constant (and known) over time. This is a slight deviation from the previous works [EHKS14, EKS16, EHS15], where y was the density of receptors bound to the ECM, but scaled with the (absolute) number of integrins (R_0 in [EHKS14, EKS16, EHS15]).

For the previously introduced variables, we set up the qualitative reaction scheme (as in [EHKS14, EKS16, EHS15])

$$Q + (1-y) \underset{k^-}{\overset{k^+}{\rightleftharpoons}} y. \tag{2.2}$$

This describes a "binding" reaction happening with positive rate k^+, where the ECM (Q) interacts with the free receptors ($1-y$) and bound receptors (y) are formed. The reverse "unbinding" reaction takes place with positive rate k^-.

Note 2.4.1. - *The reaction scheme* (2.2) *is only assumed to be valid in the averaged, mean field sense and not for a single receptor. The latter assumption would be too*

[1] In this text, we will consequently use the term Brownian motion for the physical process of a random motion and Wiener process for the mathematical description of Brownian motion.

restrictive, as the integrin family is very heterogeneous [UGR99], leading to a bunch of distinct reaction schemes.

- *In previous works [EHKS14, EKS16, EHS15], the number of free receptors (here $1-y$), is computed as R_0-y, where R_0 denotes the number of integrins per cell. This quantity is assumed to be conserved in [EHKS14, EKS16, EHS15].*

Now we employ mass action kinetics to arrive at the simple ODE

$$\dot{y} = -(k^+Q + k^-)y + k^+Q. \tag{2.3}$$

Note that the equation is the same as in [EHKS14, EKS16, EHS15] with $R_0 = 1$ in the notations therein.

Assumptions:

- The volume fraction Q is proportional to ECM with $Q \in [0,1]$ or $Q \in (0,1)$, because $Q = 0$ and $Q = 1$ are not sensible values for body tissues.
- The cell surface receptors, here integrins, of density y are able to interact with the volume fraction of tissue fibres. Moreover, it is assumed that $y \in (0,1)$.
- The binding rate is $k^+ > 0$, comparable to k^-.
- The detachment rate is $k^- > 0$, comparable to k^+.
- The mass action kinetics description is valid for the simple reaction scheme (2.2).

In the last paragraph we introduced the simple, qualitative subcellular model (2.3), so far not combined with the cell-scale model consisting of Newton's law for the movement. Before this is done, it is important to analyze for equation (2.3), whether the assumptions, especially about the range of y, remain valid, once fulfilled.

Lemma 2.4.1. *Let $Q \in [0,1]$. Then $(0,1)$ is a trapping region for* (2.3)*.*

Proof. We only need to show, that $G(y) = -(k^+Q + k^-)y + k^+Q$ points inwards on the boundaries of the domain $[0,1]$, namely $G(0) > 0$ and $G(1) < 0$. This is obvious. □

To make the scaling done in the following feasible, we need more properties of the equation (2.3). These will be collected in the next lemma.

Lemma 2.4.2. *The only steady state of* (2.3) *is given by*

$$y^\star = \frac{k^+ Q}{k^+ Q + k^-}, \tag{2.4}$$

which is moreover exponentially stable.

Proof. This is a simple calculation. □

For the incorporation of the subcellular dynamics, it is convenient (and for the analysis necessary) to measure only the derivations of the subcellular variable y from its steady state, so the new variable under consideration is

$$z = y - y^\star$$

with $z(t) \in Z = [-y^\star, 1 - y^\star]$.

Note 2.4.2. *The transformation of y to z was also done in [EHKS14, EKS16, EHS15, HS16] as well as in earlier papers like [EO05]. The notation of z is not the same as in [EHKS14, EKS16, EHS15, HS16], but the negative of it. We introduced this change in order to preserve the orientation, so higher z values correspond to more cell-ECM bindings.*

In general, the volume fraction of tissue fibres Q is spatially dependent and we include the total differential $\frac{\mathrm{d}z}{\mathrm{d}t}$ instead of $\dot{z}$ into the mesoscopic model. By computation, we have

$$\begin{aligned}\frac{\mathrm{d}z}{\mathrm{d}t} &= \dot{y} - \frac{\mathrm{d}}{\mathrm{d}x} y^\star \frac{\mathrm{d}x}{\mathrm{d}t} \\ &= -(k^+ Q(x) + k^-) z - f'(Q(x)) v \cdot \nabla_x Q,\end{aligned}$$

using the convenient notation $f(s) = \frac{k^+ s}{k^+ s + k^-}$. The symbol $y^\star$ was only introduced in order to express the equilibrium state, whereas f will be used during the rest of the text. All in all, when the subcellular scale is already included in the model, we have the microscopic–subcellular scale model

$$\begin{aligned}\mathrm{d}x &= v\,\mathrm{d}t \\ \mathrm{d}v &= \mathrm{d}S(t, x(t), v(t), z(t)) \\ \mathrm{d}z &= -\Big((k^+ Q(x(t)) + k^-) z(t) + f'(Q(x(t))) v(t) \cdot \nabla_x Q(x(t))\Big)\,\mathrm{d}t.\end{aligned} \tag{2.5}$$

Now the point is to choose a reasonable stochastic term $S(t, x, v, z)$, which clearly needs to depend on z to express the connection between the cellular and subcellular scales. Moreover, the dependence on x is mandatory, as we want to include patient specific tissue information, typically available in a spatio (-temporal) manner. In previous papers [KS12b, EO05, PH13], the stochastic term was chosen as a velocity jump process with the kernel

$$K(x, v, v') = q(x, v). \tag{2.6}$$

We denote in the following by $X \subset \mathbb{R}^d$ the spatial region and by $V \subset \mathbb{R}^d$ the region of admissible velocities. During this text V will be a scaled sphere. Then $q\colon X \times V \to \mathbb{R}$ is the tissue fibre orientation distribution. We assume it to be normalized, so

$$\int_V q(x,v)\ \mathrm{d}v = 1 \quad \text{for all } x \in X.$$

In the case where V is a scaled sphere, $q(x,v)$ represents the quantity $\frac{q(x,\hat{v})}{\omega}$ in [EHKS14, EKS16, EHS15, HS16], where ω is the normalization due to the sphere volume and $\hat{v} = \frac{v}{|v|}$ is the direction. In chapter 3 we estimate the quantity $q(x,\theta)$, where $\theta \in \mathbb{S}^2$ is the orientation. The kernel q is important as it represents also the solution F of the detailed balance equation $K(v,v')F(v') = K(v',v)F(v)$ (see e. g. [CMPS04]), which will represent the equilibrium distribution (in v) of the later cell density. The velocity jump process is then sufficiently described by this equilibrium distribution (or equivalently by the kernel K) and a turning rate, the latter being assumed to depend on z in an affine way, because the forces necessary for migration on the subcellular scale (only included via the variable z) are the cause of the turning. We will select the rate to be $\lambda[S] = \lambda_0 + \lambda_1 z > 0$, corresponding to [EHKS14, EKS16, EHS15], with a change in the sign of λ_1 to compensate the sign change of z.

We introduce also a second stochastic process driven by a standard Wiener process. The velocity jump process with turning rate λ represents the reorientation on the time scale $\frac{1}{\lambda}$, however, it is not clear whether this reorientation happens on exactly this times scale or faster. The cause for this is, as we only track the cell as a point (representing a cell centre like the centre of mass or the nucleus), the reorientations may take place instantly or very fast when the cell undergoes irregular shape changes during movement. For these fast reorientations a Gaussian process (leading to instant reorientation) is more appropriate. Moreover, it is standard to the mathematical modelling community. Now we start with the velocity jump process case.

In the situation at hand it is very complicated to write an explicit equation on the microscopic scale as in [SS10], but as we are not particularly interested in the microscopic scale, we opt for directly writing an equation on the mesoscopic scale, where the process can be described with the aid of the turning kernel K acting on the velocity space. Then the equation with a pure reorientation term on the mean field scale reads for a mesoscopic density distribution function of tumour cells $p\colon [0,T] \times X \times V \times Z \to \mathbb{R}$

$$\partial_t p(t,x,v,z) = \lambda[S] \int_V \left(K(v,v')\,p(v') - K(v',v)\,p(v)\right)\ \mathrm{d}v' \tag{2.7}$$

As mentioned before, we want to use the orientation distribution of tissue fibres $q(x,v)$ to dictate the direction of motion irrespective of previous cell reorientations, which can be achieved by the kernel K as in (2.6).

The microscopic model (now in absence of the reorientation effects) reads

$$\begin{aligned} \mathrm{d}x &= v \ \mathrm{d}t \\ \mathrm{d}v &= 0 \ \mathrm{d}t \\ \mathrm{d}z &= \left(-(k^+Q + k^-)z - f'(Q)v \cdot \nabla_x Q\right) \ \mathrm{d}t. \end{aligned} \tag{2.8}$$

In order to remain compatible with the former case, our aim is to have the same "turning rate" and the same equilibrium distribution $q(x, v)$. This can be achieved by using the modified microscopic model

$$\begin{aligned} \mathrm{d}x &= v \ \mathrm{d}t \\ \mathrm{d}v &= \sqrt{\frac{2(\lambda_0 + \lambda_1 z)}{q(x,v)}} \ \mathrm{d}W_t \\ \mathrm{d}z &= -\left((k^+Q + k^-)z + f'(Q)v \cdot \nabla_x Q\right) \ \mathrm{d}t, \end{aligned} \tag{2.9}$$

where the second equation needs to be clarified. Here we have to assume that $\inf_{x\in X,\ v\in V} q(x, v) \geq \alpha > 0$, which is indeed the case for our choice of the orientation distribution of tissue fibres (see chapter 3). The driving process W_t is a d-dimensional standard Wiener process: W_t is a time-continuous martingale with $W_0 = 0$ and $W_t^2 - t$ is a martingale. As v is not guaranteed to stay in V by the second equation of (2.9) (especially if V is a sphere), we only consider the contribution in V of the right hand side of the second equation of (2.9) on v. This is a projection onto V of the right hand side of the second equation. We intentionally wrote the system (2.9) without the (complicated) projection, as it is quite non-trivial to arrive at a Wiener process on manifolds (here the sphere). While the Stratonovich calculus is often employed in physics (mainly to have a classical chain rule), it is here not appropriate and we use Itô calculus instead. This is because the Stratonovich integral leads to an anticipating process (while the Itô integral does not), which is counterintuitive for cell behaviour, as this would mean that the cell utilizes future information for the migration, what is clearly not the case and should be avoided in a mathematical model. The stochastic term connects (for the velocity variable) to the operator

$$(\lambda_0 + \lambda_1 z)\Delta_V \left(\frac{\cdot}{q(v)}\right)$$

on the mesoscopic scale (see e. g. [KS12a]). Now we investigate the equilibrium distribution. We aim to solve

$$\Delta_V \left(\frac{g}{q(v)}\right) = 0$$

for a function $g\colon V \to \mathbb{R}$. On the sphere $\mathbb{S}^2$ (which will be the case later on), the solution space is spanned by $q(v)$, as the nullspace of the Laplace-Beltrami operator is one-dimensional

[FS08]. In an arbitrary domain $V \subset \mathbb{R}^d$, we get $p(v) = q(v) \cdot h(v)$, where h is some harmonic function and $p(t, x, v, z)$ is as before the density of tumour cells.

Theorem 2.4.1. *Let $Q \in C^{1,1}(X)$ and q be smooth enough such that the diffusion coefficient $\sqrt{\frac{2(\lambda_0+\lambda_1 z)}{q(x,v)}}$ in (2.9) is at least globally Lipschitz-continuous in x and v. For our choice for q this reduces to the assumption, that the water diffusion tensor (see data chapter 3) is continuously differentiable $D_W \in C^{1,1}(X)$. Then there exists a (strongly unique) strong solution to (2.9).*

Proof. Apply theorem 5.2.9 in [KS12a]. □

2.4.2 Mesoscopic Description

The growth of the tumour cell population is, of course, an important issue, hence it has to be modelled as well. We will dwell on this later on, but first the microscopic models have to be converted into mesoscopic ones. This is done via averaging (see for example [KS12b] or [Oel91]). Here we denote by

$$\begin{aligned} p\colon [0,T] \times X \times V \times Z &\to \mathbb{R} \\ (t, x, v, z) &\to p(t, x, v, z) \end{aligned}$$

the cell density at time t, position x, velocity v, and normalized receptor binding state z. If not stated otherwise, we will assume in the following that $X = \mathbb{R}^d$, $V = s\mathbb{S}^{d-1}$, and $Z = [-f(Q), 1 - f(Q)]$ with homogeneous Dirichlet boundary conditions. For the sake of simplicity, we assumed that the space V is given by the scaled sphere $s\mathbb{S}^{d-1}$, where s is the mean speed of a tumour cell and is assumed to be constant. This means, in particular, that we are merely interested in the direction of the cell velocity as the essential feature dictating the cell orientation. This newly introduced parameter s may be measured reliably via experiments in a Petri dish or even with mouse models. Chicoine and Silbergeld [CS95] estimated it to be around $0.21 \cdot 10^{-6} \frac{\mathrm{m}}{\mathrm{s}}$. We need to include the units of all parameters due to compatibility issues with the real patient data. This is a proceeding contrary to usual mathematical modelling, where all units are removed via non-dimensionalization.

Using the standard approach of deriving mean field equations (see e. g. appendix A in [KS12b]) we get

$$\begin{aligned} \partial_t p(t, x, v, z) + \operatorname{div}_x(vp) - \partial_z \left(\left((k^+ Q + k^-) z + f'(Q) v \cdot \nabla_x Q \right) p \right) \\ = (\lambda_0 + \lambda_1 z) \left(q(x, v) \int_V p(v')\, \mathrm{d}v' - p(v) \right) \end{aligned} \tag{2.10}$$

in the velocity jump process case. The equation consists of a combination of the spatial drift term ($\partial_t p + \mathrm{div}_x(vp)$), the drift in the internal variable

$$-\partial_z \left(\left((k^+ Q + k^-)z + f'(Q) v \cdot \nabla_x Q \right) p \right),$$

and a reorientation term (as in equation (2.7)). Equation (2.10) is a hyperbolic equation that fits in the kinetic theory of active particles (see e.g. [Bel08]), which is an extension of the standard kinetic theory to particles with an additional variable, a so-called activity, starting with the famous Boltzmann-equation, but recently also applied to cell migration, see e.g. [Hil06, Hil05, PH13, Alt80].

Remark 2.4.2. *Let us define the turning operator $\mathcal{L}[\lambda]$ as*

$$\mathcal{L}[\lambda]p = \lambda \cdot \left(q(x,v) \int_V p(v') \, \mathrm{d}v' - p(v) \right).$$

This operator describes the change of velocity (here reorientation) from v' to v and thus the reorientation term of equation (2.10) *can be written as $\mathcal{L}[\lambda_0 + \lambda_1 z]p$. Hillen [Hil06] investigated this operator in more detail:*

- *The turning operator defined in the previous equation is a linear Hilbert-Schmidt operator on the weighted space $L^2(V, q^{-1})$. This space consists of all measurable functions such that the corresponding norm induced by the scalar product*

  $$\langle f, \, g \rangle = \int_V f(v) \; g(v) \; \frac{1}{q(v)} \, \mathrm{d}v$$

  is finite.

- *The nullspace of the operator is given by the span of q denoted as usual by $\langle q \rangle$, hence we have for all $f(v) = Cq(v)$ with $C \in \mathbb{R}$ that $\mathcal{L}[\lambda]f = 0$.*

- *The operator $\mathcal{L}[\lambda]$ is invertible on the orthogonal complement $\langle q \rangle^\perp$ with the pseudo inverse given by the multiplication operator with $-\frac{1}{\lambda}$.*

These are the main properties of this operator needed subsequently for handling this mesoscopic model.

Now let us have a look at the previous microscopic model (2.9) incorporating the Wiener process as driving force:

$$\begin{aligned}
\mathrm{d}x &= v \, \mathrm{d}t \\
\mathrm{d}v &= \sqrt{\frac{2(\lambda_0 + \lambda_1 z)}{q(x,v)}} \, \mathrm{d}W_t \\
\mathrm{d}z &= -\left((k^+ Q(x) + k^-)z + f'(Q(x)) v \cdot \nabla_x Q(x) \right) \mathrm{d}t
\end{aligned}$$

The corresponding mesoscopic equation is the well-known Fokker-Planck form (see e.g. [KS12a])

$$\partial_t p(t,x,v,z) + \mathrm{div}_x(vp) - \partial_z\left(\left((k^+Q + k^-)z + f'(Q)v\cdot\nabla_x Q\right)p\right) = (\lambda_0 + \lambda_1 z)\Delta_V\left(\frac{p}{q(x,v)}\right), \quad (2.11)$$

where $p\colon X\times V\times Z\to\mathbb{R}$ denotes as before the (mesoscopic) tumour cell density function. Note that the Fokker-Planck equation here is used in a formal sense, because the rigorous derivation of the Fokker-Planck equation needs much stronger assumptions leading to a strong solution of (2.11).

Remark 2.4.3. *Let us consider the operator*

$$\mathcal{M}[\lambda]p = \lambda\Delta_V\left(\frac{p}{q}\right)$$

with $V=\mathbb{S}^2$. So the essential change between the velocity jump description and the one considered here is the operator acting on the velocity space. Then the following hold:

- *The operator $\mathcal{M}[\lambda]$ generates for all $\lambda\in\mathbb{R}$ a strongly continuous contraction semigroup on the weighted space $L^2(V,q^{-1})$ (confer the first point of remark 2.4.2).*
- *The nullspace of $\mathcal{M}[\lambda]$, $\lambda\in\mathbb{R}$ is given by the span of q.*
- *In the case $d=3$, the only biological relevant one, the inverse of $\mathcal{M}$ with V being a sphere is given by Green's formula using the explicit representation of Green's function.*

Proof. The first statement is clear by theorem 12.40 in [RR06].

For the second statement, assume w.l.o.g. $s=1$ and look at the $L^2(\mathbb{S}^2)$-complete $L^2(\mathbb{S}^2)$-orthogonal system of spherical harmonics (eigenfunctions of the Beltrami operator) (see e.g. [FM12, FS08, Fre12]) $Y_{n,k}$, $n\in\mathbb{N}$ and $k=-n,...,n$. An explicit representation of these is available. So the fully normalized real spherical harmonics are given by

$$Y_{n,k}(\theta,\phi) = \begin{cases} \sqrt{2}\sqrt{\frac{(2n+1)\,(n-|k|)!}{4\,\pi\;(n+|k|)!}}\,P_n^{|k|}(\cos(\theta))\sin(|k|\,\phi) & \text{if } k<0\\ \sqrt{\frac{2n+1}{4\,\pi}}\,P_n^k(\cos(\theta)) & \text{if } k=0\\ \sqrt{2}\sqrt{\frac{(2n+1)\,(n-|k|)!}{4\,\pi\;(n+|k|)!}}\,P_n^k(\cos(\theta))\cos(k\,\phi) & \text{if } k>0 \end{cases}$$

using the standard parametrization of the 2-sphere ($\theta\in[0,\pi]$ and $\phi\in[0,2\,\pi]$) and the associated Legendre polynomial

$$P_n^k(t) = (-1)^k(1-x^2)^{\frac{k}{2}}\frac{\mathrm{d}^k}{\mathrm{d}\,t^k}P_n(t),$$

where $P_n(t)$ is the standard Legendre polynomial. Then the nullspace of the Beltrami operator is given by the span of the zeroth order function $Y_{0,0} \equiv \frac{1}{\sqrt{4\,\pi}} = const.$ Transferring to the case at hand, we see that $\frac{p}{q}$ has to be constant and hence the nullspace of $\mathcal{M}$ is given by $\langle q \rangle$.

For the third statement, we define Green's function on the sphere $\mathbb{S}^2$ as [Fre12]

$$G(\xi, \eta) = \frac{1}{4\pi} \left(\ln(1 - \xi \cdot \eta) + 1 - \ln(2) \right).$$

Then by Green's formula

$$f(\xi) = \frac{q(\xi)}{\lambda} \int\limits_{\mathbb{S}^2} G(\xi, \eta) g(\eta) \, \mathrm{d}\eta$$

solves $\mathcal{M}[\lambda] f = g$ in $\mathbb{S}^2$ subject to the condition $\int\limits_{\mathbb{S}^2} f(\xi) \, \mathrm{d}\xi = 0$. □

Remark on the assumptions:
We assumed the convergence of the empirical density of (2.9) to a solution of the equation (2.11). For more information on this topic and rigorous proofs, we refer to [Var66, SV07] or to chapter 5 in [KS12a].

2.4.3 Modelling Proliferation via Cell-Tissue Interaction

In order to model proliferation, we focus on the different modelling scales and different growth notions. For the latter, there are two distinct possibilities. First, the phenomenological modelling on the microscopic scale by using birth (and correspondingly death) processes is a very detailed way to model population increase, but at the cost of introducing complex stochastic processes (and also more free parameters, which is clearly to avoid). This was done in [Ste00], where also a rigorous proof of the convergence of a microscopic system (without birth and death phenomena and with an SDE for the position only) to a generalized Keller-Segel model can be found. The main problem with this modelling procedure is that, while being accurate on the microscopic scale, it is not clear whether the fine-grained information is necessary, especially if the available data for the model cannot reveal the fine-grained structures. Moreover, clinicians are merely interested in the tumour bulk – an area of high tumour cell concentration, in which for a reasonably sized glioblastoma about 10^9 cells are present, so including cell division is a computational intense task to do. However, with increasing computational power this can be done in reasonable time [HHB$^+$07] and by using massive parallelization [CS14, CS15]. But until we are able to compute the required amount of cells and receive data with a very fine resolution (at the moment we use only data with a

voxel size of 2 mm), we utilize the second growth notion, namely density growth. This has several advantages: As we are interested in population (rather than individual) behaviour, the use of a population growth is the natural way to accomplish this. Moreover, if we only track the cell population within one given voxel (this will be done using finite volumes in chapter 4), we do not depend on finer resolutions and can include a variety of medical data. The microscopic cell scale is the coarsest one to include cell division in a natural way, however, we are merely interested in cell density growth, so we want to include the proliferation on a modelling scale describing a cell density. Typically this is done on the macroscopic scale [RAJRS09, HCS+12], but in this text, we will use the mesoscopic scale for the proliferation modelling. On this scale, we have to do with probability densities (from the averaging of the stochastic multi-particle systems). If we drop the assumption of the normalized integral, we get physical densities (integrable and non-negative functions) for which we can introduce a source term describing the proliferation. This is exactly the way we take to model the proliferation on the mesoscopic scale.

The authors of [EKS16] proposed to include proliferation also on the mesoscopic scale using the go-or-growth hypothesis. In essence it states that a cell either migrates or proliferates, but not simultaneously. While the go-or-growth hypothesis has been confirmed by many studies (see for example [BG99, GKL+96, HES+08]), there are recently a few works providing strong evidence that proliferation is not discontinued in favour for migration [MRP+05, UdJPK09]. Thus we seek for an alternative to modelling proliferation. A way to cope with this is to rely on the binding state of the cell surface receptors, already included in the model at the subcellular scale. Such bindings of receptors are necessary for the intracellular machinery to trigger many essential biological processes, including cell survival and proliferation [UGR99, GG04]. So in [EHS15] we proposed the mesoscopic proliferation term acting on the mesoscopic scale:

$$\mathcal{P}(p) = \mu\left(\int_V \int_Z p(t,x,v,z)\ \mathrm{d}z\ \mathrm{d}v\right) \int_Z Q(x)\chi(x,z,z')p(t,x,v,z')\ \mathrm{d}z'. \tag{2.12}$$

This can be recast directly in the context of the kinetic theory of active particles (KTAP) [Bel08] as proliferation during interaction between the tumour cells (here represented by p, as before) and the ligands of the receptors (here the volume fraction of tissue fibres modelling the ECM, denoted by Q), hence expressing the necessity of ECM-presence for proliferation. The function μ depending on the macroscopic cell density acts as a generic growth rate as in the typical ODE growth models. We select it to be

$$\mu(s) = c_g(1-s), \quad \text{for all } s \geq 0 \tag{2.13}$$

where the constant c_g is a volume growth rate for the tumour cell density. It can be estimated as shown in chapter 4 and [EHS15]. The integral kernel $\chi\colon X \times Z \times Z \to \mathbb{R}^+$ (here called

"proliferation kernel") describes the change of the internal state during proliferation from the state z' to z. We assume it to be a probability density in the second variable z, meaning that the cell is in a valid binding state after mitosis. This is not restrictive. After using moment expansions done in the next section, the macroscopic net effect of the proliferation term $\mathcal{P}$ applied to either model with velocity jump or Gaussian process corresponds to the modified logistic growth

$$\dot{g} = c_g Q(x)(1-g)g.$$

Hence we gain some insight by using this type of modelling instead of a macroscopic growth term like pure logistic or Gompertzian growth: Our approach is more accurate from the modelling perspective, as we have a biological motivation behind the proliferative action rather than only use some (arbitrary) growth term. This insight is directly capable to be interpreted in a clinical context, as the proliferation term acts on a cell density - a quantity that can be observed.

Assumptions about proliferation:

- The proliferation is conditioned by the interaction of cells with the tissue.
- The proliferation kernel $\chi(x, z, z')$ is a probability kernel in the second variable, hence

$$\int_Z \chi(x, z, z')dz = 1$$

and it characterizes the transition from an internal state z' to another state z during mitosis.

2.4.4 From Mesoscopic to Macroscopic Description

The reasons to move on from a mesoscopic to a macroscopic setting are twofold. First, the mesoscopic equation does have a very high-dimensional phase space, in our context of dimension $\dim(X) + \dim(V) + \dim(Z) = 2 \cdot d + 1$. In particular, in the 3D case, this results in solving a time-dependent partial differential equation in seven dimensions, but also in 2D, we need to discretize five dimensions (additional to the time), which is far from being trivial. Nevertheless, this can be done, but if the aim is to personalize medical treatment (using personalized, data-based mathematical modelling), the time needed to solve such a large problem is not feasible.

The second reason to make the transition is that the medical practitioners can only detect a (partial) tumour extent, so there is no reliable initial condition for the velocity and internal binding state, both being in the context of the mesoscopic model. However, the ultimate aim of model validation cannot succeed without reliable information at the initial time. There is also a practical argument against the mesoscopic equation: The units included especially in the velocity variable are much finer than those of the available data, as the typical tumour cell velocity is around $10^{-7}\frac{\mathrm{m}}{\mathrm{s}} = 0.1\frac{\mu\mathrm{m}}{\mathrm{s}}$, whereas the data resolution is around 2 mm. This would render the numerical simulation for the mesoscopic equation on such data error prone. So either we can get access to finer data allowing to handle all problems occurring with fine resolution (like the necessity of parallelization, due to the size of the resulting discretized systems), or we need to employ some scaling technique like hyperbolic [BD08] or parabolic scaling [PH13]. We choose the latter in order to arrive at a diffusion dominated equation, which provides an (at least qualitatively) enhanced description when compared to the existing models [JJHD$^+$15, ARGQ09]. So the time units will be scaled from seconds to days or even weeks, whereas the spatial scale will be converted from micrometres to millimetres, hence to a resolution observable in clinical practice. Thus the variables are transformed as follows: $t \to \varepsilon^2 t$ and $x \to \varepsilon x$ for a small parameter ε.

2.4.5 First Multiscale Model Relying on the Mesoscale Description (2.10)

We already introduced in (2.10) the model (on the mesoscopic scale):

$$\partial_t p + \mathrm{div}_x(vp) - \mathrm{div}_z\left(\left((k^+Q + k^-)z + f'(Q)v\cdot\nabla_x Q\right)p\right) = \mathcal{L}[\lambda(z)]p.$$

Including proliferation via cell-tissue interactions as in (2.12) we get

$$\partial_t p + \mathrm{div}_x(vp) - \mathrm{div}_z\left(\left((k^+Q + k^-)z + f'(Q)v\cdot\nabla_x Q\right)p\right) = \mathcal{L}[\lambda(z)]p + \mathcal{P}(p). \quad (2.14)$$

Here we assume full space solutions in the x variable and homogeneous Dirichlet boundary conditions for the z variable. From the biological interpretation this means that the boundary states (recast in y) 0 and 1 are unlikely. In fact $y = 0$ means that no receptor is bound, which corresponds to a dead cell, while $y = 1$ means that all receptors are bound, a state never observed in reality.

Lemma 2.4.3. *Let $Q \in W^{1,\infty}(X)$ and $q \in L^\infty(X \times V)$ for $X = \mathbb{R}^d$, $V = s\mathbb{S}^{d-1}$ and $Z = (-f(Q), 1 - f(Q))$. Then the equation (2.14) is well-posed in the sense that there exists a unique solution in $L^\infty(0,T; L^1 \cap L^\infty(X \times V \times Z))$ to initial data p_0 fulfilling $p_0 \in L^1(\mathbb{R}^n \times V \times Z) \cap L^\infty(\mathbb{R}^n \times V \times Z)$. This solution stays non-negative, given non-negative initial data.*

Proof. See the proofs [KS12b] or [NU16]. Using the local Lipschitz (and so the growth condition) on μ, we can apply the localized proof (Theorem 4) in [NU16] with the additional term of $C(R)\,||f^j - f^{j-1}||_{L^\infty(0,T_0;L^1(R^n\times V\times Y))}$ (in the notations of the paper [NU16]) on the right hand side in the third equation of the proof. □

Remark 2.4.4. *It is possible to relax the assumptions on the data in the previous lemma and allow for more general terms in the equation. This can be done via the much more general setting in [LS14]. In that reference there is however, no non-linear proliferation term.*

Now we use parabolic scaling for the previous equation to end up with

$$\varepsilon^2\partial_t p + \varepsilon\,\mathrm{div}_x(vp) - \mathrm{div}_z\left(\left((k^+Q + k^-)z + \varepsilon f'(Q)v\cdot\nabla Q\right)p\right) = \mathcal{L}[\lambda(z)]p + \varepsilon^2\mathcal{P}(p). \quad (2.15)$$

The parabolic scaling can be seen to be the correct scaling (regarding the space and time scales of interest) as in [HHW10, HP13]. Therefore we introduce the reference quantities $\hat{x}$ and $\hat{v}$. Our whole approach is data motivated, so we assume the characteristic length $\hat{x}$ to be around 2 mm (the side length of a voxel). The characteristic speed can be set to different reasonable values: first, and this is the approach we follow, set $\hat{v}$ to be the cell speed (between $10^{-7}\frac{\mathrm{m}}{\mathrm{s}}$ and $10^{-6}\frac{\mathrm{m}}{\mathrm{s}}$). Another reasonable quantity would be the measurable invasion speed of the tumour bulk into the neighbouring tissue. This will be typically much lower than the average speed of a single cell. So we are conservative and use the speed of a single cell as reference. Then the unitless parameter ε is defined via [HHW10]

$$\varepsilon = \frac{\hat{v}}{\lambda\,\hat{x}},$$

where λ is here the average turning rate (around $0.8\,\frac{1}{\mathrm{s}}$). This leads us to an ε of the order of 10^{-3} (which is very diffusive). This approach (using the reference space and velocity scales) leads us to the parabolic scaling [HHW10, HP13]. Note that the presented motivation is not a non-dimensionalization, because the units of the lengths and velocities stay the same. In [NU16] there was a discussion whether to use parabolic or hyperbolic scaling (or something in between) in favour of the hyperbolic scaling for the type of kinetic equation we consider. However, the argumentation cannot be applied to our setting, because our velocity scale is very small compared to the length scale (represented by $\hat{x}$), so we cannot apply hyperbolic scaling and use at the same time the medical data. Note that we scaled also the proliferation term $\mathcal{P}$ with ε^2. This comes from the fact that, integrating (2.14) over $X\times V\times Z$ using the homogeneous boundary conditions in z, we end up with the ODE

$$\partial_t\bar{p} = \overline{\mathcal{P}(p)},$$

which has to be scaled in a compatible way, known to the literature of parabolic scaling, where this is done exactly in the same manner [BBNS12]. The upper bar in the previous equation is the short hand notation for the integration over $X \times V \times Z$, not to be confused with the same notation in [EHKS14, EKS16, EHS15, HS16] standing for another average. One can see this best if applied to the proliferation rate (included in $\mathcal{P}$). Using the parabolic scaling, the time units change from seconds to days (with ε^2). So the proliferation rate has to be transformed with ε^2 in order to act on the correct time scale.

Now we define the moments:

$$\begin{aligned} m(t,x,v) &= \int_Z p(t,x,v,z)dz & M(t,x) &= \int_V m(t,x,v)dv \\ m^z(t,x,v) &= \int_Z zp(t,x,v,z)dz & M^z(t,x) &= \int_V m^z(t,x,v)dv \\ m^{zz}(t,x,v) &= \int_Z z^2 p(t,x,v,z)dz & M^{zz}(t,x) &= \int_V m^{zz}(t,x,v)dv. \end{aligned}$$

Then we form moment equations of zeroth and first order: Let us integrate (2.15) with respect to z and use the homogeneous Dirichlet boundary conditions in z to get

$$\begin{aligned} \varepsilon^2 \partial_t m + \varepsilon \operatorname{div}_x(vm) = \lambda_0 \left(qM - m\right) + \lambda_1 \left(qM^z - m^z\right) \\ + \varepsilon^2 \mu(M) Q \int_Z \int_Z \chi(x,z,z')p(z')dz'dz. \end{aligned} \tag{2.16}$$

Multiplying (2.15) with z and integrating with respect to z, we have the first order moment equation

$$\begin{aligned} &\varepsilon^2 \partial_t m^z + \varepsilon \operatorname{div}_x(vm^z) + (k^+ Q + k^-)m^z + \varepsilon f'(Q) v \cdot \nabla_x Q m \\ &\quad = \lambda_0 \left(qM^z - m^z\right) + \lambda_1 \left(qM^{zz} - m^{zz}\right) + \varepsilon^2 \mu(M) Q \int_Z \int_Z z\chi(x,z,z')p(z')dz'dz. \end{aligned} \tag{2.17}$$

As already mentioned in the modelling section for the proliferation term, we assume that $\chi(x,z,z')$ is a probability kernel in z, hence the double integral in equation (2.16) can be computed using the Tonelli theorem

$$\int_Z \int_Z \chi(x,z,z')p(z')dz'dz = \int_Z p(z')dz' = m(t,x,v). \tag{2.18}$$

In the light of the last equation, we see that the proliferation term, yet unusual, will have the net effect on the macroscopic scale as a modified logistic growth term. This is due to the choice (2.13). The pure logistic growth is used in many models for tumour growth (see

e. g. [VA82, AWLL03, MBFVP94]). We look now at the moment system (2.16) and (2.17). We neglect the second order moments of p with respect to z, because z is near 0 (confer to Lemma 2.4.2), and using Hilbert expansions

$$\Xi = \sum_{k=0}^{\infty} \Xi_k \varepsilon^k$$

for $\Xi \in \{m, M, m^z, M^z\}$. Collecting the corresponding powers of ε, we have:

ε^0:

$$\begin{aligned} 0 &= \lambda_0 \left(qM_0 - m_0\right) + \lambda_1 \left(qM_0^z - m_0^z\right) \\ (k^+Q + k^-)m_0^z &= \lambda_0 \left(qM_0^z - m_0^z\right). \end{aligned}$$

Integrating the last equation with respect to v, we get

$$(k^+Q + k^-)M_0^z = 0,$$

and so

$$(k^+Q + k^- + \lambda_0)m_0^z = 0.$$

Hence we have the identities

$$\begin{aligned} M_0^z &= 0 \\ m_0^z &= 0 \\ m_0 &= qM_0. \end{aligned}$$

This is expected, because it resembles the equilibrium distribution of $\mathcal{L}[\lambda]$. Now looking at the first power of ε:

ε^1:

$$\begin{aligned} \mathrm{div}_x(vm_0) &= \lambda_0 \left(qM_1 - m_1\right) + \lambda_1 \left(qM_1^z - m_1^z\right) \\ \mathrm{div}_x(vm_0^z) + (k^+Q + k^-)m_1^z + f'(Q)v \cdot \nabla_x Q m_0 &= \lambda_0 \left(qM_1^z - m_1^z\right) \end{aligned} \tag{2.19}$$

Integrating the latter equation with respect to v and using the assumption that the tissue fibre orientation distribution q is symmetric in v, we get

$$(k^+Q + k^-)M_1^z = 0.$$

The mentioned assumption corresponds to having undirected fibres. In the case of diffusion tensor imaging data used in the sequel, this is valid, however, in general, especially in presence of constellations like forking or crossing of fibres resolved with higher (angular) resolution (confer data chapter 3), this assumption has to be revisited. If it fails for too many voxels,

one needs either to change the model accordingly or use another scaling or another closure technique.

From (2.19) we compute

$$m_1^z = -\frac{f'(Q)v \cdot \nabla_x Q q M_0}{k^+ Q + k^- + \lambda_0}. \tag{2.20}$$

Inserting this into the first equation in (2.19), we get

$$m_1 = qM_1 - \frac{1}{\lambda_0}\operatorname{div}_x(vqM_0) + \frac{1}{\lambda_0}\frac{\lambda_1}{\lambda_0 + k^+ Q + k^-} f'(Q) q(v) v \cdot \nabla_x Q M_0. \tag{2.21}$$

ε^2:

$$\begin{aligned}
&\partial_t m_0 + \operatorname{div}_x(vm_1) = \lambda_0(qM_2 - m_2) + \lambda_1(qM_2^z - m_2^z) + \int_Z \mathcal{P}(p)\,\mathrm{d}z \\
&\partial_t m_0^z + \operatorname{div}_x(vm_1^z) + (k^+ Q + k^-) m_2^z + f'(Q) v \cdot \nabla_x Q m_1 \\
&\qquad = \lambda_0(qM_2^z - m_2^z) + \int_Z z\mathcal{P}(p)\,\mathrm{d}z
\end{aligned} \tag{2.22}$$

For the deduction of the macroscopic equation, we integrate the first equation of (2.22) with respect to v and get

$$\partial_t M_0 + \operatorname{div}_x\left(\int_V v m_1(v) dv\right) = \mu(M) Q M_0 = \mu(M_0) Q M_0 + \mathcal{O}(\varepsilon),$$

where we used (2.18). By using the explicit representation of m_1 from (2.21) we compute

$$\begin{aligned}
\int_V v m_1\,\mathrm{d}v = \int_V v q(v)\,\mathrm{d}v M_1 - \operatorname{div}_x\left(\int_V \frac{v\otimes v}{\lambda_0} q(v)\,\mathrm{d}v\, M_0\right) \\
+ \frac{\lambda_1}{k^+ Q + k^- + \lambda_0} f'(Q) \int_V \frac{v\otimes v}{\lambda_0} q(v)\,\mathrm{d}v \cdot \nabla_x Q M_0,
\end{aligned}$$

and inserting this in the equation obtained above we arrive to the leading order at the macroscopic equation

$$\partial_t M_0 - \operatorname{div}_x \operatorname{div}_x (D M_0) + \operatorname{div}_x (g D \nabla_x Q M_0) = \mu(M_0) Q M_0, \tag{2.23}$$

where we introduced the notations

$$D(x) = \int_V \frac{v\otimes v}{\lambda_0} q(x,v) dv, \qquad g(x) = \frac{\lambda_1}{\lambda_0 + k^+ Q + k^-} f'(Q). \tag{2.24}$$

The so-called tumour diffusion tensor D describes the mean spread of the tumour cell density in a position x. It is parametrized with the aid of the medical data, so the diffusion coefficient will be higher in directions in which the fibres are oriented, and lower elsewhere. The function g describes the drift velocity of the convection term depending on the volume fraction of tissue fibres.

Remark 2.4.5. *- The equation* (2.23) *depends strongly on the medical data, as the (mesoscopic) tissue fibre orientation q influences the diffusion tensor and the drift velocity.*

- The deduction of this equation with parabolic scaling and moment equations is necessary, as for the direct presumption of a convection-diffusion-reaction equation as in [RAJRS09, HCS+12] there is no natural way to include real data without further assumptions. However, in our setting the data is automatically scaled (with the cell speed s, hidden in the definition of V) and averaged (with the integration with respect to v) to fit the equation.

- The proliferation term describing the onset of proliferation via cell-tissue interactions is transferred to the macroscopic scale, where the same interpretation as interaction is possible.

Theorem 2.4.2. *Now let $\Omega \subset \mathbb{R}^d$ be a connected and open set with Lipschitz boundary. Assume that $Q \in W^{1,\infty}(\Omega)$ and $q \in \{\varphi \in L^\infty(\Omega \times V);\ \partial_x \varphi \in L^\infty(\Omega \times V)\}$. Let the initial condition $u_0 \in L^2(\Omega)$ be non-negative. Then the equation* (2.23) *has a non-negative weak solution.*

Proof. See the appendix to this chapter. □

Remark 2.4.6 (On the assumed regularity of the data)**.** *In the previous theorem we assumed a lot of regularity for the functions Q and q, both in space and for q also in velocity. This directly connects to the assumption that Q and the water diffusion tensor D_W are at least in $W^{1,\infty}(X)$.*

It is not reasonable to try to include the actual regularity of the data, as the space is not given, instead we have a discretization of the brain given as a voxel grid. The data consist of mean value reconstructions of the desired quantities (now in a not discretized sense) over a voxel. Thus we may assume without contradicting reality that the non-discretized quantities are quite regular. This means that for the well-posedness we are merely interested in solutions on a non-discretized space, whereas the numerical solution of the equations will take place on the discretized space.

The first model in a nutshell:

Via parabolic scaling and the assumption that the fibre tissue orientation is symmetric, the equation

$$\partial_t p + \operatorname{div}_x(vp) - \operatorname{div}_z\left(\left((k^+Q + k^-)z + f'(Q)v \cdot \nabla_x Q\right)p\right) = \mathcal{L}[\lambda(z)]p + \mathcal{P}(p)$$

leads to

$$\partial_t \rho - \operatorname{div}_x \operatorname{div}_x (D\rho) + \operatorname{div}_x (gD\nabla_x Q\rho) = \mu(\rho)Q\rho.$$

So the macroscopic description of the model with velocity jump process leads to a convection-diffusion-reaction equation with data based terms in every part of it.

There are some differences between an equation like (2.23) and the prototype of a reaction-convection-diffusion equation (like (2.1)) as in [HCS$^+$12]. The form of the diffusion

$$\operatorname{div}_x \operatorname{div}_x (D\rho)$$

or equivalently

$$\operatorname{div}_x (D\nabla_x \rho) + \operatorname{div}_x (\operatorname{div}_x(D)\, \rho) \tag{2.25}$$

is distinct. It is often referred to as myopic diffusion. The difference is an additional convection term (best seen in (2.25)). While myopic diffusion can also be deduced from a monoscale model (see e. g. [PH13]), our model (2.23) accounts for a different phenomenon, namely the interplay of the reorientation term (also existent in [PH13]) and the subcellular bindings (missing in [PH13]) leading to the additional (in comparison to [PH13]) drift term

$$\operatorname{div}_x (g(Q)D \cdot \nabla_x Q\rho)\,. \tag{2.26}$$

This is a haptotactic-like term describing the guidance of the brain structure. One may wonder, why the additional drift term guides the cell density in direction $D \cdot \nabla_x Q$ instead of $\nabla_x Q$. The obvious cause is the deduction of this term, however, in (2.26) happens more than pure reorientation in the direction of the steepest ascent of Q. This would be modelled via

$$\operatorname{div}_x (\gamma \nabla_x Q\rho)\,,$$

where γ is some constant, whereas the term (2.26) also includes the brain structure via both, the tumour diffusion tensor and the volume fraction of tissue fibres.

Thus the haptotactic sensitivity in the additional drift term 2.26 depends on the subcellular dynamics via the $g(Q)$ and the $\nabla_x Q$ and the tumour diffusion tensor D.

2.4.6 Second Multiscale Model Relying on the Mesoscopic Description (2.11)

Now let us take a closer look at the second model (this time dropping the assumption of undirected fibres):

$$\partial_t p + \operatorname{div}_x(vp) - \partial_z\left(\left((k^+Q + k^-)z + f'(Q)v\cdot\nabla_x Q\right)p\right) = (\lambda_0 + \lambda_1 z)\Delta_V\left(\frac{p}{q}\right).$$

We introduced this model class to handle instant cell orientation and irregular shape changes, both happening in cell movement. Due to reorientations on faster time scales, the cells will diffuse slower than in the previous model 2.14, so it will predict a different, less aggressive tumour spread (slower, but also different in shape, see figure 4.2). The advantage is that we may drop the assumption of the undirected fibres, as it is not necessary for the parabolic scaling. Instead, we use the assumption of a fast relaxation of the cell orientation to the fibres, hence we assume instant reorientations for which we introduced this model class.

Including the proliferation term, we get

$$\partial_t p + \operatorname{div}_x(vp) - \partial_z\left(\left((k^+Q + k^-)z + f'(Q)v\cdot\nabla_x Q\right)p\right) = (\lambda_0 + \lambda_1 z)\Delta_V\left(\frac{p}{q}\right) + \mathcal{P}(p). \quad (2.27)$$

As in the previous model, we use parabolic scaling on (2.27) to end up with

$$\varepsilon^2\partial_t p + \varepsilon\operatorname{div}_x(vp) - \partial_z\left(\left((k^+Q + k^-)z + \varepsilon f'(Q)v\cdot\nabla_x Q\right)p\right) = (\lambda_0 + \lambda_1 z)\Delta_V\left(\frac{p}{q}\right) + \varepsilon^2\mathcal{P}(p). \quad (2.28)$$

Note that the proliferation term was scaled accordingly to the previous model. Using moment equations and Hilbert expansions as before along with the same notations, we get

$$\begin{aligned}
&\varepsilon^2\partial_t m + \varepsilon\operatorname{div}_x(vm) = \Delta_V\left(\frac{\lambda_0 m + \lambda_1 m^z}{q}\right) \\
&\qquad + \varepsilon^2\mu(M)Q\int_Z\int_Z \chi(x,z,z')p(z')\,\mathrm{d}z'\;\mathrm{d}z \\
&\varepsilon^2\partial_t m^z + \varepsilon\operatorname{div}_v(vm^z) + (k^+Q + k^-)m^z + \varepsilon f'(Q)v\cdot\nabla_x Q m \\
&\quad = \Delta_V\left(\frac{\lambda_0 m^z + \lambda_1 m^{zz}}{q}\right) + \varepsilon^2\mu(M)Q\int_Z\int_Z z\chi(x,z,z')p(z')\,\mathrm{d}z'\;\mathrm{d}z.
\end{aligned} \quad (2.29)$$

Neglecting the second order moments in z we arrive at the zeroth order of the Hilbert expansions

ε^0 :

$$\begin{aligned} 0 &= \Delta_V \left(\lambda_0 m_0 + \lambda_1 m_0^z\right) \\ (k^+ Q + k^-) m_0^z &= \Delta_V \left(\frac{\lambda_0}{q} m_0^z\right). \end{aligned}$$

We focus on the biologically relevant case $d = 3$ and assume without loss of generality $s = 1$. For this constant cell speed the operator Δ_V is given as the Laplace-Beltrami operator $\Delta^\star$ on the unit sphere. Otherwise (for general s) the operator Δ_V is given by $\frac{\Delta^\star}{s^2}$. Hence the previous equations can be recast on the unit sphere as

$$\begin{aligned} 0 &= \Delta^\star \left(\frac{\lambda_0 m_0 + \lambda_1 m_0^z}{q}\right) \\ (k^+ Q + k^-) m_0^z &= \Delta^\star \left(\frac{\lambda_0}{q} m_0^z\right). \end{aligned}$$

The Laplace-Beltrami operator on the unit sphere has the null-space spanned by constant functions [FM12], hence the first moment equation is solved easily:

$$\lambda_0 m_0 + \lambda_1 m_0^z = q(x, v) C \tag{2.30}$$

with a generic constant C, that may depend on t and x. To compute it, we integrate the previous identity with respect to v and get

$$\lambda_0 M_0 + \lambda_1 M_0^z = C. \tag{2.31}$$

Lemma 2.4.4. *Let us consider the equation* $\frac{k^+ Q + k^-}{\lambda_0} q(x, v) g(v) = \Delta^\star g$. *It has the only solution* $g = 0$ *and hence* $m_0^z = 0$ *and* $M_0^z = 0$.

Proof. That 0 is indeed a solution to this equation is easy to see. Now let us compute

$$0 \leq \left\langle \frac{k^+ Q + k^-}{\lambda_0} q g, g \right\rangle = \langle g, \Delta^\star g \rangle = - \langle \nabla^\star g, \nabla^\star g \rangle \leq 0,$$

where we used that q is uniformly positive (i. e. $\inf_{x \in X,\ v \in V} q(x, v) \geq \alpha > 0$). Due to this definiteness, we conclude that the previous equation can only be fulfilled by the constant $g = 0$ almost everywhere. Hence $0 = g = \frac{m_0^z}{q}$ and the assertion follows. □

Lemma 2.4.4 gives also the possibility to obtain the relationship $m_0 = q M_0$ by applying it to $g = \frac{\lambda_0 m_0^z}{q}$ and using (2.30) and (2.31).

Coming now to the first order in ε we get from (2.29):

ε^1 :

$$\begin{aligned} \operatorname{div}_x(v m_0) &= \Delta_V \left(\frac{\lambda_0 m_1 + \lambda_1 m_1^z}{q}\right) \\ \operatorname{div}_x(v m_0^z) + (k^+ Q + k^-) m_1^z + f'(Q) v \cdot \nabla_x Q m_0 &= \Delta_V \left(\frac{\lambda_0 m_1^z}{q}\right). \end{aligned} \tag{2.32}$$

As before, we consider the Laplace-Beltrami operator (assuming w.l.o.g. $s = 1$):

$$\operatorname{div}_x(vm_0) = \Delta^\star\left(\frac{\lambda_0 m_1 + \lambda_1 m_1^z}{q}\right)$$
$$\operatorname{div}_x(vm_0^z) + (k^+Q + k^-)m_1^z + f'(Q)v \cdot \nabla_x Q m_0 = \Delta^\star\left(\frac{\lambda_0 m_1^z}{q}\right).$$

Using in this context Green's formula for the sphere, we get from (2.32) the identity

$$\lambda_0 m_1 + \lambda_1 m_1^z = q(v) \int_{\mathbb{S}^2} G(v, v') \operatorname{div}_x(v' q(v') M_0) \ \mathrm{d}v', \tag{2.33}$$

where $G(v, v')$ is Green's function on the 2-sphere, which can be explicitly given [Fre12]:

$$G(\xi, \eta) = \frac{1}{4\pi}\left(\ln\left(\frac{1 - \xi \cdot \eta}{2}\right) + 1\right), \tag{2.34}$$

and this Green function solves the problem with respect to the average value 0. One can clearly consider different offset values, but this would introduce a new free parameter, which is clearly not what we want to do. This offset value would be integrated away. For the solution of the second equation, we need a further assumption, as this was also the case in the velocity jump model. Here the assumption is not that the tissue fibre orientation density q is symmetric, but that $\frac{m_1^z}{q}$ is near constant (in v). This is connected to the convergence of the semigroup generated by the operator $\Delta_V\left(\frac{\cdot}{q}\right)$ for $t \to \infty$.

Under this assumption, we have

$$m_1^z = -\frac{f'(Q)v \cdot \nabla_x Q}{k^+Q + k^-} q(v) M_0, \tag{2.35}$$

which is almost the same as in the previous results for the velocity jump case. The only change is that the denominator in the previous equation (2.35) is not $k^+Q + k^- + \lambda_0$, but λ_0 less.

Now considering the first ε^2 equation:

$$\partial_t m_0 + \operatorname{div}_x(v\, m_1) = \Delta^\star\left(\frac{\lambda_0 m_2 + \lambda_1 m_2^z}{q}\right) + \int_Z \mathcal{P}(p) \ \mathrm{d}z. \tag{2.36}$$

For the deduction of a macroscopic limit equation, we integrate (2.36) with respect to v and get

$$\partial_t M_0 + \operatorname{div}_x\left(\int_V v m_1 dv\right) = \mu(M_0) Q M_0 + \mathcal{O}(\varepsilon).$$

What remains is to evaluate the term $\int\limits_V vm_1 dv$. From (2.33)

$$\begin{aligned}\int\limits_{\mathbb{S}^2} vm_1 dv &= \int\limits_{\mathbb{S}^2} -\frac{\lambda_1}{\lambda_0} vm_1^z dv + \frac{1}{\lambda_0}\int\limits_{\mathbb{S}^2} vq(v)\int\limits_{\mathbb{S}^2} G(v,v')\,\mathrm{div}_x(v'q(v')M_0)dv'dv \\ &= I + II.\end{aligned} \tag{2.37}$$

The first (and easy) integral to compute is by (2.35)

$$\begin{aligned}I &= \int\limits_{\mathbb{S}^2} \frac{\lambda_1 f'(Q)}{\lambda_0(k^+Q + k^-)} v\otimes v\cdot\nabla_x Q q(v) M_0 dv \\ &= \tilde{g}(Q) D\nabla_x Q M_0,\end{aligned}$$

where we used the notation

$$\tilde{g} = \lambda_1 f'(Q)(k^+Q + k^-)^{-1}. \tag{2.38}$$

The tensor D is the same as in the previous model (see (2.24)). So all in all, the haptotactic-like drift term is in the model driven by the Wiener process qualitatively the same as in the velocity jump case. For the second term in (2.37) we compute $\mathrm{div}_x(v'q(x,v')M_0(t,x))$ as $v'\nabla_x M_0(t,x)q(x,v') + v'M_0(t,x)\nabla_x q(x,v')$. Then we have

$$II = \tilde{D}\nabla_x M_0 + \tilde{U}M_0,$$

where we introduced the notations

$$\begin{aligned}\tilde{D}(x) &= \int\limits_{\mathbb{S}^2}\int\limits_{\mathbb{S}^2} G(v,v')q(x,v')q(x,v)\frac{v\otimes v'}{\lambda_0}\,\mathrm{d}v'\,\mathrm{d}v \\ \tilde{U}(x) &= \int\limits_{\mathbb{S}^2}\int\limits_{\mathbb{S}^2} G(v,v')vq(x,v)v'\cdot\nabla_x q(x,v')\frac{1}{\lambda_0}\,\mathrm{d}v'\,\mathrm{d}v.\end{aligned} \tag{2.39}$$

So the macroscopic equation is given by

$$\partial_t M_0 + \mathrm{div}_x\left(\tilde{D}(x)\nabla_x M_0\right) + \mathrm{div}_x\left(\left(\tilde{U}(x) + \tilde{g}(Q)D\nabla_x Q\right)M_0\right) = \mu(M_0)QM_0. \tag{2.40}$$

Note 2.4.3. - *We did the scaling procedure for $s = 1$ in order to clarify the presentation. It can be done using $s \neq 1$ leading to an operator $s^{-2}\Delta^\star$ and so to many multiplications by s^2 (which we wanted to avoid).*

- *In comparison to the first model, there is a need to compute the additional quantities*

$$\int\limits_{\mathbb{S}^2}\int\limits_{\mathbb{S}^2} G(\xi,\eta)q(\xi)q(\eta)\xi\otimes\eta\;\,\mathrm{d}\xi\,\mathrm{d}\eta$$

$$\int\limits_{\mathbb{S}^2}\int\limits_{\mathbb{S}^2} G(\xi,\eta)q(\xi)\xi\eta\cdot\nabla_x q(\eta)\;\,\mathrm{d}\xi\,\mathrm{d}\eta = \frac{1}{2}\nabla_x\cdot\tilde{D}.$$

The last identity follows from the symmetry of Green's function with respect to ξ and η.

- *Although the last equation is at first sight surprising, since it looks like an inverse diffusion equation, it is not, because the diffusion tensor $\tilde{D}$ is negative definite (as proven below).*
- *On the numerical level, this equation needs some caution in the implementation due to the additional quantities (so we really need to compute a complete data set of the first model and an additional tensor as well as an additional vector per point). The difficulty, especially in three dimensions, is to hold the required data in memory, otherwise the computer will be very slow by swapping a lot. Fortunately this issue can be handled by using compact data structures (*`mat::fixed⟨3,3⟩` *from armadillo and C++ standard* `vectors`*) and storing only the necessary data for the active voxels in the implementation. Then the data expands to less than 4 gigabyte in memory when used with the resolution of about 160000 voxel.*

Remark 2.4.7. *The diffusion tensor $\tilde{D}$ is negative definite.*

Proof. Consider

$$\int_{\mathbb{S}^2}\int_{\mathbb{S}^2} \xi \otimes \eta G(\xi,\eta) q(\xi) q(\eta)\,\mathrm{d}\eta\,\mathrm{d}\xi$$

and multiply it with $a \in \mathbb{R}^3$:

$$a^T \int_{\mathbb{S}^2}\int_{\mathbb{S}^2} \xi \otimes \eta G(\xi,\eta) q(\xi) q(\eta)\,\mathrm{d}\eta\,\mathrm{d}\xi a = \int_{\mathbb{S}^2}\int_{\mathbb{S}^2} (a\cdot\xi)(a\cdot\eta) G(\xi,\eta) q(\xi) q(\eta)\,\mathrm{d}\eta\,\mathrm{d}\xi.$$

This can be reformulated as

$$\int_{\mathbb{S}^2} (a\cdot\xi) q(\xi) z(\xi)\,\mathrm{d}\xi,$$

where z solves the equation

$$\Delta^\star z(\xi) = q(\xi)(a\cdot\xi)$$

with the normalization $\int_{\mathbb{S}^2} z(\xi)\,\mathrm{d}\xi = 0$.

Let us consider now

$$\begin{aligned}\int_{\mathbb{S}^2} (a\cdot\xi) q(\xi) z(\xi)\,\mathrm{d}\xi &= \int_{\mathbb{S}^2} \Delta^\star z z\,\mathrm{d}\xi \\ &= -\int_{\mathbb{S}^2} |\nabla^\star z|^2\,\mathrm{d}\xi \le 0.\end{aligned}$$

So we see that the diffusion tensor $\tilde{D}$ is negative semidefinite and it remains to show the definiteness. For this assume the left hand side of the previous equation to be 0. So the function z has vanishing surface gradient on the sphere, hence it is constant, but subject to the normalization. The only possible constant is 0 itself and this shows the remaining definiteness. □

Theorem 2.4.3. *Let Ω be a connected and open set with Lipschitz boundary and assume that $Q \in W^{1,\infty}(\Omega)$ and $q \in \{\xi \in L^\infty(\Omega \times V); \partial_x \xi \in L^\infty(\Omega \times V)\}$. Let $u_0 \in L^2(\Omega)$. Then equation* (2.40) *with respect to no-flux boundary conditions is well-posed in the sense that there exists a weak solution. This solution is almost everywhere non-negative, given non-negative initial data.*

Proof. See the appendix to this chapter. □

The second model in a nutshell:

Via parabolic scaling and the assumption that the equation $\partial_t g = \Delta_V \left(\frac{g}{q}\right)$ is near steady state, so $g(t,x,v) \approx q(x,v) \int\limits_V g(t,x,v)\ \mathrm{d}v$, the equation

$$\partial_t p + \mathrm{div}_x(vp) - \mathrm{div}_z\left(\left((k^+Q + k^-)z + f'(Q)v \cdot \nabla_x Q\right)p\right) = (\lambda_0 + \lambda_1 z)\Delta_V\left(\frac{p}{q}\right) + \mathcal{P}(p)$$

leads to

$$\partial_t \rho + \mathrm{div}_x\left(\tilde{D}\nabla_x \rho\right) + \mathrm{div}_x\left(\left(\tilde{U} + \tilde{g}D\nabla_x Q\right)\rho\right) = \mu(\rho)Q\rho$$

with the coefficients given by (2.39) and (2.38). So, as in the previous case, the macroscopic description of the model with the Wiener process as driving force of the microlevel dynamics consists of a convection-diffusion-reaction equation with data based terms.

The additional assumption can be interpreted in a way that the cells eventually orient along the fibre tracts and so the tissue fibre orientation $q(x,v)$ prescribes the orientation of the cell density p.

Also in this case we see the myopic diffusion (or a myopic-like) diffusion in the term

$$\mathrm{div}_x\left(\tilde{D}\nabla\rho\right) + \mathrm{div}_x\left(\tilde{U}\rho\right),$$

and an additional drift term

$$\mathrm{div}_x\left(\tilde{g}(Q)D\nabla_x Q\rho\right)$$

stemming from the interplay of the subcellular term and the reorientation (this time via the operator Δ_V). We write myopic-like diffusion, as the drift velocity $\tilde{U}$ is not $\mathrm{div}_x \tilde{D}$, but half of it.

Concluding, in our modelling via parabolic scaling we proposed two different model classes, connected to each other, leading to comparable equations on the macroscopic scale. The first scaling was done in [EHKS14] and including the proliferation term in [EHS15], whereas the scaling with the Wiener process driven model is yet unpublished.

2.5 Appendix: Well-posedness theory

Let $T \in \mathbb{R}_{>0}$ be fixed and consider equations of the type

$$\begin{aligned} &\partial_t u - \operatorname{div}_x \left(A(x,t)\nabla_x u - B(x,t)u\right) + G(x,t,u) = 0 \quad \text{in } \Omega \times (0,T) \\ &n \cdot \nabla_{A,B} := n \cdot \left(A(x,t)\nabla u - B(x,t)u\right) = 0 \quad \text{on } \partial\Omega \times (0,T) \\ &u(0) = u_0(x) \quad \text{in } \Omega \times \{0\} \end{aligned} \tag{2.41}$$

in a Lipschitz region Ω.

Assumptions:

We require in the following that A and B are continuous in time and essentially bounded in space. The diffusion tensor A shall be coercive, so $\xi A(x,t)\xi \geq c_0|\xi|^2$ for almost every $x \in \Omega$ and every $t \in (0,T)$. Here $c_0 > 0$ and independent of space and time.

The growth function G shall be continuous in time, essentially bounded in space and continuous in the solution variable u. Moreover it has to satisfy $G(x,t,0) = 0$ for almost all $x \in \Omega$ and $t \in (0,T)$. As we are only interested in cell densities, where we cannot assign any meaning to negative values u, we assume that $G(x,t,u) = 0$ for $u \leq 0$. In the case of the equations (2.23) and (2.40), we will assume that the modified logistic growth is only valid for non-negative values. This means in this special context, that the growth function G satisfies $G(x,t,u) = -Q(x)u(1-u)$ for all $u > 0$. Hence it holds, that $|G(x,t,u)| \leq C(1+|u|)$ for all $u \in \mathbb{R}$.

Let us define the Gelfand triple $(V, H, V^\star)$ with $V = H^1(\Omega)$ and $H = L^2(\Omega)$. We look for a solution u in the space

$$W := \left\{ v \in L^2(0,T,V), v' \in L^2(0,T,V^\star) \right\}.$$

Let us define (as in [HS16]) the time-dependent operators $\mathcal{A}$ and $\mathcal{G}$ by

$$\langle \mathcal{A}(t)u, v\rangle := \int_\Omega \left(A(x,t)\nabla u - B(x,t)u\right) \cdot \nabla v \,\mathrm{d}x \quad \text{for } u, v \in W \quad \text{and}$$

$$\langle \mathcal{G}(t)u, v\rangle := \int_\Omega G(x,t,u)v \,\mathrm{d}x \quad \text{for } u, v \in W.$$

The operators $\mathcal{A}$ and $\mathcal{G}$ are continuous in the time variable.

Remark 2.5.1. *The operator $\mathcal{A}(t) : V \to V^\star$ for all times t satisfy Gardings inequality*

$$\langle \mathcal{A}u, u\rangle \geq c_1|u|_V^2 - c_2|u|_H^2$$

with time independent constants $c_1 > 0$ and $c_2 \geq 0$.

Proof. Apply Theorem 5.1 of [Sho11]. □

From now on assume that $c_2 = 0$. Otherwise we can transform the equation (2.41) with $\hat{u} = \exp(c_2 t)u$ into an equivalent problem fulfilling the usual coercivity condition

$$\langle \mathcal{A}u, u\rangle \geq c_1|u|_V^2.$$

Theorem 2.5.1 (Theorem 1 in [HS16])**.** *Let $u_0 \in H$ be given. Under the previous assumptions there exists a solution u in the space W in the sense that*

$$-\int_0^T \langle v'(t), u(t)\rangle_{V^\star,V}\,\mathrm{d}t + \int_0^T \langle \mathcal{A}(t)u, v\rangle\,\mathrm{d}t + \int_0^T \langle \mathcal{G}(t)u, v\rangle\,\mathrm{d}t = \langle u_0, v(0)\rangle_H$$

for all $v \in W$ with $v(T) = 0$.

Proof. Confer to the proofs in section 3.3.6 of [Ruz06] of section III.4 of [Sho13] □

Lemma 2.5.1. *For almost everywhere non-negative initial values $u_0 \in L^2(\Omega)$, the solution u of* (2.41) *remains non-negative almost everywhere.*

Proof. We are adapting the proof in section 4.2 in [Yag09]. So let H be a $C^{1,1}$ cutoff function such that H is given by $H(u) = \frac{1}{2}u^2 1_{u<0}$. Then we have

$$\begin{aligned}
\frac{\mathrm{d}}{\mathrm{d}t}\int_\Omega H(u)\,\mathrm{d}x &= \int_\Omega H'(u)u_t\,\mathrm{d}x \\
&= \int_\Omega u\left(\operatorname{div}(A\nabla u) - \operatorname{div}(Bu) + G(u)\right)1_{u<0}\,\mathrm{d}x \\
&= -\int_\Omega \nabla u A \nabla u 1_{u<0}\,\mathrm{d}x + \int_\Omega Bu^2 1_{u<0}\,\mathrm{d}x \\
&\leq 2|B|_{L^\infty(\Omega)}\int_\Omega H(u)\,\mathrm{d}x,
\end{aligned}$$

so $\frac{\mathrm{d}}{\mathrm{d}t}H(u) \leq CH(u)$. Hence Gronwall inequality states that $H(u) \leq e^{Ct}H(0)$. As $H(0) = 0$ due to the non-negative initial data, the assertion follows. □

Chapter 3

Data

The main noninvasive imaging techniques for the brain, as well as for other organs, can be separated into two classes: The computed (or computer) tomography (CT) and the magnetic resonance imaging (MRI).

During a CT, ionizing radiation is used to measure the so-called radiodensity, the absorption coefficient of the radiation used. This may have serious implications on the health; it is estimated that in the United States about 0.4 % of all cancer occurrences are due to computed tomography examinations in the past [BH07]. The main advantage of CT is the finer resolution of the images compared to MRI, the lower cost (of both, devices and actual examination), and the speed.

The magnetic resonance imaging is based on the measurement of spin echoes, which are caused by the relaxation of hydrogen atoms to the equilibrium state in a strong magnetic field. These are abundant in all body tissues, as the human body consist of approximately 70% water. While the magnetic field used in MRI has no direct implication on the health, it must not be used if ferromagnetic implants or other ferromagnetic substances like several tattoo-inks are present in the body. The main disadvantages of MRI are the cost (both of machines and actual examination) and the longer time needed to perform a scan.

So CT scans as well as MRI would give information about the brain structure. Both methods do have advantages for model simulations: The CT method is more flexible, in the sense that in one image bones as well as soft tissue can be resolved in higher detail than it is possible with a classical MRI scan. However, the latter method is based on water diffusion and so it may be better suited for a diffusion model like those presented in the modelling chapter 2. Moreover, in the last years a new technique, the diffusion-MRI was used to measure directional information about the underlying diffusion process simultaneously, hence providing information about directional diffusion. These directions are often referred to as gradients and provide information about the anisotropy in the brain. Depending on the number of

gradients measured, the method is considered as HARDI, which stands for 'high angular resolution diffusion imaging', and of which the Q-Ball imaging technique [Tuc04] is the best known method. Whereas in classical diffusion-MRI only 10-12 gradient directions are taken, a typical Q-Ball imaging would consist of about 50 gradient directions. Of course this gives more angular information, but there is a trade-off between angular and spatial resolution: The time needed during an examination grows with both resolutions and is typically limited. Ideally, mathematical models would profit from refinements of both, but usually only one resolution is refined.

In this work we will concentrate on the use of diffusion-MRI data (this includes diffusion tensor imaging, where a water diffusion tensor is reconstructed, as well as HARDI techniques) in mathematical models, because this type of medical data provides the necessary information about orientations of tissue fibres, which are of tremendous importance to foreshadow the directions in which cells will move. As data set we use the diffusion MRI data coming along with Camino [CBG$^+$06] for all visualizations and simulations. This data set consists of one weighted image and 32 gradient directions, so we have a higher angular resolution. This is not directly used in the following, but diffusion tensors are estimated and we use them for the subsequent tasks.

3.1 Information contained in the data

A typical diffusion-MRI data set will provide a diffusion weighted image together with several gradient ones. For smaller data sets, one can get around 8 or 12 (up to 20) gradients, whereas for HARDI or Q-Ball imaging the number of gradients is substantially higher (around 50). Considering simpler pure anisotropic diffusion, the underlying movement can be described via a diffusion tensor, which clearly has to be symmetric and positive definite. Hence we have to estimate only 6 independent variables per voxel. So we need at least 7 images (one diffusion weighted image to adjust the intensity and 6 gradient images) to estimate such a tensor. Usually, more gradient or even more diffusion weighted images are provided to get a better fit and to reduce the noise (or equivalently enhance the signal-to-noise ratio). There are several different algorithms to estimate a diffusion tensor. The linear [BML94] as well as the non-linear [JB04, AB05] fitting techniques are done locally, whereas the inversion algorithm RESTORE [CJP05] is based not only on local information, but also includes information on the machine like the usual noise level. While the non-linear and the RESTORE fit result in comparable directions of the leading eigenvectors of the diffusion tensor, the linear fit may fail, if the anisotropy is low.

For the visualization of this finding, we define the fractional anisotropy as

$$FA = \sqrt{\frac{3}{2}} \frac{\sqrt{\sum_{i=1}^{3} (\lambda_i - \bar{\lambda})^2}}{\sqrt{\sum_{i=1}^{3} \lambda_i^2}}, \tag{3.1}$$

where $\lambda_1 \geq \lambda_2 \geq \lambda_3$ are the eigenvalues of the estimated water diffusion tensor and $\bar{\lambda}$ is their arithmetic mean. We select a slice containing very few voxels and thereof a section where the difference between the linear and the non-linear fit is obvious (see figure 3.1), especially in regions where the fractional anisotropy is smaller (depicted with darker colours). The discrepancy between both fits shrinks if the fractional anisotropy is larger, corresponding to brighter colours, best seen in figure 3.2. Except for the two figures 3.1 and 3.2 we use the slice 26 of 51 in z-direction of the data set coming along with Camino for visualization, although actual computations are carried out in three dimensions.

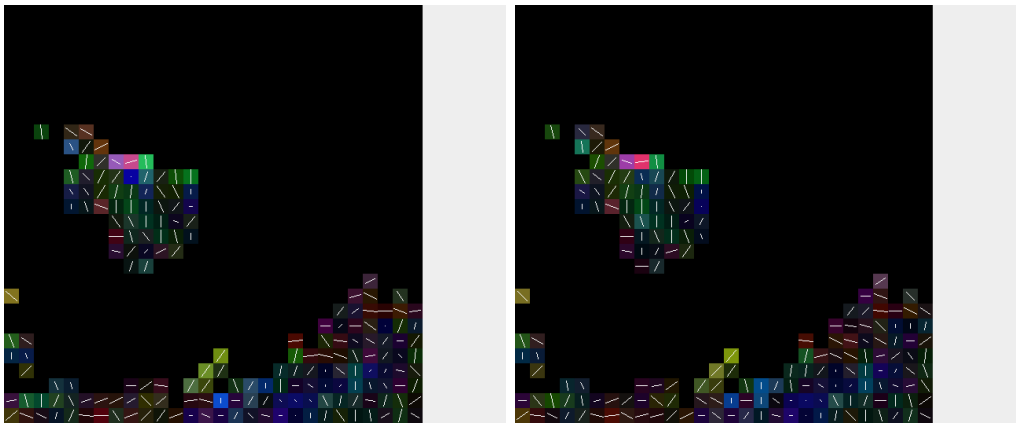

Figure 3.1: The linear versus non-linear fit on the test data. The difference between the fits is best visible in the lower part of the island in the centres of the pictures.

3.1.1 Assessment of q

If we are now interested in the expected orientation of the fibres, we are interested in the quantity [RMU+13, ALJ+11]

$$q(x, \theta) Q(x), \tag{3.2}$$

where $q(x, \theta)$ is the orientation distribution function and by Q we denote the volume fraction of tissue fibres as in the modelling chapter 2. Thereby, θ stands for an orientation, so $\theta \in \mathbb{S}^2$, and x is a position in the mathematical domain describing the brain tissue. The quantity Q

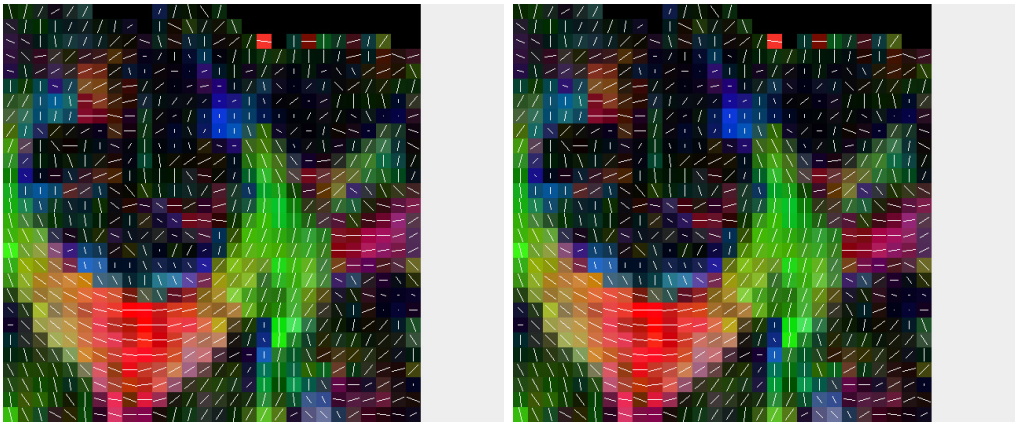

Figure 3.2: The linear versus non-linear fit on a slice containing a fibre bundle. Here the difference is negligible, especially where the white matter tract is located (the bright red and green regions).

was proposed to be proportional to FA in [ALJ+11, EHKS14] and in [EKS16]. This will be discussed in the following, but first we want to enlighten the fibre orientation distribution q.

There are several approaches from different viewpoints. We will concentrate here on an estimated diffusion tensor D originating from medical data. The quantity q was approximated by a fixed distribution for a diffusion tensor, like the peanut distribution used in [PH13, EHKS14, EKS16, EHS15]:

$$q(x,\theta) = \frac{3}{4\pi\ tr(D(x))}\theta^T D(x)\theta.$$

It is easy to verify that this is indeed a probability distribution on $\mathbb{S}^2$. As seen in the structure, the prefactor is only a normalization; it is the easiest way to convert a diffusion tensor to an orientation. The main problem is the very smooth shape of this distribution, that cannot reveal fibre crossings and similar phenomena; this is not only due to the peanut-type of the distribution, but an inherent restriction of diffusion tensor imaging. This is especially problematic when lots of different gradient measurements (Q-Ball imaging) are available. These would be reduced to 6 variables. To enhance the visual anisotropy, a bimodal von-Mises-Fisher distribution was proposed in [PH13] for the quantity q

$$q(x,\theta) = \frac{k(x)}{8\pi\sinh(k(x))}\left(\exp\left(\theta\cdot\phi k(x)\right) + \exp\left(-\theta\cdot\phi k(x)\right)\right),$$

where $k(x) = \kappa FA(x)$. Thereby ϕ is the principal eigenvector of $D(x)$, but in [JKT13] it was argued that the leading eigenvector of a diffusion tensor is not necessarily a good indication of the main fibre orientation in all voxels. This fact may also be underlined with

the orientation difference of the principal eigenvector between two different, especially linear and non-linear reconstruction techniques for the diffusion tensor, rendering the choice of the bimodal von-Mises-Fisher distribution questionable. Moreover (but this is a mathematical modelling issue) the bimodal von-Mises-Fisher distribution, as presented before, introduces the new free parameter κ via the function $k(x)$. This gives the flexibility to increase or decrease the observed anisotropy, but at the cost of estimating a unit-free parameter without indication of the order, such that the 'real' parameter may largely vary in the positive real numbers. So we neglect this approach.

From the medical imaging perspective, there are different concepts of a so-called orientation distribution function [Tuc04, Des08]. These split into the notion of a so-called dODF introduced by Tuch [Tuc04], which is the one that is presented here, and the fODF introduced by Descoteaux [Des08]. It may be an interesting task to explore the difference between these notions in the context of mathematical modelling and its implications on the outcome of numerical experiments. This is not done in the present text, but we look forward to data-based mathematical modelling addressing this question in the future. Here we will give a summary presentation of the ODF in order to focus on the ideas and not going into details for which an extensive background in special spherical functions would be necessary. The details can be found in [Tuc04, Des08, ALS+10]. We will not present the 'original' orientation distribution function, introduced in [Tuc04], since Aganj et al [ALS+10] argued that one has to take into account a normalization of the solid angle during the reconstruction. Thus, the orientation distribution function (in our context) is given by

$$ODF(\theta) = \int_0^\infty P(r\theta) r^2 \, dr,$$

where r^2 is exactly the required normalization [ALS+10]. Thereby, P stands for the displacement probability of a water or hydrogen molecule from position 0 (the origin) to the point $r\theta$ (here in spherical coordinates). Note that the point $r\theta$ is not meant to be in the spatial coordinate system given by the MRI data, but affects only the orientation variable θ, hence the gradients. As mentioned in [ALS+10] this quantity is fully normalized, so in particular unit-free and

$$\int_{\mathbb{S}^2} ODF(\theta) \, d\theta = 1.$$

The main problem is to acquire the orientation distribution function, whence the need to compute the integral. Luckily, in the case of diffusion tensor imaging, which is our focus here, this can be done analytically [ALS+10]:

$$ODF_{DTI}(\theta) = \frac{1}{4\pi |D|^{\frac{1}{2}} \, (\theta^T D^{-1} \theta)^{\frac{3}{2}}}.$$

The symbol $|\cdot|$ denotes the determinant of a rank-2 tensor. Note that unlike the peanut distribution, where the normalization is tied to $tr(D)$, thus only taking the trace values into account, the determinant depends also on the off-diagonal values. The different exponents of $\frac{1}{2}$ and $\frac{3}{2}$ may be counterintuitive, but the determinant actually is a volume form and hence the exponents on the units (of the values) will be the same. Our choice for the tissue fibre orientation q is the above orientation distribution function. As already mentioned, using diffusion tensor imaging results in a reduction of the orientation information to the 6 degrees of freedom of a symmetric tensor. Although from a modelling perspective it is clear that it is better to use more parameters, their number will be reduced anyway, because the macroscopic equations ((2.23) and (2.40)) need the processed information and only use the orientation distribution in an averaged manner through the macroscopic diffusion tensors D and $\tilde{D}$. The evaluation of the effect of including higher order data into the forecast of the tumour shape by numerical simulations is an interesting question. However, we do not answer it here and refer to further work, because the reconstruction of the orientation distribution with more parameters is a non-trivial task and the reconstructed values are currently not available to us.

3.1.2 Assessment of Q

Hence the first quantity, which can be extracted from diffusion-MRI data, is the orientation information, while the other quantity, the occupied volume fraction, is still missing. In [ALJ+11] it was proposed to use the fractional anisotropy as estimator. This aligns with the choice in [EHKS14, EKS16]. The idea behind this is that especially in brain slices with lots of white matter tracts (which are known to have the highest density in the brain tissue) the fractional anisotropy is in correspondence to the expected density distribution in a brain slice. This consideration is clearly valid considering slices containing white matter tracts; however, in regions where the tissue is densely packed, but isotropic, resulting in a very low fractional anisotropy, the estimation of the volume fraction of tissue fibres with the aid of the fractional anisotropy (and other anisotropy measures) must fail. This case may or may not occur in reality, because the white matter tracts are the most dense regions of a human brain and the fractional anisotropy of neuron bundles increases by myelination [LBMP+01]. A core assumption in MRI data acquisition is that the orienting molecules do not pass the membrane of the neurons, a constraint posing the question whether the diffusion-MRI technique is capable to resolve the actual density, or only anisotropy. Computed tomography does not yield a density estimator directly, as in CT scans only absorption coefficients are measured and these are not connected to the density. So there is a need for a further investigation of the estimation of brain matter density out of diffusion-MRI or CT measurements. Reisert et al [RMU+13] introduced a reconstruction technique based on inverse problems. This may be a

working approach, but in general inverse problems (in this case already a non-linear one) and their solutions depend strongly on the used regularization technique. In the paper [RMU$^+$13], the authors used the classical non-linear Tikhonov regularization [Rie03], that might provide an alternative (although not tailored to the actual problem) but then it remains to solve ill-conditioned large systems, which we try to avoid during data processing.

So we set up another possibility to estimate the occupied volume fraction of tissue fibres in [EHS15]. To this aim we consider a cube with side length h, which is a voxel in the MRI data. From Physics we know that the characteristic (diffusion) length is defined as $l_c = \sqrt{\alpha t_c}$ and corresponds to the mean free path length. Its derivation is based on the diffusion equation, which is a further modelling assumption, already implicitly stated, because especially in the context of diffusion tensor imaging, the complete data reconstruction is based on it. In the previous formula, α is a diffusion related coefficient, while t_c is the characteristic (diffusion) time. For the former, there are several sensible choices to form a local average of the diffusion tensor. The first option would be to take the trace of a diffusion tensor, while another one would be to take the mean diffusivity, defined as $MD = \frac{tr(D)}{3}$. When other data sets (like apparent diffusion imaging) are available, one could also use the apparent diffusion coefficient reconstructed directly out of measurements. We opt as in [EHS15] to use the diffusion tensor trace in order to get a normalization with respect to the dimension of the problem.

The characteristic time is more difficult to approximate. Usually the characteristic length and the diffusion are given and the time can be computed, but here we need to invert this situation. As mentioned before, the underlying assumption is that we have to do with a diffusion process, which can be interpreted on the individual particle scale as a Wiener process. We estimate it with the expected first exit time of a particle from a ball surrounding the voxel. The radius of such a ball is given as $h\frac{\sqrt{3}}{2}$. Then the expected exit time is given as $\frac{h^2}{4}$ [KS12a]. This is valid for standard Wiener processes, i.e. for $\mathcal{N}(0, t-s)$ distributed increments, which we have to rescale according to the diffusion strength. For this scaling we select the leading eigenvalue of the diffusion tensor. Then the formula of the characteristic length reads

$$l_c = \frac{h}{2}\sqrt{\frac{tr(D)}{\lambda_1}}.$$

As mentioned before, the characteristic length corresponds to the mean free path length, so the free volume is approximated as l_c^3. Then the volume fraction of tissue fibres is given as

$$Q = 1 - \frac{1}{8}\sqrt{\frac{tr(D)}{\lambda_1}}^3 .$$

3.1.3 Test cases

Now we want to consider some test cases. Let us define the diffusion tensors

$$D_1 = \begin{pmatrix} 1 & 0 & 0 \\ 0 & 1 & 0 \\ 0 & 0 & 1 \end{pmatrix} \quad D_2 = \begin{pmatrix} 2 & 0 & 0 \\ 0 & 0.5 & 0 \\ 0 & 0 & 0.5 \end{pmatrix}.$$

We get the volume fraction estimated by fractional anisotropy versus the method described here for D_1 as 0 versus 0.35 and for D_2 as 0.71 versus 0.77. A volume fraction 0 of tissue fibres in the brain is not possible, so only the second method generates a sensible output for this case. In the second case, the difference between the fractional anisotropy and the new estimator is quite low. This means that the high densities of the white matter tracts (having a high fractional anisotropy) are recovered, but the more isotropic parts are resolved in a better way with the new estimator. This can also be seen in figure 3.3.

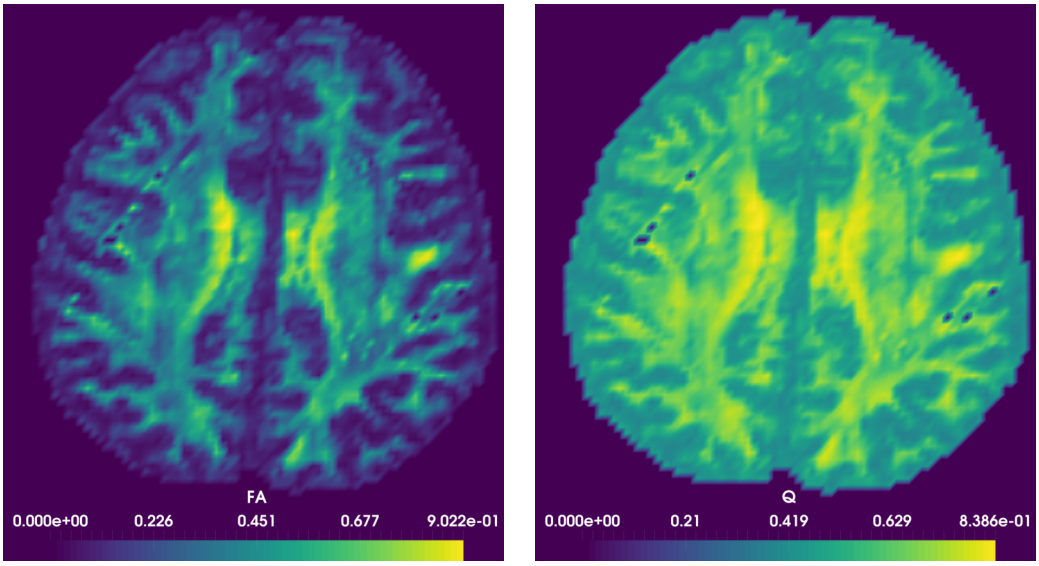

Figure 3.3: The fractional anisotropy versus the estimated volume fraction. The fractional anisotropy does not generate reasonable values (a volume fraction of less than 0.2). The heuristic estimator does generate reasonable values everywhere and captures the high density of the white matter tracts (here bright yellow).

3.2 Appendix: Data preprocessing in detail

Here we describe how a data set can be preprocessed in order to have the diffusion tensors estimated and the data formats converted into some file format which can be easily read.

3.2.1 Data formats used

There are several data formats commonly used in medical imaging:

- DICOM: The absolute standard in medical imaging. It can consist of different image formats and a lot of metadata.
- Nifti: A standard format, that can be used easily in combination with Camino [CBG+06].
- nrrd: A more modern format. The header is in plain text, which helps extracting the information.

In general all mentioned formats may contain 3D or 4D data. The 3D format is either used for a (scalar valued) quantity (e. g. a segmentation all over the brain) or a vector valued quantity (e. g. a diffusion MRI data set over one slice of the brain) unlike the 4D formats, storing a vector valued quantity over the whole brain.

3.2.2 Software

We use **Camino** [CBG+06] for the reconstruction of diffusion tensors, because it is very transparent with respect to which algorithm is actually used. The documentation is very concise and readable, much like a man-page in Unix-like systems. Unfortunately, Camino is only capable to read diffusion MRI data as Nifti 4D images, so one has to ensure that this format is actually used. To convert a series of DICOM images to a 4D Nifti format, one can easily use the **mricron** [mri16] software. For further investigations and conversions between the data formats one has to rely either on the base libraries (mostly written in plain C) or on high level software packages unifying the loading and saving procedures. We have no experience with the base packages by itself, but it may be helpful to list them shortly, each with a web-link

- GDCM: A Dicom loader available under [gdc16].
- Niftilib: A library for reading nifti-1 data available via [nif12].
- NRRD: A library capable of reading nrrd files [NRR16]. It is actually part of the library libteem.

A high-level software package that enables reading and writing all the mentioned data is ITK: Insight Segmentation and Registration Toolkit (available via [ITK16]). All following example codes make heavy use of it. With this library it is very easy to convert one data format into another (see listing 3.2) or to stack up sliced images to a full 3D or 4D image container. The medical data formats do the job quite well, but for mathematical preprocessing

we prefer to rely on data formats that are on the one hand easy to load and on the other hand standardized, hence compatible to other widely used software packages like Matlab. We decided to use NetCDF [Uni15], as it has high quality C++ bindings and implements also the hdf5 standard in its latest NetCDF4 format, while it has good compression facilities, such that the loading of data is reduced to a minimum.

Then a typical processing is done via:

(a) Convert the available data to nifti files using ITK (see listing 3.2)

(b) Estimate the diffusion tensors with Camino

(c) Convert the diffusion tensors to NetCDF using ITK (see listing 3.3).

3.2.3 Known problems

There are two different main problems: the first one occurs when using a Windows PC. Then almost no software from those mentioned above will work natively. The second larger problem is that during the preprocessing step a good brain mask or even a segmentation are required. Often, this segmentation is given on another grid, which cannot be interpreted as sub-grid of the MRI data. This renders the preprocessing difficult, because one has to transfer the data between the grids. In the case of structured quadrilateral or cubic grids this is especially difficult if the grids are not parallel. Then it is better to interpolate the diffusion tensor data (given as floating point numbers) to the grid of the segmentation avoiding this way the interpolation of integer data, which is impossible to do in a reliable manner.

3.2.4 Example codes

Here we want to present some very simple example codes to accomplish conversion tasks on medical data. As mentioned before, we use the software package Camino [CBG+06] for processing, i.e. estimation of diffusion tensors, as it is easy to use and does the preprocessing reasonably well.

The first file is the CMakeLists.txt file needed to setup a working source tree for the conversion:

```
1 # Write cmake version information.
2 # 3.0 should work for everybody
3 cmake_minimum_required(VERSION 3.0)
4
5 # name the project
6 project(Project)
7
8 # If we want to use threads.
9 find_package(Threads)
```

```
10
11 # We need ITK for conversion and preprocessing.
12 find_package(ITK REQUIRED)
13 # We want to read / write files:
14 include(${ITK_USE_FILE})
15
16 # Write some nice message, that we know, which include directory
17 # cmake found.
18 message("Including ${ITK_INCLUDE_DIR}")
19
20 # Include the include directory:
21 include_directories(${ITK_INCLUDE_DIR})
22
23 # Include our own include directory, if needed
24 include_directories(include)
25
26 # Define sources in the directory 'source'
27 file(GLOB PROJECT_SRC
28    "source/converter.cpp")
29
30 # Define the program:
31 add_executable(converter ${PROJECT_SRC})
32
33 # And link to the necessary libraries:
34 target_link_libraries(converter ${ITK_LIBRARIES};${CMAKE_THREAD_LIBS_INIT};
       netcdf_c++4)
35
36 # Set the c++ standard. C++11 should be supported, given, that
37 # ITK is compiled with the '-std=c++11' flag.
38 set_property(TARGET converter PROPERTY CXX_STANDARD 11)
```

Listing 3.1: Raw CMakeLists.txt file for the use of ITK

The next example deals with the conversion of a three dimensional medical data file to another format:

```
1  /*
2    Example code for the Dissertation of Alexander Hunt,
3    Biomathematics Group, University of Kaiserslautern
4  */
5
6  // C++ includes:
7  #include <iostream>
8  #include <string>
9
10 // ITK Includes, CMake will recover the absolute paths:
11 #include <itkImage.h>
12 #include <itkImageFileReader.h>
13 #include <itkImageFileWriter.h>
14
15 // Print usage information:
16 void usage()
17 {
18   std::cout << "Usage: converter [3D file] [output file]" << std::endl;
```

```
19 }
20
21 int main(int argc, char ** argv)
22 {
23   // Check the number of input arguments:
24   if( ! (argc == 3))
25     {
26       // Print usage information
27       usage();
28       // Exit, but no error:
29       return 0;
30     }
31
32   // typedefs:
33   // The PixelType describes, what we expect as pixel:
34   // Here we use int, so this will work for a segmentation file
35   typedef int PixelType;
36   // We have a 3D image, with pixel int:
37   typedef itk::Image<PixelType,3> ImageType;
38
39   // We want to read and write this type of image:
40   typedef itk::ImageFileReader<ImageType> ReaderType;
41   typedef itk::ImageFileWriter<ImageType> WriterType;
42
43   // Get the in/outfile names:
44   const std::string infileName = argv[1];
45   const std::string outfileName = argv[2];
46   // NOTE: This is NOT the secure way.
47   // I would recommend boost::program_options to do the job in
48   // a more secure manner.
49
50   // Make a reader:
51   ReaderType::Pointer reader = ReaderType::New();
52   // set filename:
53   reader->SetFileName(infileName);
54
55   // Make the corresponding writer:
56   WriterType::Pointer writer = WriterType::New();
57   // Set filename. Formats will be guessed out of the filename extension.
58   writer->SetFileName(outfileName);
59   // Set the writer input:
60   writer->SetInput(reader->GetOutput());
61   // At this time nothin happened and there is only a connection between
62   // the reader and writer, so we need to update the writer.
63   // Then the file is read and written in the corresponding format.
64
65   // NOTE: The Update() method may throw exceptions, which we need to
66   // catch:
67   try
68     {
69       // Do the job.
70       writer->Update();
71
72       // And return without error:
```

```
73        return 0;
74      }
75    catch(std::exception & e)
76      {
77        // I catch every known exception with this, so this includes
78        // out of memory and or file exceptions.
79        // Write information about the problem:
80        std::cerr << "Exception " << e.what() << std::endl;
81        // And return with error:
82        return 1;
83      }
84    catch(...)
85      {
86        // Catch the rest. These are unknown exceptions.
87        // In most cases, this will not happen, personally,
88        // I did not have any unkonw exception from
89        // the standary c++ library neither from the
90        // ITK library.
91        std::cerr << "Unknown exception thrown" << std::endl;
92        // Exit with error
93        return 1;
94      }
95  } // end main.
```

Listing 3.2: Convert between data formats

In the last example, we want to present the conversion of a segmentation and a diffusion tensor file to a single netCDF file. In this code, the file is in the actual NetCDF4-format, meaning that every software capable to read HDF5 files should be able to read it.

```
1  /*
2    Example code for the Dissertation of Alexander Hunt,
3    Biomathematics Group, University of Kaiserslautern
4  */
5
6  // C++ includes:
7  #include <iostream>
8  #include <string>
9
10 // NetCDF include. We rely on the C++ Binding:
11 #include <netcdf>
12
13 // ITK includes, CMake will recover the absolute paths:
14 #include <itkImageFileReader.h>
15 #include <itkImage.h>
16 // We want to read estimated diffusion tensors:
17 #include <itkDiffusionTensor3D.h>
18
19 // use the netcdf namespaces:
20 using namespace netCDF;
21
22 // Wrapped in an anonymous namespace:
23 namespace
```

```
24 {
25   // Helper function to compute indices
26   // For one dimension:
27   unsigned int indexComputer(const unsigned int i,
28                              const unsigned int n)
29   {
30     return i;
31   }
32   // For more dimensions, we need to stack this up.
33   // The easy way is to use the variadic templates of C++11:
34   template <typename ... ARGS>
35   unsigned int indexComputer(const unsigned int i,
36                              const unsigned int n,
37                              ARGS ... args)
38   {
39     return i + n * indexComputer(args...);
40   }
41
42   // Helper function for the output of diffusion tensors:
43   template <typename S,
44             typename D>
45   void writeToNCDF(S s, D d, const std::string & filename)
46   {
47     // s: Segmentation
48     // d: Diffusion tensor
49     // filename: Name for the output file
50
51     // First we have to check the spacings / sizes and so on:
52     auto d_spacings = d->GetSpacing();
53     auto s_spacings = s->GetSpacing();
54     auto d_sizes = d->GetLargestPossibleRegion().GetSize();
55     auto s_sizes = s->GetLargestPossibleRegion().GetSize();
56
57     const bool spacings_ok =
58       ((d_spacings[0] - s_spacings[0])<1e-4 &&
59        (d_spacings[1] - s_spacings[1])<1e-4 &&
60        (d_spacings[2] - s_spacings[2])<1e-4);
61     const bool sizes_ok = ((d_sizes[0] == s_sizes[0]) &&
62                            (d_sizes[1] == s_sizes[1]) &&
63                            (d_sizes[2] == s_sizes[2]));
64     // Check spacings:
65     if(!spacings_ok)
66       {
67         // Write information:
68         std::cout<<"Spacings are different: "
69                  <<d_spacings << " vs " << s_spacings<<std::endl;
70         // And throw an exception in the case that not:
71         throw std::runtime_error("Spacings are different");
72       }
73     // Check sizes:
74     if(!sizes_ok)
75       {
76         // Write information:
77         std::cout << "Sizes are different: "
```

```
78                  <<d_sizes << " vs "<<s_sizes << std::endl;
79          // And throw an exception in the case of inequality
80          throw std::runtime_error("Sizes are different");
81        }
82
83      // Now we have checked all pitfalls with respect to the data.
84      // Now we write:
85      std::cout << "Going to write "<<filename<<std::endl;
86
87      // Create NCDF file:
88      NcFile file(filename,NcFile::replace,NcFile::nc4);
89      // NcFile::replace replaces the file in case it exists, otherwise
90      // creates it.
91      // NcFile::nc4 is the new NetCDF4 standard, which is simple hdf5
92      // in disguise
93      // Add dimensions:
94      NcDim x = file.addDim("x",d_sizes[0]);
95      NcDim y = file.addDim("y",d_sizes[1]);
96      NcDim z = file.addDim("z",d_sizes[2]);
97      NcDim dim = file.addDim("d",3);
98
99      // Spacings var:
100     NcVar spacings = file.addVar("spacing",ncDouble,dim);
101     std::vector<double> data({d_spacings[0],d_spacings[1],d_spacings[2]});
102     spacings.setCompression(false,true,9);
103     spacings.putVar(data.data());
104
105     // Segmentation var:
106     NcVar segmentation = file.addVar("B",ncInt,{x,y,z});
107     std::vector<int> s_data(s_sizes[0] * s_sizes[1] * s_sizes[2]);
108     for(unsigned int i=0;i<s_sizes[0];++i)
109       for(unsigned int j=0;j<s_sizes[1];++j)
110         for(unsigned int k=0;k<s_sizes[2];++k)
111           s_data.at(indexComputer(k,s_sizes[2],
112                                   j,s_sizes[1],
113                                   i,s_sizes[0]))= s->GetPixel({i,j,k});
114     segmentation.setCompression(false,true,9);
115     segmentation.putVar(s_data.data());
116
117     // Diffusion tensor:
118     data.clear();
119     data.resize(d_sizes[0] * d_sizes[1] * d_sizes[2] * 3 * 3);
120     for(unsigned int i=0;i<d_sizes[0];++i)
121       for(unsigned int j=0;j<d_sizes[1];++j)
122         for(unsigned int k=0;k<d_sizes[2];++k)
123           {
124             auto pix = d->GetPixel({i,j,k});
125             for(unsigned int ii=0;ii<3;++ii)
126               for(unsigned int jj=0;jj<3;++jj)
127                 {
128                   const unsigned int ind =
129                     indexComputer(ii,3,jj,3,k,d_sizes[2],
130                                   j,d_sizes[1],
131                                   i,d_sizes[0]);
```

```
132                     data.at(ind) = pix(ii,jj);
133                   }
134               }
135       NcVar diffusion_tensor = file.addVar("DW",ncDouble,{x,y,z,dim,dim});
136       diffusion_tensor.setCompression(false,true,9);
137       diffusion_tensor.putVar(data.data());
138     }
139 } // end namespace{}
140
141 // Main:
142 int main(int argc, char ** argv)
143 {
144   // Define Pixel types:
145   typedef int PixelType;
146   typedef itk::DiffusionTensor3D<double> TensorType;
147   typedef itk::Image<PixelType,3> SegmentationImage;
148   typedef itk::Image<TensorType,3> DTIImage;
149
150   typedef itk::ImageFileReader<SegmentationImage> SegReader;
151   typedef itk::ImageFileReader<DTIImage> DTIReader;
152
153   try
154     {
155       // The use is
156       // program [segmentation file] [diffusion tensor file] [output]
157       std::string seg_filename = argv[1];
158       std::string dti_filename = argv[2];
159       std::string outfile = argv[3];
160       SegReader::Pointer seg = SegReader::New();
161       seg->SetFileName(seg_filename);
162       seg->Update();
163       SegmentationImage::Pointer segmentation = seg->GetOutput();
164
165       DTIReader::Pointer dti = DTIReader::New();
166       dti->SetFileName(dti_filename);
167       dti->Update();
168       DTIImage::Pointer diffusion_tensors = dti->GetOutput();
169
170       writeToNCDF(segmentation,diffusion_tensors,outfile);
171
172     }
173   catch(std::exception & e)
174     {
175       std::cerr << "Exception "<<e.what()<<std::endl;
176       return 1;
177     }
178   catch(...)
179     {
180       std::cerr << "Unknown exception thrown"<<std::endl;
181       return 1;
182     }
183
184 }
```

Listing 3.3: Convert medical data to NetCDF file

Chapter 4

Numerical simulation

4.1 Introduction

In this chapter we will present how the previously introduced models are solved numerically. We will neither show how the microscopic models (cellular scale including the subcellular dynamics) can be solved (if one is interested, we would recommend [SS11]), neither how the mesoscopic models can be discretized. This is due to the lack of reasonable initial conditions for these - of course one may choose something arbitrary for the velocity variable, but the aim of personalized medicine requires reliable information, that is only available on the macroscopic (i. e. spatio-temporal) scale. The main traits of a numerical method are clearly correctness and ease of implementation. For the accuracy, we will rely as often as possible on existing and, more important, on well-tested codes. Our choice are the core packages of the numerical framework of Dune [BBD$^+$08b, BBD$^+$08a, BB07, BB08] for grid handling and sparse linear algebra, whereas the necessary dense linear algebra is handled by Armadillo [SC16], which combines fast execution with ease of implementation. All of these libraries are written in and for C++, a compiled general-purpose programming language. We cannot use Matlab nor the open source equivalents Gnu Octave and Scilab, because we need to load plenty of data, which is required for the personalization of the mathematical model. This data has to reside in memory, so we need a memory efficient language, like C++. For the loading procedure itself, it is convenient to have access to high quality libraries, that are usually available for the C-language family (C/C++). Another reason to use a compiled language is the execution speed. There is no point in having a good model, which could be used in clinical practice to estimate the tumour growth, but does not fulfil the strict requirements on performance, originating from the pressing need of therapy in presence of glioblastoma. It is necessary that three dimensional computations are possible in a reasonable time, as two dimensional ones neglect the third dimension the tumour can use to spread, and thus can

lead to wrong results (see e.g. figure 4.3).

The simulations must preserve every core property the equation exhibits, and should handle the problem efficiently. A high-performance code is not a necessity, but we must not waste time nor memory. The region where the computation takes place is given by the medical data, which is 167549 voxels in three dimensions in the case of the data set coming along with Camino [CBG+06]. The estimation of the necessary quantities D and Q of the modelling chapter 2 takes a few minutes (in our non-representative test 94 seconds) and the estimation of the quantities $\tilde{D}$ and U substantially longer (around 18 hours). In the case of model (2.23) there is only the need to compute the diffusion tensor D and the volume fraction Q, whereas model (2.40) requires computing double integrals for $\tilde{D}$ and U. But luckily, the computations are only local, so they can be massively parallelized using additional power to fit the time requirements.

4.2 Discretization of the macroscopic equations

We only consider the prototype of the macroscopic equations belonging to models (2.23) and (2.40), so we handle the reaction-convection-diffusion equation

$$\partial_t u - \operatorname{div}(D(x)\nabla u) + \operatorname{div}(M(x)u) = f(u), \tag{4.1}$$

where D is a positive definite, spatial dependent diffusion tensor and M is a spatial dependent drift vector, both assumed to be continuous. For the models (2.23) and (2.40) where we have to do with myopic and myopic-like diffusion, the additional drift term is included in M. The function f is a nonlinear reaction term. In our case it has the property $f(0) = 0$, so the parabolic comparison principle states that the solution stays non-negative, as proven in the modelling chapter 2. If we only consider the convection-diffusion term

$$-\operatorname{div}(D\nabla u - Mu)$$

and integrate it over a test volume Σ with at least Lipschitz boundary, we get by the Gauß theorem

$$\int_\Sigma -\operatorname{div}(D\nabla u - Mu)\,dx = \int_{\partial\Sigma} -n \cdot (D\nabla u - Mu)\,d\sigma(x),$$

where n represents the unit outer normal to $\partial\Sigma$. So this part of the equation is locally mass conservative. This also remains true if we look at the convection term or the diffusion term alone.

These properties, namely local mass conservation of the diffusive and convective fluxes, as well as the non-negativity must be conserved by the numerical method used. This hinders

us from using finite elements, as there is no standard method fulfilling both properties. Especially the non-negativity is of importance, because we solve the equations for a cell density, that has to remain non-negative for all times. We cannot assign any meaning to negative values, except that the numerical method is not tailored to the problem and should not be used. In the following, we will present the discretization of the equation (4.1) part by part, starting with the diffusion term.

4.2.1 Discretization of the diffusion term

Let us consider the equation

$$\begin{aligned} -\operatorname{div}(D\nabla u) &= g \quad \text{in } \Omega \\ u &= 0 \quad \text{on } \partial\Omega, \end{aligned} \tag{4.2}$$

in a Lipschitz-domain Ω with polygonal boundary. As we do not want to inflate the presentation with the inclusion of different boundary conditions, we select homogeneous Dirichlet conditions, although we solve equations (2.23) and (2.40) to homogeneous Neumann boundary conditions. Homogeneous Neumann conditions can be included via removing the fluxes over the boundary faces.

It is known [EGH00] that for full tensorial diffusion we are confronted with the classical two point fluxes not being sufficient if the eigenvectors of D are not aligned with the grid, which is not satisfied for real medical data (see figure 3.2). So, since two point fluxes are not sufficient, multipoint flux methods (MPFA) were proposed [Aav02], of which the MPFA O-method is the most prominent one [Aav02]. We do not want to present this special method, but implemented it and realized (which is actually known to the literature [Dro14]) that in general it does not preserve non-negativity of the solution and hence it is not usable for our purposes.

A very attractive method from the analytical point of view (due to its high order) is the discontinuous Galerkin approximation (DG) [ESZ09], or even the hybridized one (HDG) [NPC09], in which a postprocessing strategy can be used to gain one order of convergence [NPC09, NP12]. The strengths of the HDG method are local approximation of the fluxes, high approximation orders, and a parallelization friendly layout of the resulting linear systems, which can be locally inverted due to a cell-wise block structure. However, this method fails in preserving the positivity in general without flux limiters. So neither the MPFA nor the (H)DG methods, yet attractive, can be used to solve the equation (4.1).

A viable solution for the discretization of (4.1) is to use mimetic finite differences [LMS14, dVDM11], although they are not optimal, because they have severe computational implications like inverting large unsymmetric linear systems. They are based on approximations of inner products in a way that ensures the integral theorems - especially the Gauß

theorem in the present context - to remain valid in a discrete form. This can be established with a correct approximation of the discrete differential operators. The following short sketch is based on the very comprehensive and readable work [LMS14] to which in order to improve readability we refer for all results without citing them explicitly in the following. The paper [LMS14] is a review of the numerical analysis on mimetic discretizations performed during the last decades.

As a first step for the mimetic discretization of the diffusion equation (4.2) we transform the equation

$$\begin{aligned} -\operatorname{div}(D\nabla p) &= g \quad \text{in } \Omega \\ p &= 0 \quad \text{on } \partial\Omega \end{aligned}$$

into the equivalent first order system

$$\begin{aligned} u &= -D\nabla p \quad \text{in } \Omega \\ \operatorname{div}(u) &= g \quad \text{in } \Omega \\ p &= 0 \quad \text{on } \partial\Omega. \end{aligned} \tag{4.3}$$

We renamed the previous variable u into p to be conformal with the mimetic finite difference literature, where the variable represents in most cases a pressure.

Now we select a finite volume approximation of the system (4.3). So let $\mathcal{T}_h$ be a triangulation of Ω to mesh width h. Denote by $C(\mathcal{T}_h)$ the cells and by $F(\mathcal{T}_h)$ the faces of the triangulation. In our case of a voxel grid given by medical data, the cells will be squares (in two dimensions) or cubes with side length h. We do not want to present the mimetic finite differences for an arbitrary grid, but for the sake of simplicity prefer to do it only for such a structured quadrilateral grid.

Define the space

$$C_h = \{p : C(\mathcal{T}_h) \to \mathbb{R} \colon p\Big|_c \equiv const \text{ for each cell } c \in \mathcal{T}_h\}.$$

The variable p is now approximated by $p_h \in C_h$ such that p_h holds the cell averages of p, hence

$$p_h\Big|_c = \frac{1}{|c|} \int_c p(x)dx$$

for each computational cell c. For the fluxes we need to define the space

$$F_h = \{u : F(\mathcal{T}_h) \to \mathbb{R} \colon u\Big|_f \equiv const \text{ for each face } f \text{ of } \mathcal{T}_h\}.$$

Note that the space F_h cannot hold the vector valued function u in the system (4.3), but only the normal fluxes. So we approximate the function u by a (scalar valued) function $u_h \in F_h$

such that

$$u_h\Big|_f = \frac{1}{|f|}\int_f n_f \cdot u(x) d\sigma(x)$$

for all faces f with the notation n_f for the normal vector on the face f.

Note 4.2.1.

- *The notations $|c|$ and $|f|$ stand for the volume of the cell c and the face f, respectively.*
- *The normal vector n_f is directed in an (arbitrary) fixed orientation, whereas the normal on the face f directed outwards of a cell c is denoted by $n_{c,f}$.*
- *An issue with the implementation is to keep track of the face orientations. A possible solution is to save them into an array of Boolean variables, but the simpler version, which is the one we use, is to exploit the cell indices that are given by the implementation of the grid in Dune. So we selected a face normal orientation to be positive if it points from a lower indexed cell to a higher indexed one.*

The main idea behind mimetic finite differences is the compatible discretization of differential operators, so we select to do this for the divergence operator first. As seen from the system (4.3), it has to map our approximated u to a cell variable, hence $DIV : F_h \to C_h$. A compatible discretization is

$$(DIV\ u_h)_c = \frac{1}{|c|}\sum_{f\in\partial c} \alpha_{c,f}\ |f|\ u_f,$$

where α describes the mutual orientations of the face normal (with fixed orientation) n_f and the face normal on the cell $n_{c,f}$, so $\alpha_{c,f} = n_f \cdot n_{c,f}$.

Lemma 4.2.1. *For the previously defined discrete divergence, the discrete analogue of the Gauß theorem holds*

$$\sum_{c\in V_h} |c|\,(DIV\ u_h)_c = \sum_{f\in S_h} |f| u_f,$$

where V_h is a connected union of computational cells with S_h as boundary and the normal vectors n_f are assumed to point outward of V_h.

Proof. Obvious, for the inner faces the orientations $\alpha_{c,f}$ are counted with different signs. □

Another nice property needed is that the discrete divergence DIV is surjective, so $DIV(F_h) = C_h$. For a proof we refer to lemma 2.1 in [LMS14]. Now we are able to discretize the second equation of the system (4.3):

$$\operatorname{div}(u) = g$$

will be transformed into the discrete counterpart

$$DIV\ u_h = g_h,$$

where

$$(g_h)_c = \frac{1}{|c|} \int_c g(x)dx.$$

Now the equation

$$u + D\nabla p = 0$$

remains to be discretized. This has to be done in a compatible way. Intuitively, one may be tempted to use similar defining properties from vector calculus for the discrete gradient, but this does not succeed. The way to go is better understandable if we test the equation with some smooth function ϕ:

$$\left\langle D^{-1}u, \phi \right\rangle_{L^2(\Omega)} + \langle \nabla p, \phi \rangle_{L^2(\Omega)} = 0.$$

Inserting the well known identity $\nabla = -\operatorname{div}^\star$, we get

$$\left\langle D^{-1}u, \phi \right\rangle_{L^2(\Omega)} - \langle \operatorname{div}^\star p, \phi \rangle_{L^2(\Omega)} = 0.$$

Thereby $\operatorname{div}^\star$ denotes the L^2-adjoint operator of div. For a moment let us assume that we have compatible mimetic scalar products $[\cdot,\cdot]_{F_h}$ and $[\cdot,\cdot]_{C_h}$. Then we would like to have as in the continuous case a discrete gradient operator $GRAD$ fulfilling $GRAD = -DIV^\star$ with respect to the scalar products, so

$$[DIV\ u_h, p_h]_{C_h} = -\left[u_h, GRAD\ p_h\right]_{F_h}.$$

We require that the scalar products fit to the equation, and so their cell contributions have to fulfil

$$\begin{aligned} [p_h, q_h]_{C_h}\Big|_c &\approx \int_c q(x)p(x)dx \\ [u_h, v_h]_{F_h}\Big|_c &\approx \int_c u(x) \cdot D^{-1} \cdot v(x)dx \end{aligned} \tag{4.4}$$

for each computational cell c.

Note 4.2.2. - *The operator $GRAD$ introduced above is the so-called derived gradient operator in [LMS14] and is denoted therein by $\widetilde{GRAD}$.*

- *The cell-wise contributions of the scalar products may be written as matrix multiplication, so each of the scalar products $[\cdot,\cdot]_\Sigma$ is represented by a cell-wise matrix M_Σ for $\Sigma \in \{C_h, F_h\}$. In the following, we will drop the 'h' as second index, because we only refer to a fixed width h.*

The task is now to deduce conditions on M_C and M_F in order to get an accurate numerical scheme. In order to fulfil the first equation of (4.4), we may select $M_C\Big|_c = |c|$. This fits also the dimensions of the space C_h, where we have only one degree of freedom per cell leading to a globally diagonal matrix M_C, which hence may be inverted easily. The face matrix M_F (also cell-wise) is not that easy and we need to impose consistency conditions in order to arrive at a first order scheme. Let us denote by m the number of faces per cell, which is in the case of a structured quadrilateral grid fixed. In two dimensions, we have $m = 4$, in three $m = 6$. Then we arrive at a set of algebraic equations

$$M_F\Big|_c N_i = R_i \quad i = 1, ..., m$$

to be fulfilled for a first order numerical method. It can also be written as a matrix equation

$$M_F\Big|_c N_c = R_c, \tag{4.5}$$

where the matrices N_c and R_c containing the columns N_i and R_i, respectively, are left to be defined. They represent the applications of the inner product to an ansatz space. Let us define the cell centre x_c and the face centre x_f. Both are well defined in the case of an axiparallel structured quadrilateral grid, like that on which the medical data is given. Then the matrices N_c and R_c are given by

$$N_c = \begin{pmatrix} n_{f_1}^T \\ \vdots \\ n_{f_m}^T \end{pmatrix} D \qquad\qquad R_c = \begin{pmatrix} \alpha_{c,f_1}|f_1|(x_{f_1} - x_c)^T \\ \vdots \\ \alpha_{c,f_m}|f_m|(x_{f_m} - x_c)^T \end{pmatrix}.$$

Under the assumption that $R_c^T N_c$ is symmetric and positive definite (which is proven to be fulfilled) we can solve the equation (4.5) with

$$\begin{aligned} M_F\Big|_c &= M_0 + M_1, \text{ where} \\ M_0 &= R_c \left(R_c^T N_c\right)^{-1} R_c^T \text{ and} \\ M_1 &= D_c U_c D_c^T \end{aligned}$$

upon using a matrix D_c with columns forming a basis of $ker(N_c^T)$. The matrix $U_c \in \mathbb{R}^{d\times d}$ has to be symmetric and positive definite and controls the numerical scheme. As mentioned in [Dro14], the matrix U_c has little influence on the convergence behaviour and the approximation error, but it can be used to arrive at a monotone scheme. For the presentation of the monotone method, the matrix equation (4.5) can be reformulated as

$$N_c = W_F|_c R_c. \tag{4.6}$$

If we split the matrix $W_F\Big|_c$ as before for $M_F\Big|_c$ we get

$$\begin{aligned} W_F\Big|_c &= W_0 + W_1, \\ W_0 &= N_c \left(N_c^T R_c\right)^{-1} N_c^T \text{ and} \\ W_1 &= \tilde{D}_c \tilde{U}_c \tilde{D}_c^T. \end{aligned}$$

The columns of the matrix $\tilde{D}_c$ have to form a basis of $ker(R_c^T)$, the matrix $\tilde{U}_c$ has to be symmetric and positive definite as before.

Lemma 4.2.2 (Lemma 3.1 in [LMS14]). *For the previously defined matrices the identity*

$$R_c^T N_c = D|c|$$

is valid, so we may use the formulae for M_0 and W_0 presented before.

Example 4.2.1 (Corollary 2.1 in [LMS14]). *A simple possibility to get convergence is now to take the matrix $M_F|_c$ as*

$$M_F\Big|_c = R_c \left(R_c^T N_c\right) R_c^T + \lambda_c \left(I - N_c \left(N_c^T N_c\right) N_c^T\right),$$

with a stabilization constant, that may be chosen as

$$\lambda_c = \frac{1}{2} tr \left(R_c \left(R_c^T N_c\right)^{-1} R_c^T\right).$$

For the mimetic finite difference method we have the desired convergence properties.

Theorem 4.2.1 (Theorem 3.3 and 3.4 in [LMS14]).

Let $u \in H(\mathrm{div}, \Omega) = \left\{\phi \in (L^2(\Omega))^d, \mathrm{div}(\phi) \in L^2(\Omega)\right\}$ and $p \in H^2(\Omega)$ be a solution to the first order system (4.3). Let the following assumptions (in the paper [LMS14] denoted by (S1) and (S2)) be fulfilled:

- *Let v^1 and v^2 be vector valued functions on a cell c such that v^1 is a constant vector and $div(v^2)$ is constant in c. Moreover let the normal flux $v^2 \cdot f$ be constant on each*

face f of cell c. For the constant diffusion tensor D and discretizations v_h^1 and v_h^2, the mimetic inner product $[\cdot,\cdot]_F|_c$ has to be exact, so

$$[v_h^2, v_h^1]_F|_c = \int_c v^2 D^{-1} v^1 dx.$$

This assumption is at the origin of the consistency conditions (4.5) *and* (4.6) *and hence is fulfilled for the presented matrices.*

- *The matrix $M_F\Big|_c$ has to be coercive and bounded, in the sense that there are positive constants α_1 and α_2 fulfilling*

$$\alpha_1 \ |c| \ |x|^2 \leq x^T M_F|_c x \leq \alpha_2 \ |c| \ |x|^2 \quad \text{for all } x \in \mathbb{R}^m.$$

Let $u^I \in F_h$ and $p^I \in C_h$ be the projected variants of u and p. Let $u_h \in F_h$ and $p_h \in C_h$ be the solution of the discretized system using the mimetic finite difference method. Then it holds

$$\left|u^I - u_h\right|_{F_h} + \left|p^I - p_h\right|_{C_h} \leq Ch||p||_{H^2},$$

where the discrete norms $|\cdot|_\Sigma$ are defined via the scalar products $|\phi|_\Sigma = ([\phi,\phi]_\Sigma)^{\frac{1}{2}}$. Moreover, if the domain is convex and the right hand side g is at least $H^1(\Omega)$, it holds

$$\left|p^I - p_h\right|_{C_h} \leq Ch^2 \left(||p||_{H^2} + ||g||_{H^1}\right).$$

In both cases, the constant C is independent of the mesh size h.

The convergence is optimal for a piecewise constant approximation. Of course, one can introduce additional degrees of freedom for u or p leading to additional constraints in order to get a higher order mimetic finite difference method. This is sketched in chapter 5.2 of [LMS14], but we restrain here at using a first order method. The complete discretized system reads

$$\begin{aligned} -DIV^T \ M_C \ p_h + M_F \ u_h &= 0 \\ DIV \ u_h &= g_h. \end{aligned} \tag{4.7}$$

The matrix M_C is, as noted, diagonal, and represents the application of the scalar product $[\cdot,\cdot]_{C_h}$, whereas the matrix M_F represents $[\cdot,\cdot]_{F_h}$ and has to be assembled cell-wise. The implementation of this method is quite straightforward, with the exception of the matrix M_F. If we want to use a monotone method, we have to assemble the matrix $W_F|_c$ first and explicitly invert it. This is time consuming, but as the size is given by m, which is bounded by 6 (for three dimensions) in our case, this is a viable solution. Otherwise, one would

compute a matrix W_F instead of M_F and then perform a sparse matrix-matrix multiplication. We tested both possible implementations and realized that explicitly inverting small dense matrices is much faster than the sparse matrix-matrix product. For the monotone mimetic finite difference method, one may select a compatible stabilization matrix $\tilde{U}_c$. In chapter 4.1 in [LMS14] this was done for a hybrid mimetic finite difference method, which is not what we want to use; however, the idea can be transferred to the sketched one. Using $\tilde{U}_c = \hat{D}$, where the entries of $\hat{D}$ are given by

$$\left(\hat{D}\right)_{i,j} = -|D_{i,j}| \quad \text{for } i \neq j$$
$$\left(\hat{D}\right)_{i,i} = D_{i,i},$$

leads to a monotone method.

Remark 4.2.1. *The previous formula is only valid for a structured axiparallel quadrilateral grid, like YaspGrid of Dune and the grids of the given medical data.*

To test the implementation of this method, we used $\Omega = (0,1)^2$ and the constant diffusion tensor

$$D = H \begin{pmatrix} 1.1 & 0 \\ 0 & 0.01 \end{pmatrix} H^{-1}$$

with a rotation matrix

$$H = \begin{pmatrix} \cos\left(\frac{\pi}{4}\right) & \sin\left(\frac{\pi}{4}\right) \\ -\sin\left(\frac{\pi}{4}\right) & \cos\left(\frac{\pi}{4}\right) \end{pmatrix}.$$

So we test two different properties: first the eigenvectors are not aligned with the grid (as they are given by the columns of the rotation matrix H) and secondly the eigenvalues of the diffusion tensor have two orders of magnitude in difference, a property ubiquitous in real data, but problematic for numerical schemes. As a test function we chose

$$p(x) = \sum_{i=1}^{3} \exp\left(\frac{(x - x_i)^2}{0.01}\right)$$

using the points $x_1 = (0.25, 0.25)^T$, $x_2 = (0.75, 0.25)^T$ and $x_3 = (0.5, 0.75)^T$. The right hand side g as well as the boundary values were chosen such that the test function p fulfils the equation. The results can be seen in the tables 4.1 and 4.2 for the non-monotone and the monotone method, respectively. In the tables the cycle indicates the refinement cycle applied on the grid. We used global refinement, so the size h will be halved in one cycle. The row L^2-residual indicates the discrete norm $|\cdot|_{C_h}$ and the H^1-seminorm is given by the L^2-norm on the faces (and so on the variable u). The row convergence contains the

Cycle	0	1	2	3	4
L^2-residual	1.40906	0.370784	0.0963164	0.0246138	0.00642245
H^1-seminorm	1.37968	0.719982	0.33475	0.138349	0.0623659
Convergence	∞	0.26314	0.25976	0.25555	0.26093

Table 4.1: Convergence results for the non-monotone method

Cycle	0	1	2	3	4
L^2-residual	2.00824	0.501928	0.125469	0.0313857	0.00793592
H^1-seminorm	0.978507	0.32016	0.113042	0.0477333	0.0404773
Convergence	∞	0.24993	0.24999	0.25015	0.25285

Table 4.2: Convergence results for the monotone method

change of the L^2-residual during one step, i. e. e_i/e_{i-1}, where e_i is the L^2-error in cycle i. As one can easily see, the convergence on the p-variable is around 0.25, as expected. The error on the u-variable is not as expected, because we are using another norm to measure the distance; however, a linear convergence can be indicated. So the implementation is correct and exhibits the expected order of convergence.

4.2.2 Discretization of the convection term

Here the task is to discretize the equation

$$\begin{aligned} \operatorname{div}(Mu) &= g \quad \text{in } \Omega, \\ M \cdot nu &= 0 \quad \text{on } \partial\Omega, \end{aligned} \tag{4.8}$$

where M is a continuous function depending on the spatial variable x. We need to approximate the function u in a manner that has to be compatible to the discretization of the diffusion term. For the latter we used mimetic finite differences, leading to cell centred finite volume approximations for the main variable, so we use for this term cell centred finite volumes tailored to the triangulation $\mathcal{T}_h$ of width h. Then the discretized form of (4.8) reads for a cell c

$$\operatorname{div}(Mu)\Big|_c \approx \frac{1}{|c|} \sum_{f \in \partial c \setminus \partial\Omega} M_f u_{f,+},$$

where M_f is an approximation of

$$M_f \approx \int_f M(x) \cdot n d\sigma(x)$$

and $u_{f,+}$ is the classical upwind evaluation of u on the face f [dVDM11, Dro10]. This scheme is locally mass conservative and moreover conserves positivity, at least numerically. Details can be found in [EGH00]. This discretization is first order exact and compatible with the mimetic finite difference scheme for the diffusion term [dVDM11, Dro10]. Another possibility also discussed in [dVDM11, Dro10] is to use mimetic formulations of this term leading to a method where local mass conservation has to be enforced via additional constraints in the linear systems to solve. However, the enforced local mass conservation does not hold in the classical sense, where each of the diffusive and convective fluxes are conserved, but only the combination of both.

The only question remaining is how to choose the value of M on a face, especially if this value depends on real data given typically only in the interior of the cells and not on the faces. An intuitive way would be to use linear interpolation between the cell values, but sometimes it is better to use harmonic averages

$$\text{harm}(a, b) = \frac{a \cdot b}{a + b}.$$

We used both methods and found little difference in the resulting solution. This stems from the fact that the dominant term $g(x)D\nabla Q$ originating from the subcellular scale is in a form where it is convenient to apply mimetic finite differences to compute $D\nabla Q$ on a face, hence leaving g the only term to average. We did not test the implementation of the upwind method rigorously, because it is quite simple to implement and moreover, we cross-checked it against the well-tested convection implementation in Dune [BBD$^+$08b, BBD$^+$08a, BHM10]. The discretization of the convection term can be put into a matrix P acting on the cell variables.

4.2.3 Time stepping

For the time stepping scheme, it is convenient regarding computation time (which is of particular importance to the clinical application) to employ a semi-implicit method. The convection-diffusion part, especially the diffusion, needs to be resolved implicitly, while the reaction part, consisting of the growth, is not a stiff problem due to the small growth constants (for more details refer to table 4.5) and hence may be resolved explicitly. The overall method has to be exact of first order - we cannot expect more, because the upwind for the convection part and the mimetic finite differences on a non-convex domain, like the brain, are only of first order -, so we use an implicit Euler stepping for the convection-diffusion part and per

computational cell a fourth order Runge-Kutta method for the reaction part. The overall scheme for a time step τ reads

$$(I + \tau\mathcal{A})\, u_h^{k+1} = u_h^k + \tau\Phi\left(f(u_h^k)\right),$$

where $\mathcal{A} = (-DIV\ M_F^{-1}\ DIV^T\ M_C) + P$ represents the linear system stemming from the discretization of the convection-diffusion part, whereas Φ shall stand for the numerical flux associated with the fourth order Runge-Kutta method.

Note 4.2.3. *With the higher order explicit scheme for the reaction part we do not gain any order of convergence, but the explicit one-step schemes are very easy to implement and very cheap during execution of the code, so they have at least no negative influence compared to a corresponding explicit first order scheme: in contrary, the numerical code may profit from the higher accuracy.*

4.3 Processing the data

In this section we want to document how the implementation of the data processing took place. With processing we mean the inclusion of real medical data into the numerical code. Recall (confer to the data chapter 3) that we have ideally the quantities q describing the tissue fibre orientation, Q standing for the volume fraction of tissue fibres as well as a segmentation, which gives information of the different tissues in the brain, or at least information about where the brain tissue is located. For the different models, we need to compute the quantities

- $\int_{\mathbb{S}^2} \xi \otimes \xi q(\xi) d\xi$
- $\int_{\mathbb{S}^2} \int_{\mathbb{S}^2} G(\xi,\eta)\xi \otimes \eta q(\xi) q(\eta) d\eta\ d\xi$
- $\int_{\mathbb{S}^2} \int_{\mathbb{S}^2} G(\xi,\eta)\xi \otimes \eta q(\xi) \nabla q(\eta) d\eta\ d\xi,$

a process that cannot be done analytically, due to the selection of the orientation distribution function as tissue fibre orientation. However, for different choices as the peanut or the bimodal von-Mises-Fisher distribution, this is possible [PH13]. So we need to employ a numerical integration method, and we chose Monte-Carlo integration was inspite of the fact that it is clearly not optimal with a mean convergence rate of $\frac{1}{2}$. However, more elaborate possibilities for spherical integration, like best approximation formulae, which require to solve additional linear systems to minimize the discrepancy, are harder to implement. This is clearly possible, but not necessary, because we are solving the forward problem, so it is not of importance whether the integration is exact for three or seven digits. For the actual integration it is

very convenient to use parallelization, because solving the integrals per voxel are tasks that are independent of each other. To accomplish this task, we rely on the framework OpenMP [Ope16], which is automatically enabled in the code, if present.

4.3.1 The single integral

The single integral

$$\int_{\mathbb{S}^2} \xi \otimes \xi q(\xi) d\xi$$

is very straightforward to implement, so we do not discuss this in detail. For testing the code, we used the water diffusion tensor $D_W = I$ leading to the orientation distribution function $q = \frac{1}{4\pi}$. Now we have to compute for this test case the integral explicitly, which has been done in [Hil05]. So we have

$$\int_{\mathbb{S}^2} \xi \otimes \xi q(\xi) d\xi = \frac{1}{3} I.$$

The convergence result is as expected (see table 4.3). The error row contains the error in a matrix related norm. We use the Frobenius norm, which is equally sensitive for all entries. The row convergence is the actual error divided by the error corresponding to half of the points, as in the previous tables 4.1 and 4.2. One expects that by doubling the number of points, the error should multiply by $\frac{1}{\sqrt{2}}$, which is around 0.7071, and can be verified in table 4.3.

Number of points	500	1000	2000	4000	8000
Error in Fro-norm	0.05746	0.0212005	0.0154376	0.0107685	0.00867506
Convergence	∞	0.3690	0.7282	0.6976	0.8056

Table 4.3: Convergence of the single integration code for the test case

4.3.2 The double integral

The second double integral involving the gradient of q is just the same to implement as the first one, if the gradient is precomputed, for which we employ first and second order finite differences. The domain has a lot of boundary voxels, where a centred second order scheme is not possible and so we use a first order difference in the outer rim of the domain.

So to compute the integral

$$\int_{\mathbb{S}^2}\int_{\mathbb{S}^2} G(\xi,\eta)\xi\otimes\eta q(\xi)q(\eta)d\eta\ d\xi,$$

we need to employ regularization, because we are confronted with a singular integral. Recall that Green's function reads

$$G(\xi,\eta)=\frac{1}{4\pi}\left(\ln\left(\frac{1-\xi\cdot\eta}{2}\right)+1\right),$$

which has a singularity in $\xi=\eta$. To avoid the integration over this singularity, we use the so-called space regularized sphere function

$$G^{\rho}(\xi,\eta)=\begin{cases}\frac{1}{4\pi}\left(\ln\left(\frac{1-\xi\cdot\eta}{2}\right)+1\right) & \xi\cdot\eta<1-\rho\\ \frac{1-\xi\cdot\eta}{4\pi\rho}+\frac{1}{4\pi}\left(\ln(\rho)-\ln(2)\right) & \xi\cdot\eta\geq 1-\rho\end{cases},$$

which is a linearly extrapolated version of G around $\xi\cdot\eta=1-\rho$. This function can be found for example in [FS08] in combination with a proof that the value of the regularized integral converges to the original one. In the simulations and tests, we use $\rho=0.01$, because the error scales with ρ and so the expected errors of the regularization and the Monte-Carlo integration are of the same order. Moreover, we tested the independence of the integration with respect to the parameter ρ for smaller values.

Now we opt for the test case $q=\frac{1}{4\pi}$ as before. Then the double integral simplifies to

$$\int_{\mathbb{S}^2}\int_{\mathbb{S}^2} G(\xi,\eta)\xi\otimes\eta q(\xi)q(\eta)d\eta d\xi=\frac{1}{(4\pi)^2}\int_{\mathbb{S}^2}\int_{\mathbb{S}^2} G(\xi,\eta)\xi\otimes\eta d\eta d\xi$$

The latter one has to be computed. Therefore, the integral

$$\int_{\mathbb{S}^2} G(\xi,\eta)\eta d\eta$$

is rewritten as the solution to the problem

$$\begin{aligned}\Delta^{\star}g(\xi)&=\xi\\ \int_{\mathbb{S}^2} g(\xi)d\xi&=0,\end{aligned}$$

where both equations are understood component-wise. This PDE on the sphere is solved by $g(\xi)=-\frac{1}{2}\xi$ fulfilling also the side condition. Then the double integral simplifies to

$$\frac{1}{(4\pi)^2}\int_{\mathbb{S}^2}-\frac{1}{2}\xi\otimes\xi d\xi,$$

for which the value is known as $-\frac{1}{24\pi}I$ [Hil05].

As before, the actual numerical code has the expected convergence rate as seen in table 4.4, where the conventions of the previous table 4.3 apply.

Number of points	500	1000	2000	4000	8000
Error in Fro-norm	0.00450304	0.00170246	0.00121828	0.0008613	0.000686214
Convergence	∞	0.3781	0.7156	0.7070	0.7967

Table 4.4: Convergence of the double integration code for the test case

4.4 Assessing the parameters

We included the medical data in the numerical code, but we still need to select the parameters. This is easy for some of them, because measurements are available. Others, however, cannot be measured and have to be estimated, while there is also one free parameter, where it is not yet clear in which region typical values should lie. Nevertheless this free parameter confers flexibility to the model, enhancing or suppressing anisotropy, which can be easily seen in the simulations on real data (see figures 4.5 and 4.6). It remains to estimate the following parameters:

- The cell speed s: This is measurable for different types of cells, at least in vitro, but also in mouse models, where few cells, which can be tracked, are implanted into a rodent. In [CS95] the cell speed was measured for glioma cells to be around $2.1 \cdot 10^{-7} \frac{\mathrm{m}}{\mathrm{s}}$.

- The attachment and detachment rates k^+ and k^-: These are a bit trickier to assess, because measurements are available only for the detachment rate [LL93]. We expect the attachment rate to be of the same order of magnitude, so selecting $k^+ = k^- = 0.1 \frac{1}{\mathrm{s}}$ is a reasonable choice.

- The mean turning rate λ_0: K. Wolf (Radboud Univ. Nijmegen, unpublished data at the time of writing) measured it to be $0.8 \frac{1}{\mathrm{s}}$ and is also used in [EHS15] and [HS16].

- The growth rate c_g: This can be estimated, which is done in the following.

- The incremental turning rate λ_1: This is the free parameter in the model, that enables to adjust the visible anisotropy on a per patient basis. It cannot be measured, neither is it clear which sign this constant should have. In previous papers [EHKS14, EKS16, EHS15] the rate was proposed to be $1000 \frac{1}{\mathrm{s}}$, what is very large, especially in the light that the overall rate $\lambda(z)$ has to stay positive, so we are more conservative and select it between $-100 \frac{1}{\mathrm{s}}$ and $100 \frac{1}{\mathrm{s}}$. We include negative values, because we want to assess the sensitivity of the result with respect to this parameter (see figures 4.5 and 4.6).

There are two different possibilities to assess the growth rate c_g. On the one hand, one can rely on measurements. This is widely accepted and used, but has the shortcomings that

Parameter	s	$k^+,\ k^-$	λ_0	λ_1	c_g
Value (in $\frac{1}{\mathsf{s}}$)	$0.21 \cdot 10^{-6}\mathsf{m}$	0.1	0.8	$-100 - 100$	$8.44 \cdot 10^{-7}$

Table 4.5: Model parameters used in the numerical simulation

a tumour doubling rate is measured, however not from the complete tumour, but only from the visible part of it consisting of up to 80 % of the tumour cell density. If these volume doubling rates are present, it is not known how to transform these in a reliable manner into a cell density growth rate. The other possibility is to rely on the cell cycle, which was estimated for glioma to be about 57 hours [HWRB75], so the cell density is expected to double after this time span, if all cells are actively cycling. However, this is not the case, so there is a need for further measurement of cells that are in cycle. In [UGR99] the authors estimated the fraction of actively cycling cells to be around 25-30 %. So the rate c_g computes as $\frac{\text{fraction of actively cycling cells}}{\text{duration of a cell cycle}} \ln(2) \approx 8.44 \cdot 10^{-7} \frac{1}{\mathsf{s}}$, as in [EHS15].

The table 4.5 summarizes the actual values of the parameters used in the numerical code. Note that the units in which the constants are given are not used in the numerical code, but we transformed them with the compile-time `ratio` implementations of C++ to the desired ones (days and millimetres). The compile time logic is less error prone than by doing the conversion manually and yields more accurate results, because floating-point errors are mostly avoided.

4.5 Numerical Simulations

4.5.1 Implementation

We want to comment on the actual implementation of the reaction-convection-diffusion-equation. Overall, we use a splitting scheme in order to have only a linear system that is solved in a sequence, so there is only the need of assembling this linear system once. Starting the programme, it first reads the configuration and loads the segmentation, because this data set contains only integer variables, typically in a range of -1 to 8 - in the case of a pure brain mask, as is the case for the example data set that is used for illustration of the diffusion tensor reconstruction in Camino [CBG$^+$06], only 0 and 1.

With this segmentation a `YaspGrid` of Dune [BBD$^+$08b, BBD$^+$08a] is generated for a bounding box and afterwards all voxels not contained in the brain mask are removed with the aid of `dune-multidomaingrid`. Then the actual computation engine is started. It first loads the needed data (only for the voxels in the brain mask, so we do not waste memory by loading a lot of matrices containing zeros). The initial values are loaded, applied, and then

the associated memory is freed. Then the expression

$$\begin{pmatrix} -DIV^T\ M_C & M_F \\ I + \Delta t\ P & \Delta t\ DIV \end{pmatrix} \begin{pmatrix} p \\ u \end{pmatrix} = \begin{pmatrix} 0 \\ g \end{pmatrix}$$

is assembled, where it is convenient to compute only the matrices M_F, DIV and $I + \Delta t\ P$. Recall that the matrix M_C is globally diagonal and the effect is a multiplication by $|c|$. During this phase it is necessary to compute $D\nabla_x Q$ for the drift terms. This is done via mimetic finite differences, so M_F and DIV are assembled first, then the matrix P. During this computation we use the `ILU0`-preconditioned `BiCGSTAB`-solver, as implemented in `dune-istl` [BB07, BB08] to the reduction 10^{-14}. After the assembly step, there is no need to hold any data beyond Q in memory, so the rest is released in order not to waste resources.

During a step in the simulation phase, the right hand side g is computed and the system is solved with the aid of the Schur-complement:

$$p = \left(I + \Delta t \left(P - DIV\ M_F^{-1}\ DIV^T\ M_C\right)\right)^{-1} g,$$

where we do not need to compute u, because we are only interested in the density variable. Here we need two solvers, for the outer inverse and for M_F^{-1}. Both are solved with `ILU0`-preconditioned `BiCGSTAB`-solvers to the different reductions 10^{-14} for the outer solve, hence also for the complete system, and 10^{-8} for the inner solve. This is used because of a discrepancy in the orders of magnitude of p and u.

After the solve we inserted the (not essential) step of checking non-negativity of the solution, in the sense that we call a value negative if it is smaller than -`std::numeric_limits<double>::epsilo` so against machine precision. Note that the comparison of a value smaller than 0.0 does not make sense (and is not fulfilled in general). This restrictive check generates warnings and should not fail for too many voxels; as we did not smooth the data and use iterative solvers, we cannot expect the non-negativity to hold true in all voxels. In the following simulations, this check failed for 4 voxels out of over 167549 meaning less than 0.003%, with values around -10^{-14}, so with an error expected from the iterative solver. We compensated the negativity by setting the corresponding solution there to 0, because we really want to preserve non-negativity. If one is interested in having a very exact monotony of the method, we would recommend to switch from iterative solvers for the linear systems (allowing an error which is huge (10^{-14}) compared to machine precision ($2.25 \cdot 10^{-16}$)), to direct solvers acting much more accurately. These are much slower and need more memory, but have the positive effect that due to the smaller error, the non-negativity is preserved in a better way. Unfortunately, there seems to be a memory barrier implemented in `SuiteSparse` solvers (`UMFPack` and `SPQR`) that only allows for memory allocation up to 4 gigabytes, at least in the packages

corresponding to our Linux-platform. So one may have to switch to another direct solver like `Amesos(2)`, available in the `Trilinos` package, but we did not try it.

After the solution step, the values are updated and written to the disk, if requested.

We tested the programme with memcheck from `valgrind` against memory leaks and found none, apart from one `Singleton` instance (reported as still reachable) of `OpenMPI`. This is clearly desired, when experimenting with real data that expands to around 1 gigabyte in memory.

In the previous paragraph, we referred to a lot of software packages without citing them. This is intentional, because we did not use them in the version of the code employed to generate the simulations for the present text. Moreover, `SuiteSparse` is a very high quality numerical package for solving linear systems directly and well-suited for smaller-scale simulations, like two dimensional ones.

4.5.2 Results

We use the previously described numerical method to simulate the equations (2.23) and (2.40) deduced in subsections 2.4.5 and 2.4.6 via parabolic scaling of the mesoscopic equations. The simulations will exclusively take place on the dataset bundled with Camino [CBG+06]. We have chosen this one, as it has the advantage of the whole work being under our control: estimation of the water diffusion tensors, a task done by non-linear inversion, and computation of the necessary quantities D, $\tilde{D}$ and U. This gives us confidence, the possibility to choose the best fitting algorithms, and illustrates the working programme pipeline from the raw medical data to the numerical simulation. As initial condition we use

$$\rho_0(x) = 1_{\exp\left(-\frac{|x-x_0|^2}{2}\right)\geq 0.3} \exp\left(-\frac{|x-x_0|^2}{2}\right),$$

where the point $x_0 = (46, 51, 26)^T$ measured in slice indices of the data set is chosen such that the centre x_0 is located in a highly anisotropic region of the brain, presumably a white matter tract (see figure 4.1). The brightness in the second picture of figure 4.1 is scaled with the fractional anisotropy defined in the data chapter 3. The colours are according to the standard DTI visualizations, hence the red component describes the left-right, the green component the antero-posterior and the blue component the superior-inferior orientations. The initial condition is only used for illustrative purposes, because the data stems from a healthy subject and not from a real patient with a brain tumour.

In the visualizations we always scale the colour bar at the bottom of each picture to the actual value range of the visualized quantity. Although the numerical method employed is monotone, there are very few negative values visible, but they are indistinguishable from 0 in the selected machine precision. The images in this section stem from three dimensional

calculations, unless stated otherwise. For the sake of visualization, we cut out a single slice (here the 26th) of the three dimensional simulation.

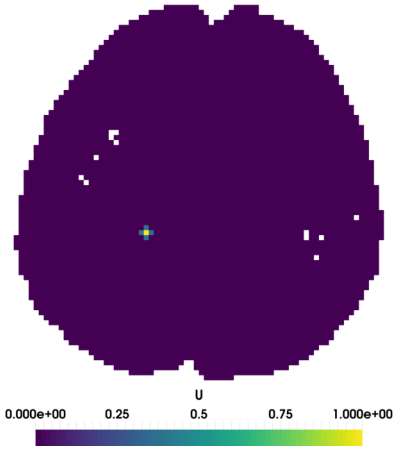

(a) The initial condition used in the following

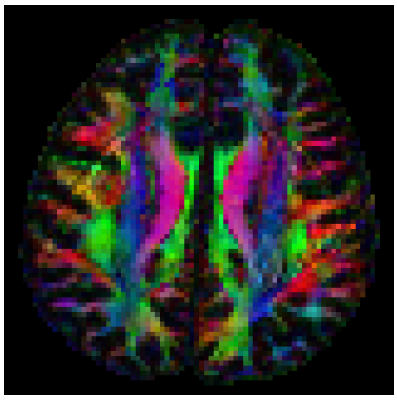

(b) The visualized DTI data

Figure 4.1: The initial condition and the brain data. To see the effect of the white matter tracts on the artificial tumour, we locate the initial condition in a highly anisotropic region in the brain.

The main difference between the first model featuring the velocity jump process and incorporating an integrin-mediated proliferation term leading to equation (2.23) and the second one based on a Gaussian process and incorporating the integrin-mediated proliferation term as well, corresponding to equation (2.40) is the diffusion tensor. For identical tissue fibre orientation distributions, the tensor $\tilde{D}$ (in (2.40)) is about a factor 8π smaller than D (in (2.23)) (see the test case of isotropic diffusion for the computation of D and $\tilde{D}$). As the convection term stemming from the subcellular level ($g(Q(x))\ D\nabla_x Q$) stays the same in both models, the second one is more dominated by convection for the same parameter choice. This results in higher visible anisotropy of the simulated cell density. This means that we can reproduce finger like infiltrative tumour spread for both models, but this behaviour will be visually more dominant for (2.40).

Starting from the same initial condition (see figure 4.1), we simulated equation (2.23) (see the second column in figure 4.2) and equation (2.40) (see the third column of figure 4.2) up to 600 days. One can easily see that the simulations confirm the expectations that the equation (2.40) will give rise to more anisotropy and finger-like spread, however, both models do comply with real diagnosed tumour shapes [SC$^+$12]. Nevertheless, there is a need for the quantitative assessment of the models in comparison to the tumour spread in vivo;

this is ongoing work.

As stated, all simulations seen in figure 4.2 are carried out in three dimensions in order not to neglect the possibility of the tumour to invade the visualized brain slice using the third dimension. This actually happens, as seen in figure 4.3, where we exemplify the difference between one slice of the three dimensional simulation and the two dimensional simulation directly performed on that brain slice and by using the model (2.40) at time 600 days. The visual difference stems from the difference of dimensions, as the data used in the computation is exactly the same. All other natural sciences (psychology, physics, biology and others) do their brain data analysis, not necessarily based on MRI data, also in three dimensions, as the brain function (and hence also the white matter tracts) cannot be confined into a brain slice.

All the simulations here were done with the semi-implicit scheme described previously. However, it is known that a splitting scheme as employed here will result in an additional error compared to a purely implicit calculation. We do need the speed of the semi-implicit simulation to fulfil the strict time requirements of clinical practice, where the result has to be available as fast as possible for therapy planning. This is not feasible for the fully implicit calculation, because it takes substantially longer to terminate (in our case around a day for a simulation up to $t = 600$ days). So we checked our semi-implicit scheme by using model (2.23) (see figure 4.4) to time $t = 600$ days. The difference is very small, although we are comparing the semi-implicit scheme using a fourth order Runge-Kutta method for the non-linear part to an implicit Euler scheme. Hence the error is not prohibitively large and we may use the faster method. Moreover, assessing the visual difference between figures 4.4 (a) and (b), the shape of the simulated tumour spread is exactly the same, so it will represent the prediction to use in the clinical practice.

As we have a free parameter (λ_1) in our models, we need to evaluate the impact of it on the simulation outcome. As mentioned before, this parameter controls the anisotropy, so it enables or inhibits the finger-like spread, if it is larger or smaller, respectively. So we simulated both models for different values for λ_1, positive as well as negative. The results can be seen in figure 4.5 for equation (2.23) and in figure 4.6 for equation (2.40) at time $t = 600$ days.

For growing absolute values of λ_1, the simulations reveal finer structures within the tumour bulk compared to the simulation with neglected influence of subcellular dynamics, corresponding to $\lambda_1 = 0$ (see figure 4.5 (a) and (i) in comparison to (e) and figure 4.6 (a) and (i) versus (e)). In the case of model (2.23), the image corresponding to the parameter $\lambda_1 = 0$ (figure 4.5 (e)) shows a rather regular tumour shape. This means that the tumour spreads equally in all directions, whereas, and this is remarkable, in the case of the second model (2.40) the corresponding image (figure 4.6 (e)) is less regular. The shape follows the central white matter fibre tract (see figure 4.1 (b), the white matter tract on the right in the

left half of the brain).

In the last decades there were introduced a plethora of brain tumour models (as noted in the introduction). However, two of them, the model by the group of Swanson [JJHD$^+$15, RAJRS09, HCS$^+$12, JMD$^+$05] and the model introduced by Painter and Hillen [PH13, HP13] are natural candidates for comparison to the models introduced in this text, because the type of the resulting equation is the same.

As equation representing the model of Swanson we will use

$$\partial_t \rho = \operatorname{div}(D\nabla\rho) + c_g Q(x)\rho(1-\rho), \tag{4.9}$$

where D is our tumour diffusion tensor. Here we imposed the identical growth term as in model (2.23) to get the closest results. Everything else would diverge too much in order to enable a proper comparison. The results for the simulation of both models until time $t = 600$ days can be seen in figure 4.7

For the comparison we have a look at time $t = 400$. We visualized the differences between model (4.9) and model (2.23) with $\lambda_1 = 0$ and $\lambda_1 = 100$ in figures 4.8 and 4.9, respectively. One can see clearly the effect of the myopic diffusion of model (2.23) compared to the Fickian type of model (4.9) in figure 4.8: model (2.23) predicts a larger spread of the tumour, especially in the outer regions, which is also visible in figure 4.7. So model (2.23) predicts a more aggressive cancer as (4.9). Including the subcellular dynamics in the simulation (see figure 4.9) the mentioned effect will be even more pronounced, but there is a second effect: the subcellular dynamics leads to a focus of the tumour cells onto the diagonal white matter tract in the centre of the simulated tumour (so the visualized negative part is greater than 0, where the white matter tract is located and the positive part will be greater than 0 at the boundaries of this region of high anisotropy). Hence model (2.23) predicts there a larger cell density, which will migrate at a higher speed in the white matter tract and characterizes a more malignant tumour. This is an important issue, since the efficiency of therapy is tightly related to the difficulty of exhaustively resecting or irradiating the neoplastic regions. The tumour recidive is actually due to the cancer cells originating from the untreated margins.

Now we have a look at the model proposed by Painter and Hillen [PH13]. We include an additional growth term, hence we will use the modified version of their model

$$\partial_t \rho = \operatorname{div}\operatorname{div}(G\rho) + c_g Q(x)\rho(1-\rho), \tag{4.10}$$

where G is the tumour diffusion tensor D, but for a different fibre orientation distribution. They proposed the bimodal von-Mises-Fisher distribution

$$q(x,\theta) = \frac{k(x)}{8\pi \sinh(k(x))} \left(\exp\left(\theta \cdot \phi k(x)\right) + \exp\left(-\theta \cdot \phi k(x)\right)\right),$$

where $k(x) = \kappa \cdot FA(x)$ and $FA(x)$ is the fractional anisotropy. The vector ϕ is selected to be the leading eigenvector of the water diffusion tensor, which is given by the diffusion tensor imaging data. As the value of κ cannot be measured, we are using $\kappa \in \{0.5, 1, 5\}$. We did simulations to the model (4.10) to the same initial condition as for our models and visualized the result on slice 26 (figure 4.10).

Now we turn to compare the simulation outcomes of the model (4.10) with different values of κ to (2.23) with $\lambda_1 = 0$. This means we are comparing the impact of different distributions for the fibre orientation on the simulation outcome what we are doing by considering the differences (seen in figure 4.11) to time $t = 400$ days. As the model (2.23) has a strong focus on the white matter tract, the difference between (4.10) with $\kappa \leq 1$ and (2.23) with $\lambda_1 = 0$ is high at the boundary, where the white matter tract is located (yellow regions in figure 4.11 for $\kappa = 0.5$ and $\kappa = 1$). However, the difference between both models at this part of the boundary decreases with increasing κ. The simulation outcome for $\kappa = 5$ focuses only on the white matter tract and hence the choice of the bimodal von-Mises-Fisher distribution as orientation distribution neglects the other anisotropic regions (the peak in the upper region of the simulated tumour at time $t = 400$ days in the simulation of (2.23) with $\lambda_1 = 0$ compared to the simulation of (4.10) with $\kappa = 5$ seen in figure 4.10). So the bimodal von-Mises-Fisher distribution is good to express high anisotropy (using appropriate values of κ), but fails to be the cause for anisotropic simulation outcomes, when the fibres are not aligned. The local difference between both models ((4.10) and (2.23)) is not negligible (local error of over 60% of the maximal simulated value) and can only be assessed with the aid of a known tumour spread during the validation of the model. However, as the orientation distribution function seems to be the correct concept and the leading eigenvector of the water diffusion tensor is not a good measure for the direction of the fibres in all voxels [JKT13], we will stick to the orientation distribution function until the difference between both distributions was assessed during model validation.

For the comparison of the model (2.23) including the subcellular dynamics ($\lambda_1 = 100$), we use (4.10) with $\kappa = 1$, as the visual difference between (4.10) with $\kappa = 1$ and (2.23) with $\lambda_1 = 0$ is smallest among the values for κ we used. This can be seen by comparing the second and fourth row of images in figure 4.10. So we look at the difference $D = U_1 - U_2$ between the simulation outcome of (4.10) (U_1) and (2.23) with $\lambda_1 = 100$ (U_2) seen in figure 4.12. The model (2.23) focuses on the white matter tract (and so D is larger than 0 at the boundary of the white matter tract). This can be seen in figure 4.12 (b). However, the additional drift term originating from the subcellular dynamics leads to a larger tumour spread and so to a higher simulated malignancy (figure 4.12 (c)).

We do not do any comparison of models (4.9) and (4.10) to the model (2.40), as the behaviour is visually completely different. This is due to the lower diffusion speed of model (2.40) and the higher anisotropy when the subcellular dynamics is included (see figure 4.6

(i)). Moreover, when comparing to (4.10) there is also the different type of diffusion: Myopic diffusion for (4.10) and something in between myopic and Fickian diffusion for model (2.40). So we restrain from an in depth comparison between those models.

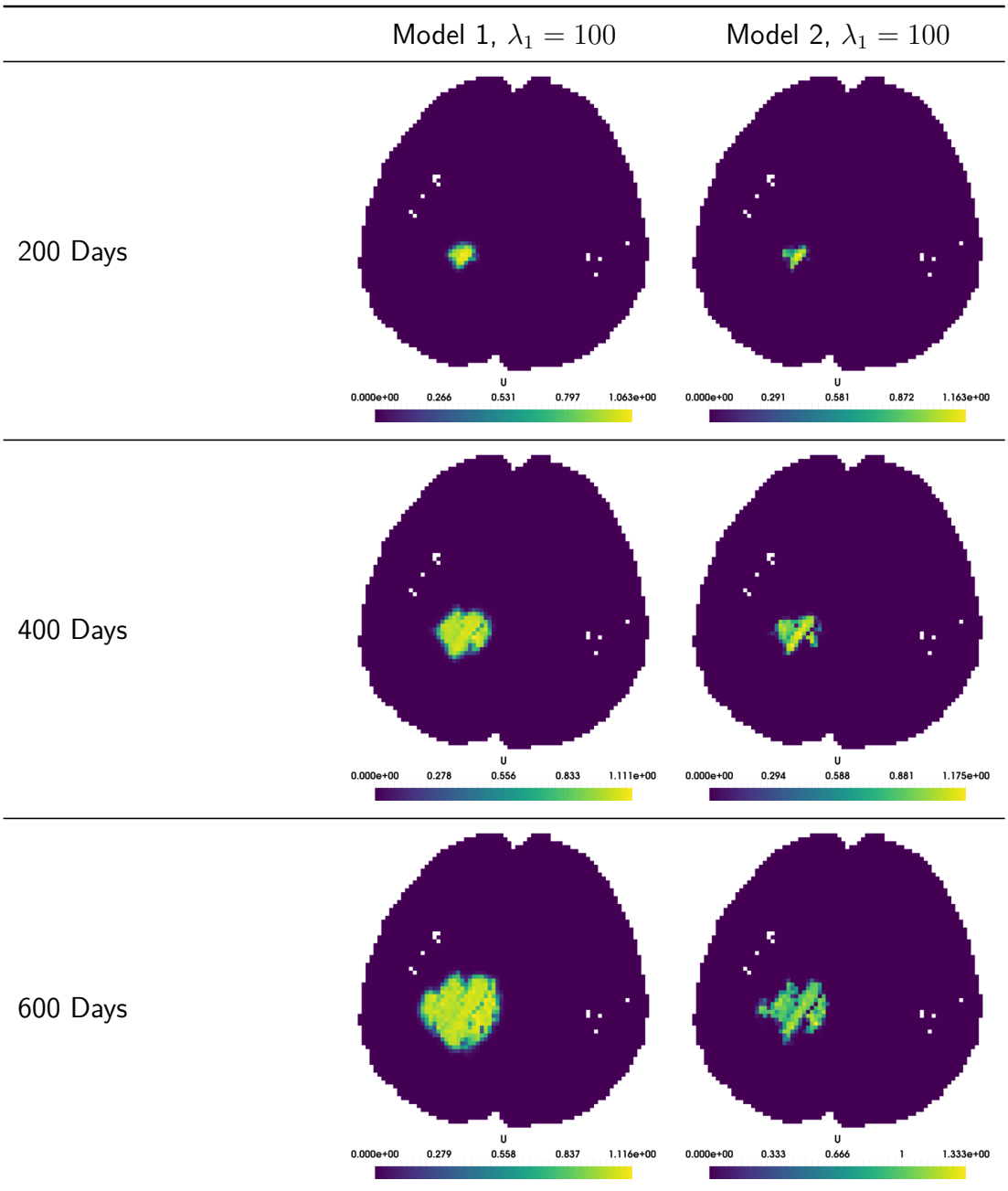

Figure 4.2: Simulation of model (2.23) (left column) and model (2.40) (right column) to $\lambda_1 = 100$. The effect of the data on the simulation of the artificial tumour is obvious, as the simulation generates highly anisotropic shapes and especially the model (2.40) leads to a strong focus on the white matter tracts.

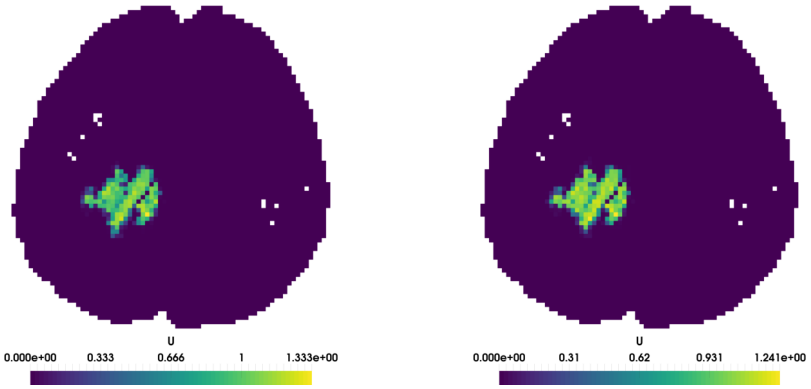

(a) 3D Simulation, visualized on slice 26

(b) 2D Simulation on slice 26

Figure 4.3: Comparing 2D and 3D simulations of the model (2.40) at $t = 600$ days. The difference between the two simulations is not negligible, especially in the lower tip of the tumour bulk, hence for a reliable prognosis we need to rely on the full three dimensional simulation.

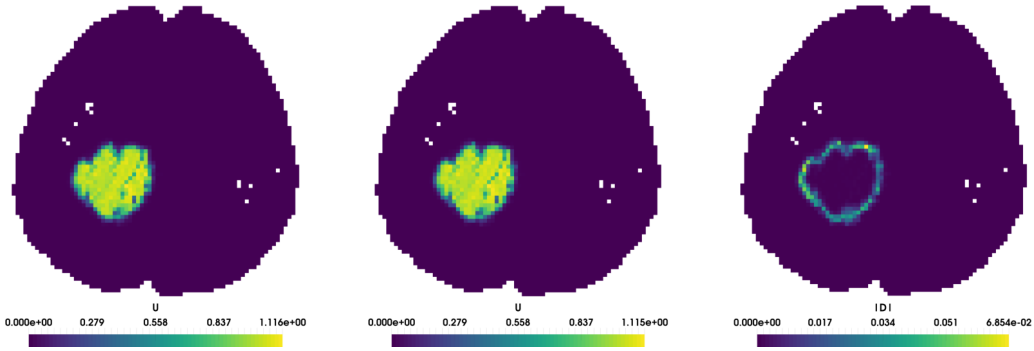

(a) Semi-implicit simulation

(b) Implicit simulation

(c) The absolute value of the difference

Figure 4.4: Comparing semi-implicit and implicit calculation at time 600 days of model (2.23). The local error is around 7 %, so we may use the semi-implicit simulation to speed up the runtime.

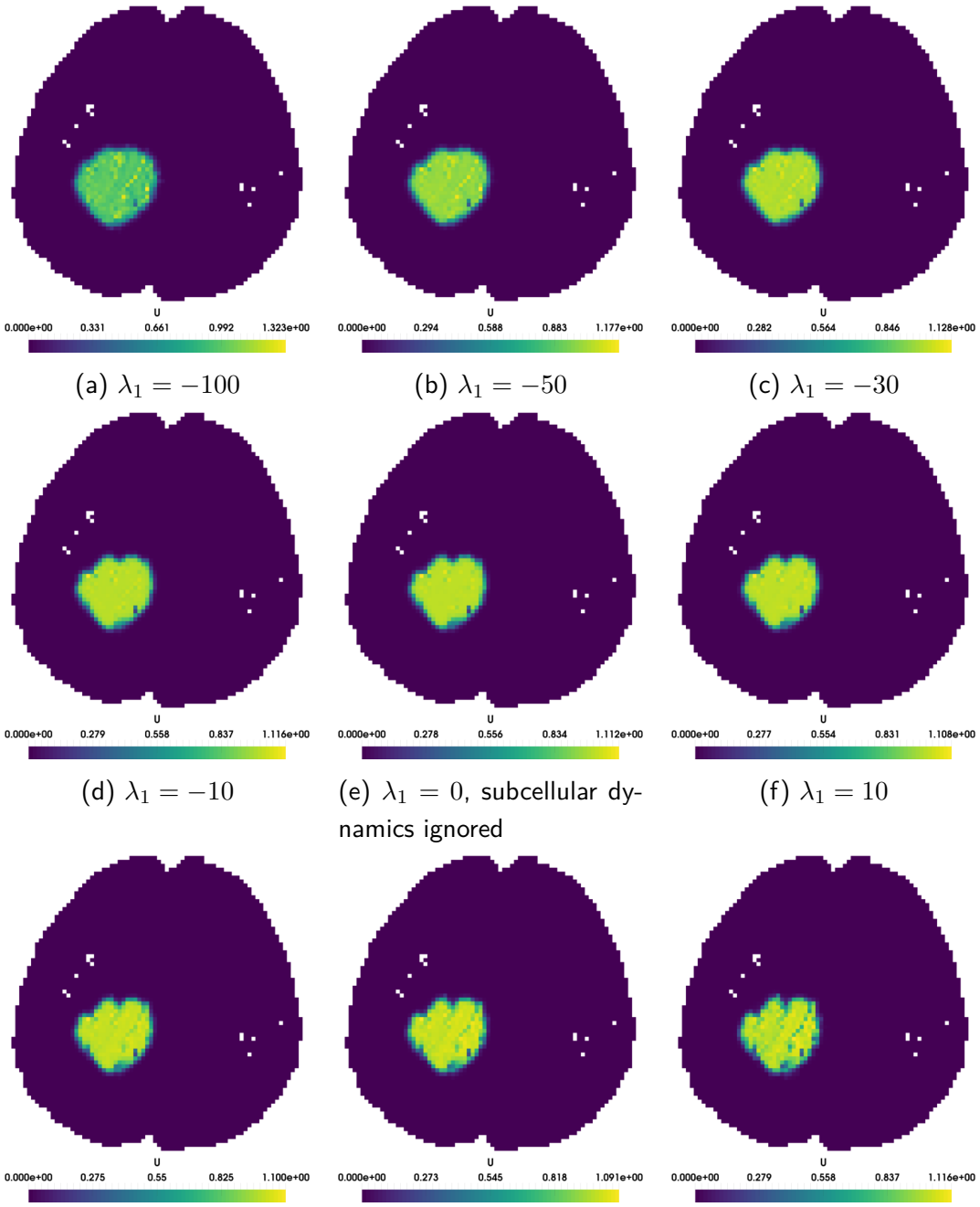

(a) $\lambda_1 = -100$ (b) $\lambda_1 = -50$ (c) $\lambda_1 = -30$

(d) $\lambda_1 = -10$ (e) $\lambda_1 = 0$, subcellular dynamics ignored (f) $\lambda_1 = 10$

(g) $\lambda_1 = 30$ (h) $\lambda_1 = 50$ (i) $\lambda_1 = 100$

Figure 4.5: Model (2.23) for different values of λ_1 at time $t = 600$ days. Higher absolute values of λ_1 enhance the visual anisotropy. Negative values of λ_1 partly (compare $\lambda_1 = -100$ with $\lambda_1 = 0$) makes the overall shape more symmetric (so the borders of the artificial tumour are nearer to a circle shape than in the simulation without subcellular dynamics). Higher values of λ_1 (see $\lambda_1 = 100$) reveal finer structures, so especially the lower right part of the simulated tumour separates better from the main cell mass than in the simulation with $\lambda_1 = 0$.

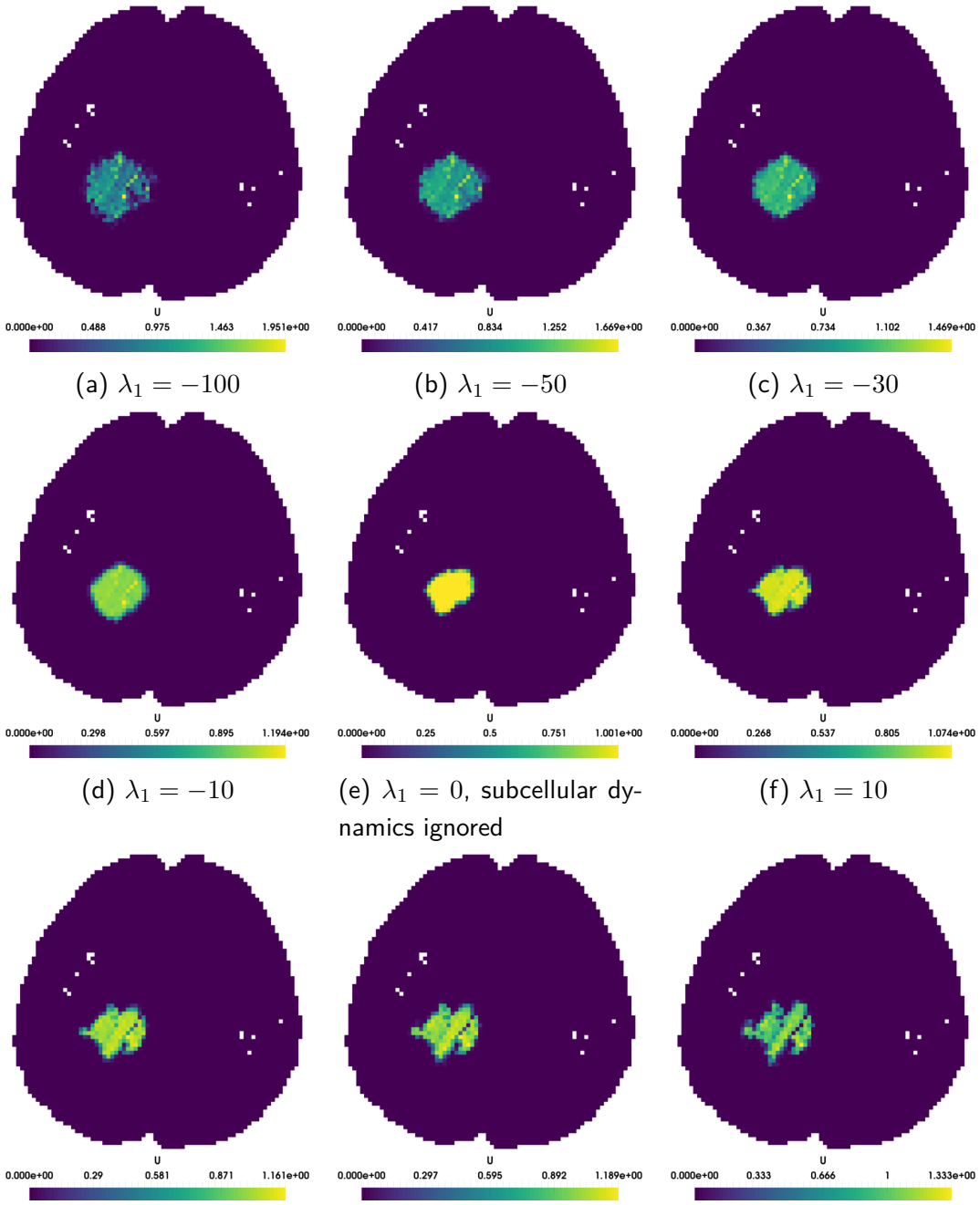

(a) $\lambda_1 = -100$ (b) $\lambda_1 = -50$ (c) $\lambda_1 = -30$

(d) $\lambda_1 = -10$ (e) $\lambda_1 = 0$, subcellular dynamics ignored (f) $\lambda_1 = 10$

(g) $\lambda_1 = 30$ (h) $\lambda_1 = 50$ (i) $\lambda_1 = 100$

Figure 4.6: Model (2.40) for different values of λ_1 at time $t = 600$ days. The generated shapes are different from the ones in the previous figure (4.5) while the overall structure stays the same: higher values of λ_1 (especially $\lambda_1 = 100$) lead to highly irregular shapes, so the left part of the simulated tumour is almost separated from the rest. Lower values of λ_1 (see especially $\lambda_1 = -100$) are visually rounder than the simulation corresponding to $\lambda_1 = 0$.

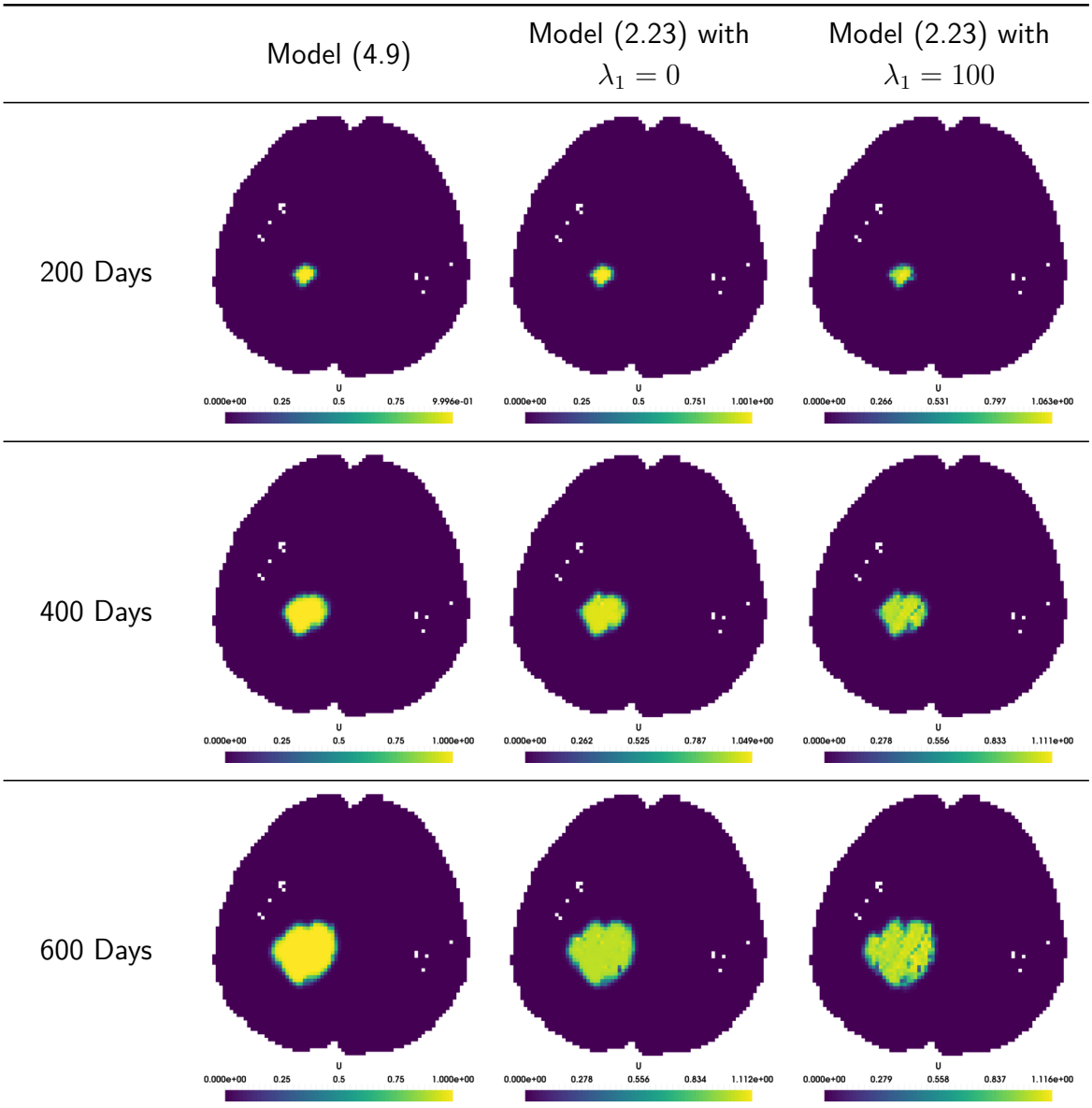

Figure 4.7: Simulations of model (2.23) and (4.9) visualized on slice 26. The visual shape of the simulated tumour becomes more irregular from left to right, so the most regular shape is generated by (4.9) and the most irregular shape by (2.23) including subcellular dynamics ($\lambda_1 = 100$). So especially for glioblastoma multiforme, which is known to generate irregular shapes, the model (2.23) might be more appropriate than (4.9)

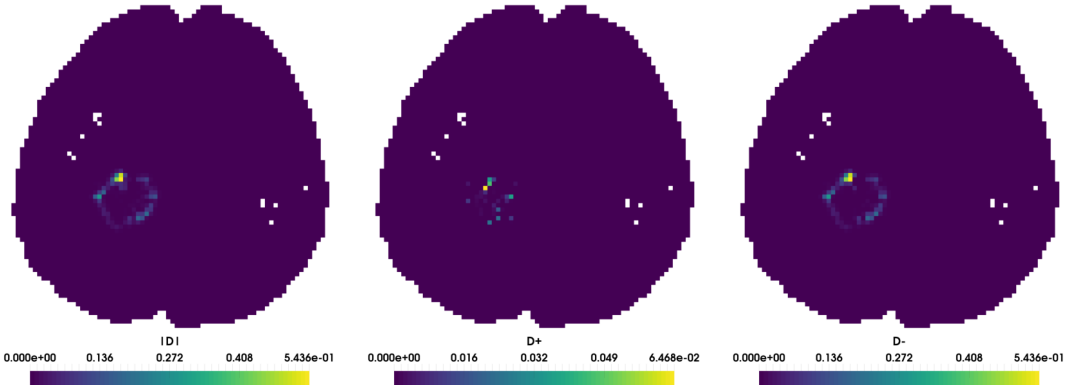

(a) Absolute value (b) Positive part (c) Negative part

Figure 4.8: Visualized the difference $D = U_1 - U_2$ between model (4.9) (U_1) and model (2.23) (U_2) to $\lambda_1 = 0$. The additional drift term of U_2 leads to a larger spread of the tumour in the outer rim. This means that the model (2.23) without influence of the subcellular level predicts a larger tumour extent than (4.9).

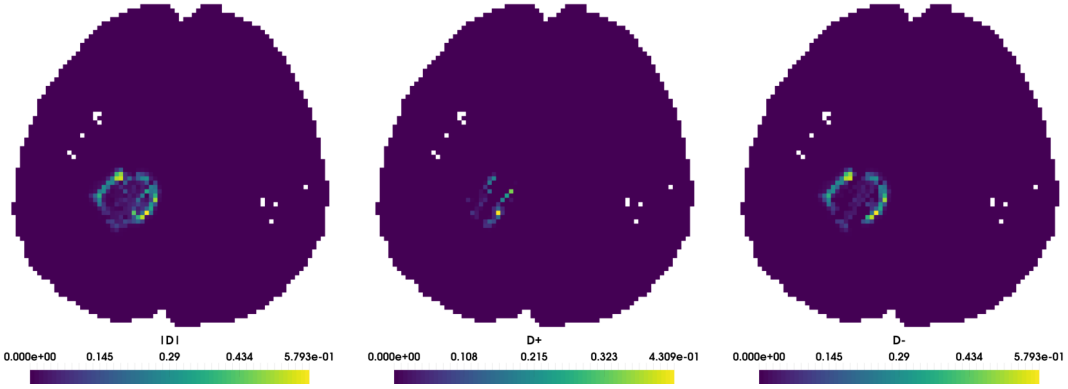

(a) Absolute value (b) Positive part (c) Negative part

Figure 4.9: Visualized difference $D = U_1 - U_2$ between model (4.9) (U_1) and model (2.23) (U_2) to $\lambda_1 = 100$. Including the subcellular dynamics enhances the major difference between model (4.9) and (2.23). So model (2.23) predicts a larger spread of the tumour at the edge of the tumour bulk, but also finer structures, thus it focuses the cell density more on the diagonal white matter tract in the centre of the simulated tumour.

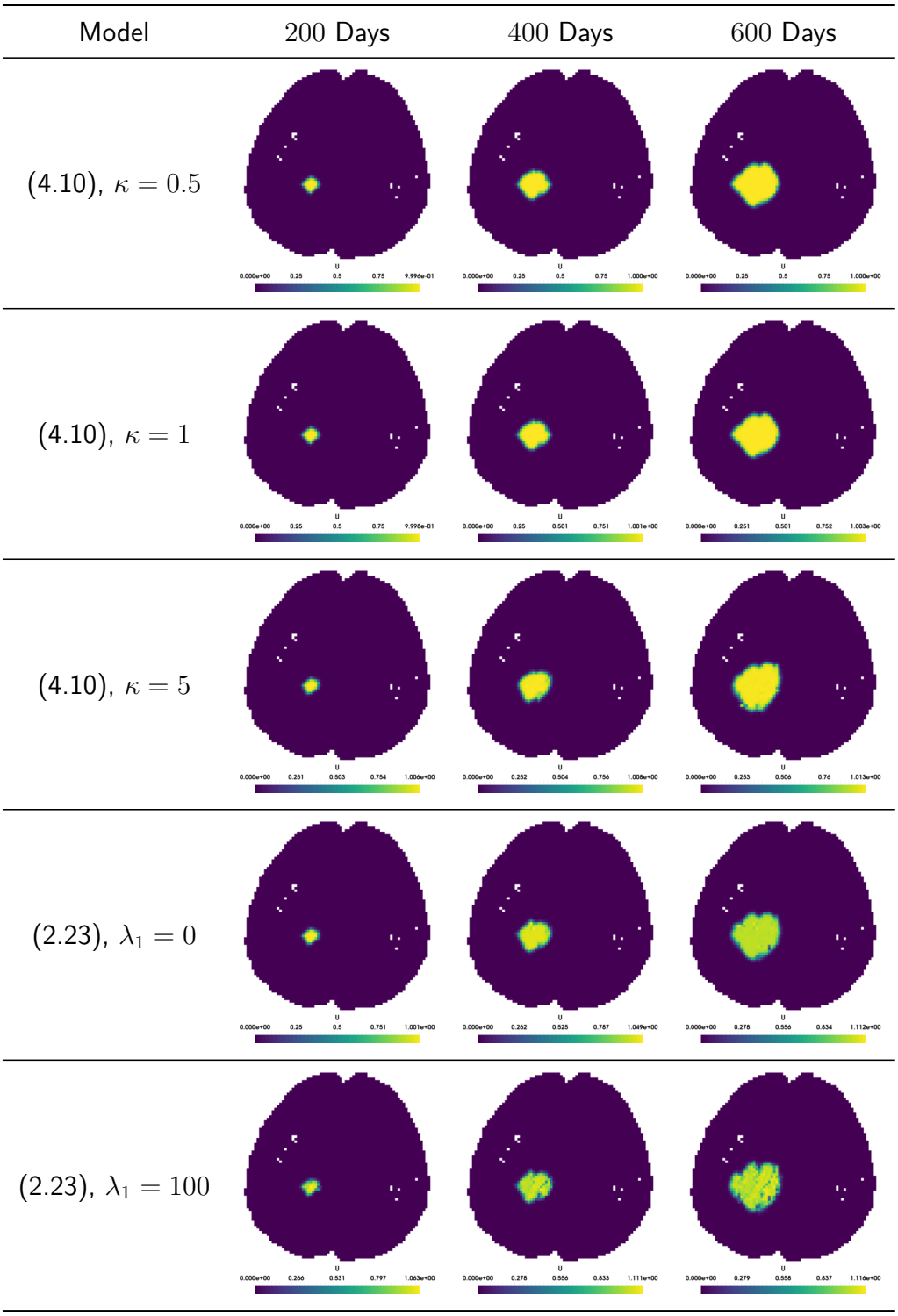

Figure 4.10: Three dimensional simulation of model (2.23) and (4.10) visualized on slice 26. Higher values of κ lead to higher visual anisotropy, but cannot generate the finer structures seen in the simulation of (2.23) with subcellular dynamics ($\lambda_1 = 100$).

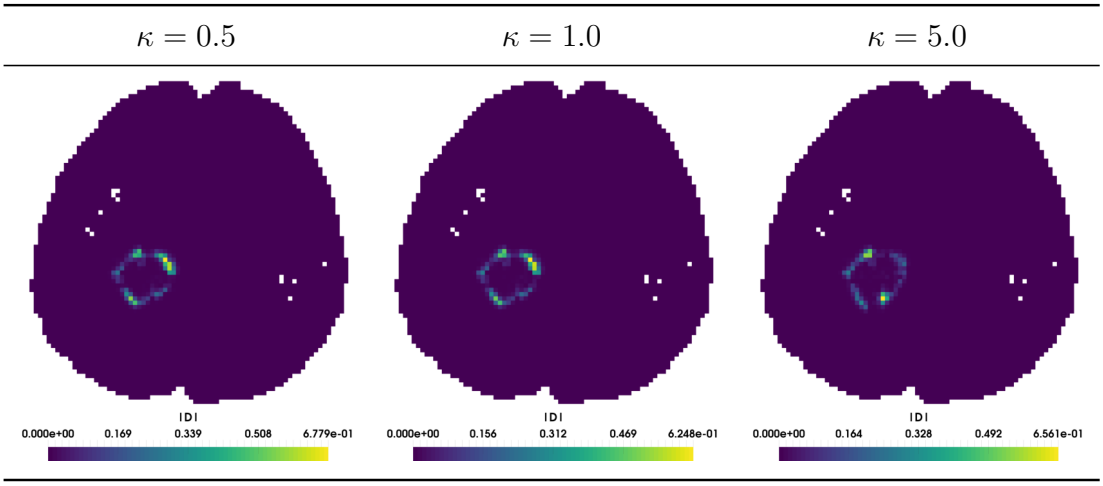

Figure 4.11: The absolute values of the differences between the simulations of (4.10) for different values of κ and (2.23) without subcellular dynamics.

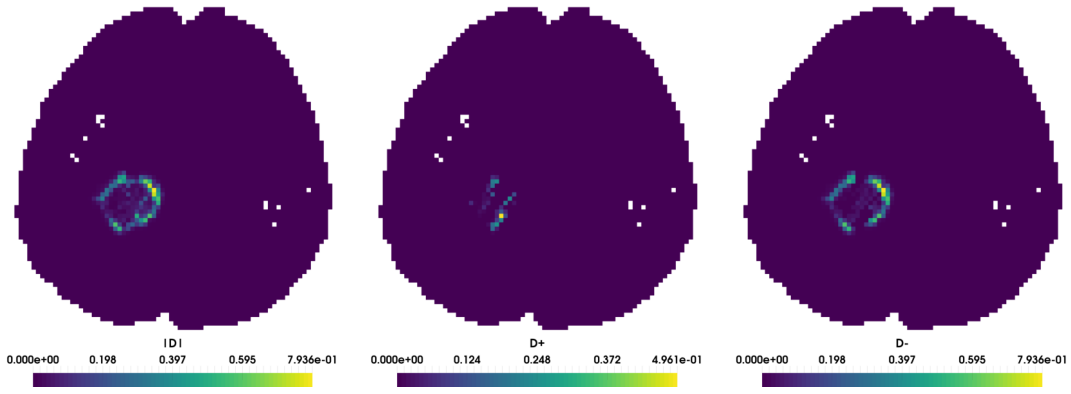

(a) Absolute value (b) Positive part (c) Negative part

Figure 4.12: Difference $D = U_1 - U_2$ of model (4.10) with $\kappa = 1$ (U_1) and (2.23) with subcellular dynamics $\lambda_1 = 100$ (U_2). The model including subcellular dynamics accounts for a larger tumour spread (seen in (c)) and finer structures within the tumour bulk (seen in (a) and (b)).

Chapter 5

Therapy

Another important aspect is therapy. There are plenty of different therapy approaches to treat brain tumours: chemotherapy targeting at tumour cell death, radiotherapy, resection, and a combination of two or all of them. Each of these therapies was modelled separately during the last years: Chemotherapy [SMAC05, dPGR06], radiotherapy [RRM$^+$10] and resection [SBMA03, SAM03]. However, there is a new class of so-called peptidomimetics aiming at glioblastoma therapy by targeting e.g cell surface receptor bindings [CCRW12, GBBW03]. While the standard therapy for newly diagnosed glioblastomas consists of surgical resection, radiotherapy and concurrent chemotherapy with a chemotherapeutic agent aiming at cell death like temozolomide [FFB$^+$07, SRD$^+$07], the new agents are or were in clinical trials in combination with radiotherapy [CCRW12]. These new agents are the outcome of newer studies hinting that the cell-ECM interactions enhance cell survival after radiation exposure [CSD$^+$06]. Additionally, integrins on the surface of host cells like endothelial cells, perivascular cells or fibroblasts (to name a few, all of which are inhibited in the same context during therapy), can boost the malignant potential of a tumour by mediating core hallmarks like angiogenesis or lymphangiogenesis [DC10].

The type of treatment consisting of radiotherapy and concurrent chemotherapy with such a new drug was addressed in [HS16]. In the following we present the findings therein, adjusted to fit the model class described previously. In particular, the change of the variable y to z will be done already in the presentation, contrary to the deduction of the model in [HS16]. The main difference between the therapy model and the models presented in this text so far (also being the motivation of this independent chapter) is the different description of the growth. The therapy model is based on [EKS16], where the proliferation was included via the go-or-growth dichotonomy. This leads to two coupled equations on the mesoscopic scale not directly fitting to the description of the microscopic scale presented here. A deduction of these equations from an underlying microscopic system, is however possible. The only

drawback from the modelling perspective is the utilization of additional free parameters, which are very difficult to assess, if possible at all. This is because there is yet no data available about the net effects of the new chemotherapeutic agents on the cellular scale. In contrast, for single integrins the effectiveness of these chemicals is well-tested, as they are or were studied in clinical trials [CCRW12]. Unfortunately, we cannot include the data for a single integrin receptor in our model, as we modelled the subcellular scale as the net effect of receptors.

5.1 Description

We will use the quantities $q(x, v)$ and $Q(x)$ already employed in the previous chapters. For the modelling which was done in [EKS16], we start now from the mesoscopic point of view and include the proliferation with the aid of the go-or-growth dichotomy as already mentioned in the subsection about the proliferation term 2.4.3. This means that we need two different subpopulations, a migrating (denoted by $p_m(t, x, v, z)$) and a proliferating (and hence not moving) one, the latter denoted by $p_p(t, x, z)$). For the description of the migration, we rely on the mesoscopic equation associated to the velocity jump process

$$\partial_t p_m + \operatorname{div}_x (v p_m) - \operatorname{div}_z \left(\left(\left(k^+ Q + k^- \right) z + f'(Q) v \cdot \nabla_x Q \right) p_m \right) = \mathcal{L}[\lambda(z)] p_m$$

with the same notation $\mathcal{L}$ for the turning operator. In chapter 2, we were interested in the macroscopic cell density

$$M = \int_V \int_Z p(t, x, v, z) dz \; dv,$$

but now we are interested in the macroscopic cell density

$$N = \int_Z \left(\int_V p_m(t, x, v, z) \, \mathrm{d}v + p_p(t, x, z) \right) \, \mathrm{d}z,$$

which is the sum of the macroscopic cell densities for the two subpopulations. Including natural cell death into both subpopulations with rates l_m and l_p, both dependent on the overall cell density N and modelling growth only for the non moving subpopulation with a rate g that may also depend on N, we arrive at the system

$$\begin{aligned} &\partial_t p_m + \operatorname{div}_x (v p_m) - \operatorname{div}_z \left(\left(\left(k^+ Q + k^- \right) z + f'(Q) v \cdot \nabla_x Q \right) p_m \right) \\ &\qquad = \mathcal{L}[\lambda(z)] p_m - l_m(N) p_m \\ &\partial_t p_p = \left(g(N) - l_p(N) \right) p_p. \end{aligned}$$

Then we need to model the process of proliferating cells switching to the moving phenotype, hence the transition of a proliferating cell into a migrating one, and the change of a migrating cell into a proliferating one. The process of starting to move is especially problematic to include, because we need to choose an orientation to which the cell migrates. This is one free parameter choice, which is avoided using the mesoscopic proliferation term described in the modelling section. Nevertheless, we can extract some limit information out of the system as it stands. Assuming that the proliferating and migrating cells are the same cell type, but only with different velocities of migration, leads to the applicability of the movement description of the migrating to the proliferating ones, but only in steady state. The equilibrium orientation of the cells is, as analyzed before, $q(x,v)$, so it is reasonable to assume that the starting cells are distributed accordingly. The process of stopping is not problematic, because there we only lose information about the orientation. Then the system including the stopping (a) and starting rate (b), both later dependent on the delivered dose of chemotherapeutical agent, reads

$$\begin{aligned}
&\partial_t p_m + \operatorname{div}_x(v p_m) - \operatorname{div}_z\left(\left(\left(k^+ Q + k^-\right) z + f'(Q) v \cdot \nabla_x Q\right) p_m\right) \\
&\qquad = \mathcal{L}[\lambda(z)] p_m - a p_m + b q p_p - l_m(N) p_m \\
&\partial_t p_p = a \int_V p_m(v) dv - b p_p + (g(N) - l_m(N)) p_p.
\end{aligned} \tag{5.1}$$

To include radiotherapy, we rely on the findings that different types of cells have different sensitivity against radiation. To have a local model, we assume that the effect of radiation can be described with a single loss term in each equation. This does make sense, as we want to model the net loss on the mesoscopic (cell density) scale and not the effect of radiation on the subcellular level - here we mean not the integrin bindings, but the cell hits degrading the DNA chain. We denote these loss terms by R_m and R_p, respectively. Because we are using the volume fraction of tissue fibres Q in our model, which is also affected by the radiation, if applied, we have to take the surviving fraction $S(\alpha_Q, \beta_Q, d_r)$ of these into account. So the model including radiotherapy reads

$$\begin{aligned}
&\partial_t p_m + \operatorname{div}_x(v p_m) \\
&\quad - \operatorname{div}_z\left(\left(\left(k^+ S Q + k^-\right) z + f'(SQ) v \cdot \nabla_x (SQ)\right) p_m\right) \\
&\qquad = \mathcal{L}[\lambda(z)] p_m - a p_m + b q p_p - \left(l_m(N) + R_m\right) p_m \\
&\partial_t p_p = a \int_V p_m(v) dv - b p_p + (g(N) - l_m(N) - R_p) p_p.
\end{aligned} \tag{5.2}$$

For the actual choice of the loss terms involving the corresponding surviving fraction, we adopt the linear-quadratic (LQ) model, which is standard to the clinical practice [RKD11, SSS02], although there is strong evidence of its failure in some situations [BHH$^+$95, KMM08].

This was also done in [RRM+10] in order to include radiotherapy. The standard for brain tumours is to give the overall radiation dose in several fractions, ν in this context, so the loss terms can be modelled via

$$R_j = \sum_{i=1}^{\nu} (1 - S(\alpha_j, \beta_j, d_r))\, \eta_\delta(t - t_i) \quad j \in \{m, p\},$$

where α_j and β_j are the sensitivity parameters of the LQ model, S stands for the surviving fraction, and η_δ is a mollifier with support in $[-\delta, \delta]$. These supports are assumed not to overlap, meaning that the radiotherapy is given in timely distinct slots and not continuously, an assumption in accordance with clinical practice. With d_r we denote a fractional dose given at times t_i, $i = 1, ..., \nu$. The surviving fraction can be computed with the aid of the LQ model as

$$S(\alpha_j, \beta_j, d_r) = \exp\left(-\left(\alpha_j d_r + \beta_j d_r^2\right)\right), \quad j \in \{m, p, Q\}.$$

In the model we included proliferation and radiotherapy, but we want to model a type of chemotherapy that aims at inhibiting the cell-ECM interactions. Due to their importance to every subcellular process, all the rates k^+, k^-, a and b will depend on the drug delivery. We expect k^+ to be decreasing with growing drug dosis (denoted by d_c), whereas k^- is increasing, meaning that the cell is more likely to detach from the fibres, as the modelled chemotherapeutical substance is supposed to inhibit receptor binding to tissue fibres. The integrins are needed for migration, so it is natural to assume the stopping rate to increase with the drug delivery and the starting rate to decrease. We selected in the paper [HS16] the functions

$$k^+(d_c) = 0.1\left(1 + \frac{d_c}{1 + d_c^2}\right) \qquad k^-(d_c) = 0.1\,(1 + d_c)$$

$$a(d_c) = 0.05\,(1 + d_c) \qquad b(y) = 0.1\left(1 + \frac{d_c}{1 + d_c^2}\right).$$

In absence of chemotherapy ($d_c = 0$), these rates are exactly those chosen in the table 4.5 (k^+ and k^-) and in the paper [EKS16] for a and b. The main problem here is that we do not even have quantitative information about the strength of the chemotherapeutical effect, but we are looking forward to new data to become available from clinical trials. With these, the model has to be revised, evaluated and adapted to the real outcomes. Nevertheless, the model gives insight into the interplay between subcellular processes like binding and unbinding to the ECM and radiotherapy. In order to allow comparison to the previous proliferation model, we use

$$g(N) = c_g$$
$$l_j(N) = c_g N, \quad j \in \{m, p\}$$

resembling logistic growth. The constant c_g is chosen as in table 4.5. Thus we get the system

$$\begin{aligned}
&\partial_t p_m + \operatorname{div}_x (v p_m) \\
&\quad - \operatorname{div}_z \left(\left(\left(k^+(d_c) SQ + k^-(d_c) \right) z + f'(SQ) v \cdot \nabla_x (SQ) \right) p_m \right) \\
&\qquad = \mathcal{L}[\lambda(z)] p_m - a(d_c) p_m + b(d_c) q p_p - (c_g N + R_m) p_m \\
&\partial_t p_p = a(d_c) \int_V p_m(v) dv - b(d_c) p_p + (c_g - c_g N - R_p) p_p.
\end{aligned} \tag{5.3}$$

Note 5.1.1. *In [HS16] we made the transition $y \to z$ after the modelling of the therapy, while here, most due to presentation reasons, the transition was already made before. This proceeding results in a slight change of the drift term in z, additionally to the difference in the signs of λ_1 and z. This has no effect on the macroscopic scale, because the difference in the drift terms is a time derivative that is scaled afterwards by ε^2 in [HS16] and hence vanishes in the parabolic limit, which is of interest here.*

5.2 Extracting the macroscopic behaviour

For the deduction of a macroscopic equation, we use parabolic scaling as in chapter 2 ($t \to \varepsilon^2 t$, $x \to \varepsilon x$) in order to extract the limit information:

$$\begin{aligned}
&\varepsilon^2 \partial_t p_m + \varepsilon \operatorname{div}_x (v p_m) \\
&\quad - \operatorname{div}_z \left(\left(\left(k^+ \left(d_c SQ + k^-(d_c) \right) z + \varepsilon f'(SQ) v \cdot \nabla_x (SQ) \right) p_m \right) \right) \\
&\qquad = \mathcal{L}[\lambda(z)] p_m - a(d_c) p_m + b(d_c) q p_p - \varepsilon^2 (c_g N + R_m) p_m \\
&\varepsilon^2 \partial_t p_p = a(d_c) \int_V p_m(v) dv - b(d_c) p_p + \varepsilon^2 (c_g - c_g N - R_p) p_p.
\end{aligned} \tag{5.4}$$

Let us define the moments

$$\begin{aligned}
m &= \int_Z p_m(z) dz & m^z &= \int_Z z p_m(z) dz & m^{zz} &= \int_Z z^2 p_m(z) dz \\
M &= \int_V m(v) dv & M^z &= \int_V m^z(v) dv & M^{zz} &= \int_V m^{zz}(v) dv \\
W &= \int_Z p_p(z) dz & W^z &= \int_Z z p_p(z) dz,
\end{aligned}$$

where in order to ensure the closure of the resulting system we assume that the second order moments m^{zz} and M^{zz} vanish. As done in the modelling section, we set up moment equations by integrating the system (5.4) with respect to z, and by multiplying it with z and

integrating afterwards. For the sake of notation convenience, we write $L_m = c_g N + R_m$ and $L_p = c_g N + R_p$. This leads to

$$\begin{aligned}
&\varepsilon^2 \partial_t m + \varepsilon \operatorname{div}_x (vm) = \lambda_0 (qM - m) + \lambda_1 (qM^z - m^z) - am + bqW - \varepsilon^2 L_m m \\
&\varepsilon^2 \partial_t W = aM - bW + \varepsilon^2 (c_g - L_p) W \\
&\varepsilon^2 \partial_t m^z + \varepsilon \operatorname{div}_x (vm^z) + (k^+ SQ + k^-) m^z + \varepsilon f'(SQ) v \cdot \nabla_x (SQ)\, m \\
&\qquad = \lambda_0 (qM^z - m^z) - am^z + bqW^z - \varepsilon^2 L_m m^z \\
&\varepsilon^2 \partial_t W^z = aM^z - bW^z + \varepsilon^2 (c_g - L_p) W^z.
\end{aligned}$$

In a way compatible to the previous models we consider Hilbert expansions $\Xi = \sum_{k=0}^{\infty} \Xi_k \varepsilon^k$ for

$$\Xi \in \{m, m^z, M, M^z, W, W^z\}$$

and collect the corresponding powers of ε:

ε^0:

$$\begin{aligned}
0 &= \lambda_0 (qM_0 - m_0) + \lambda_1 (qM_0^z - m_0^z) - am_0 + bqW_0 \\
0 &= aM_0 - bW_0 \\
(k^+ SQ + k^-) m_0^z &= \lambda_0 (qM_0^z - m_0^z) - am_0^z + bqW_0^z \\
0 &= aM_0^z - bW_0^z.
\end{aligned}$$

Integrating these equations with respect to v, we deduce

$$M_0^z = 0 \qquad W_0^z = 0 \qquad m_0^z = 0$$
$$m_0 = qM_0 \qquad W_0 = \frac{a}{b} M_0.$$

ε^1:

$$\begin{aligned}
\operatorname{div}_x (vm_0^z) &= \lambda_0 (qM_1 - m_1) + \lambda_1 (qM_1^z - m_1^z) - am_1 + bqW_1 \\
0 &= aM_1 - bW_1 \\
(k^+ SQ + k^-) m_1^z + f'(SQ) v \cdot \nabla_x (SQ)\, m_0 &= \lambda_0 (qM_1^z - m_1^z) - am_1^z + bqW_1^z \\
0 &= aM_1^z - bW_1^z.
\end{aligned}$$

Proceeding as before, we deduce

$$W_1 = \frac{a}{b} M_1 \qquad W_1^z = \frac{a}{b} M_1^z,$$

so integrating the third ε^1-equation above with respect to v and using the symmetry of the tissue fibre orientation (which we assume for the velocity jump case) we arrive at

$$(k^+ SQ + k^-) M_1^z = 0,$$

hence $M_1^z = W_1^z = 0$. This results in the identity

$$m_1^z = -\frac{f'(SQ)v \cdot \nabla_x (SQ)\, m_0}{k^+ SQ + k^- + \lambda_0 + a}.$$

Inserting this into the first ε^1-equation, we get

$$m_1 = \frac{1}{\lambda_0 + a}\left(q\,(M_1 + bW_1) - \operatorname{div}_x (vm_0) + \frac{f'(SQ)v \cdot \nabla_x (SQ)\, m_0}{k^+ SQ + k^- + \lambda_0 + a}\right).$$

Observing that integrating $vq(M_1 + bW_1)$ with respect to v results in 0 due to the symmetry of q and the fact that neither M_1 nor W_1 depend on v, we can compute

$$\int_V vm_1 dv = \frac{1}{\lambda_0 + a}\Bigg(- \operatorname{div}_x \left(\int_V v \otimes vq(v)dv M_0\right) + \frac{\lambda_1 f'(SQ) \int_V v \otimes vq(v)dv \cdot \nabla_x (SQ)\, M_0}{k^+ SQ + k^- + \lambda_0 + a}\Bigg).$$

Using the convenience notations

$$\Lambda = \frac{1}{\lambda_0 + a}\int_V v \otimes vq(v)dv \qquad \text{and } \gamma(Q) = \frac{\lambda_1 f'(SQ)}{k^+ SQ + k^- + \lambda_0 + a},$$

we have

$$\int_V vm_1 = -\operatorname{div}(\Lambda M_0) + \gamma(Q)\Lambda \nabla_x (SQ)\, M_0.$$

Directly integrating the ε^2 equations, we have

$$\partial_t M_0 + \operatorname{div}_x \left(\int_V vm_1 dv\right) = -aM_2 + bW_2 - L_m(N_0)M_0$$
$$\partial_t W_0 = aM_2 - bW_2 + (c_g - L_p(N_0))W_0,$$

so

$$\partial_t (M_0 + W_0) + \operatorname{div}_x \left(\int_V vm_1\right) = -L_m(N_0)M_0 + (c_g - L_p(N_0))W_0.$$

Using the formula for the term in the divergence operator, we get

$$\begin{aligned}&\partial_t N_0 - \operatorname{div}_x \left(\operatorname{div}_x \left(\frac{b(d_c)}{a(d_c) + b(d_c)}\Lambda N_0\right)\right) \\ &+ \operatorname{div}_x \left(\gamma(S(d_r)Q, d_c)\frac{b(d_c)}{a(d_c) + b(d_c)}\Lambda \nabla_x (S(d_r)Q)\, N_0\right) \\ &\qquad = \left(\frac{a(d_c)}{a(d_c) + b(d_c)}(c_g - L_p(N_0)) - \frac{b(d_c)}{a(d_c) + b(d_c)}L_m(N_0)\right) N_0. \quad (5.5)\end{aligned}$$

Theorem 5.2.1. *Let Ω be a region with Lipschitz boundary, the chemotherapy dose function $d_c\colon [0,T] \to \mathbb{R}$ be at least continuous and the parameter functions k^+, k^-, a and b be continuously dependent on d_c. Assume that $Q \in W^{1,\infty}$ and $q \in \{\phi \in L^\infty(\Omega \times V), \partial_x \phi \in L^\infty(\Omega \times V)\}$. Let the initial condition $N_0 \in L^2(\Omega)$ be non-negative. Then the macroscopic equation* (5.5) *has a non-negative weak solution.*

Proof. Analogous to the proof in the appendix to chapter 2. □

For a comment on the high regularity assumed in the previous theorem see remark 2.4.6 in the modelling chapter 2.

Rewriting the equation (5.5), we get

$$\begin{aligned}\partial_t N_0 - \operatorname{div}_x \operatorname{div}_x \left(\frac{b}{a+b}\Lambda N_0\right) + \operatorname{div}_x \left(\gamma(Q)\frac{b}{a+b}\Lambda \nabla_x (S(\alpha_Q, \beta_Q, d_r)Q) N_0\right) \\ = c_g \left(\frac{a}{a+b} - N_0\right) N_0 - \frac{aR_p(\alpha_p, \beta_p, d_r) + bR_m(\alpha_m, \beta_m, d_r)}{a+b} N_0.\end{aligned}$$

The task is now to choose the new parameters introduced. As in [HS16], we use for the radiation parameters α_j and β_j ($j \in \{m, p, Q\}$) measurements from cell lines as described in the table 5.1. The fractionated radiation dose d_r is chosen such that the overall dose νd_r is about 70Gy and a single dose d_r is not larger than 2 Gy, both clinically reasonable parameters.

Therapy model with novel chemotherapy in a nutshell:

With the aid of parabolic scaling and the assumption that the tissue fibre orientation is symmetric, the system of equations

$$\begin{aligned}&\partial_t p_m + \operatorname{div}_x (v p_m) \\ &\quad - \operatorname{div}_z \left(\left(\left(k^+(d_c SQ + k^-(d_c)\right) z + f'(SQ) v \cdot \nabla_x (SQ)\right) p_m\right) \\ &\qquad = \mathcal{L}[\lambda(z)] p_m - a(d_c) p_m + b(d_c) q p_p - (c_g N + R_m)\, p_m \\ &\partial_t p_p = a(d_c) \int_V p_m(v) dv - b(d_c) p_p + (c_g - c_g N - R_p) p_p\end{aligned}$$

leads to the macroscopic description for the overall cell density ρ

$$\begin{aligned}&\partial_t \rho - \operatorname{div}_x \operatorname{div}_x \left(\frac{b(d_c)}{a(d_c)+b(d_c)}\Lambda \rho\right) \\ &+ \operatorname{div}_x \left(\gamma(S(\alpha_Q, \beta_Q, d_r)Q, d_c)\frac{b(d_c)}{a(d_c)+b(d_c)}\Lambda \nabla_x (S(\alpha_Q, \beta_Q, d_r)Q)\rho\right) \\ &= c_g \left(\frac{a(d_c)}{a(d_c)+b(d_c)} - \rho\right)\rho - \frac{a(d_c)R_p(\alpha_p, \beta_p, d_r) + b(d_c)R_m(\alpha_m, \beta_m, d_r)}{a(d_c)+b(d_c)}\rho.\end{aligned}$$

Parameter	Value	Source
α_m	$(0.033 - 0.058)\frac{1}{\text{Gy}}$	Corresponding to cell line TK1 in [BS15]
α_p	$(0.311 - 0.401)\frac{1}{\text{Gy}}$	Corresponding to cell line A172 in [BS15]
α_Q	$0.37\frac{1}{\text{Gy}}$	Corresponding to fibroblasts in [BS15]
β_m	$(0.047 - 0.048)\frac{1}{\text{Gy}^2}$	Corresponding to cell line TK1 in [BS15]
β_p	$(0.061 - 0.091)\frac{1}{\text{Gy}^2}$	Corresponding to cell line A172 in [BS15]
β_Q	$(0.016 - 0.052)\frac{1}{\text{Gy}^2}$	Corresponding to fibroblasts in [BS15]

Table 5.1: The parameters for the LQ model for different cell types

So we have data based terms in every part of the equation, as before with the first model. The novel chemotherapeutical approach reflects in a change in every term of the equation, underlining the importance of the integrin bindings.

5.3 Simulation

We simulated the effect of two different types of therapy, namely with radiotherapy alone starting at time 0 for five weeks daily from Monday to Friday (here with $d_r = 2.0\,\text{Gy}$ and $\nu = 25$, which is in the range of standard therapy [FCF$^+$07]) and with radiotherapy including concurrent chemotherapy with $d_c = 10$ every Monday and Wednesday. The former is referred in this text as strategy 1 and the latter as strategy 2. We augment this with strategy 0 meaning no therapy at all.

The results are shown in figure 5.1. The model associated with equation (2.23) should not be compared directly to the model (5.5), because even in absence of radiation and chemotherapy, they are distinct through the different constants $\frac{a}{a+b}$ in the growth term and $\frac{b}{a+b}$ in the macroscopic diffusion tensor. For better comparability, we simulated (5.5) in the

absence of any therapy, hence providing the basic model for the comparison in figure 5.1. We used the same initial condition

$$\rho_0(x) = 1_{\exp\left(-\frac{|x-x_0|^2}{2}\right)\geq 0.3} \exp\left(-\frac{|x-x_0|^2}{2}\right)$$

with $x_0 = (46, 51, 26)^T$ measured in slice indices as in the chapter 4. Comparing model (2.23) introduced in chapter 2 and the one presented here (without therapy) we see that the former predicts a more aggressive tumour spread, while the overall characteristic that the tumour cell density orients along white matter tracts is preserved. There is a need for model validation to assess and evaluate the difference between both models critically. In figure 5.1 (c), one can see the effect of radiotherapy. The visible size of the tumour cell density shrinks when using simulated 2 Gy radiation dose per day (except weekends). It can be clearly seen that the tumour has not been eradicated, a fact well-known for glioblastoma multiforme, which can hardly be exhaustively treated with radiotherapy alone. Typically, a resection would have been applied before starting any further therapy efforts [SBMA03, SAM03].

In [SBMA03, SAM03] a method to model resection was proposed using an eradication of the tumour mass in a certain region contrary to the proposal in [HS16], where the tumour cell density was numerically set to 0, if above a predefined threshold. We do not want to include resection here, because side effects like removing brain matter and foreign oxygen supply affecting the tumour spread were completely neglected in the mentioned models. Moreover, introducing resection in the way of [SBMA03, SAM03, HS16] also introduces an additional non-linear, non-local, and even singular term in the equation. This is very challenging to use rigorously within a mathematical framework.

In order to assess the effectivity of the therapy, we used another larger initial condition

$$\rho_0(x) = 1_{\exp\left(-\frac{|x-x_0|^2}{2}\right)\geq 0.05} \exp\left(-\frac{|x-x_0|^2}{2}\right),$$

where the centre $x_0 = (45, 50, 37)^T$ is measured in slice indices (see figure 5.2). Note that strategy 1 consist of radiotherapy from day 0 to day 35 with a daily dose (except weekends) of 2 Gy. This accumulates to an overall dose of 50 Gy, which is quite low, but realistic for glioblastoma multiforme [FCF+07]. We did not use a higher dose for the simulation in order to assess the effect of the chemotherapy, which otherwise would be not perceivable. We now have a look at figure 5.3, where the simulation outcomes for the strategies 1 and 2 can be seen along with their difference. The effect of the concurrent chemotherapy is directly visible in the images corresponding to time $t = 100$ days. This is 65 days after the end of all simulated therapy efforts, so a classical follow-up after around 2 months. The concurrent chemotherapy had the desired effect to hinder the cells to spread. So the image to strategy 2 shows a smaller (both in absolute value and in occupied space) tumour, which is more

compact then its counterpart treated with strategy 1. The more compact and less diffuse shape of the tumour in strategy 2 will lead to a better prognosis. This positive effect visible 2 months after the end of the therapy can also be seen at time $t = 300$ days where the simulated tumour is still smaller and more compact than its counterpart in strategy 1, albeit no therapy was applied in between these times (see the last row of figure 5.3).

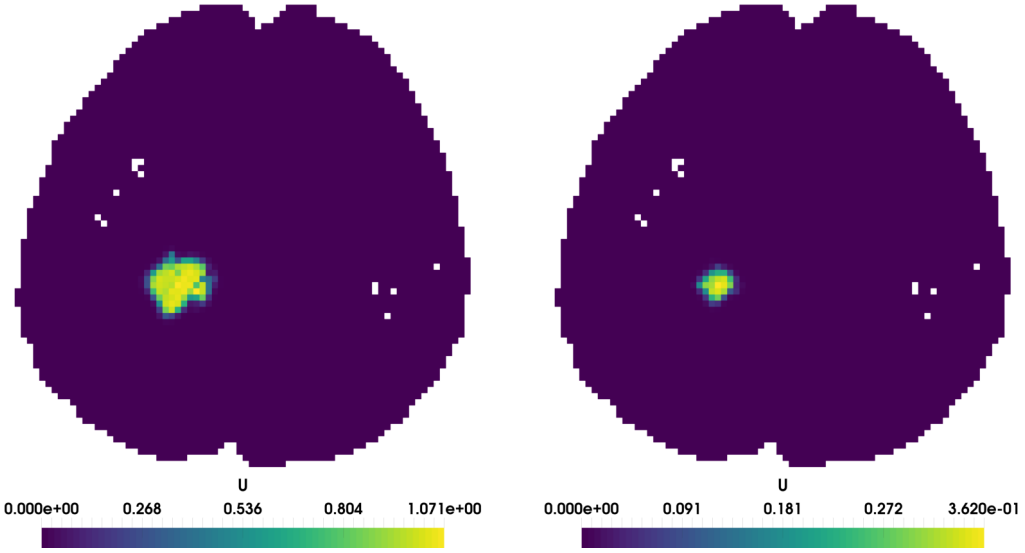

(a) Model (2.23) (without therapy), simulation at day 300

(b) Model (5.5) without therapy simulation at day 300

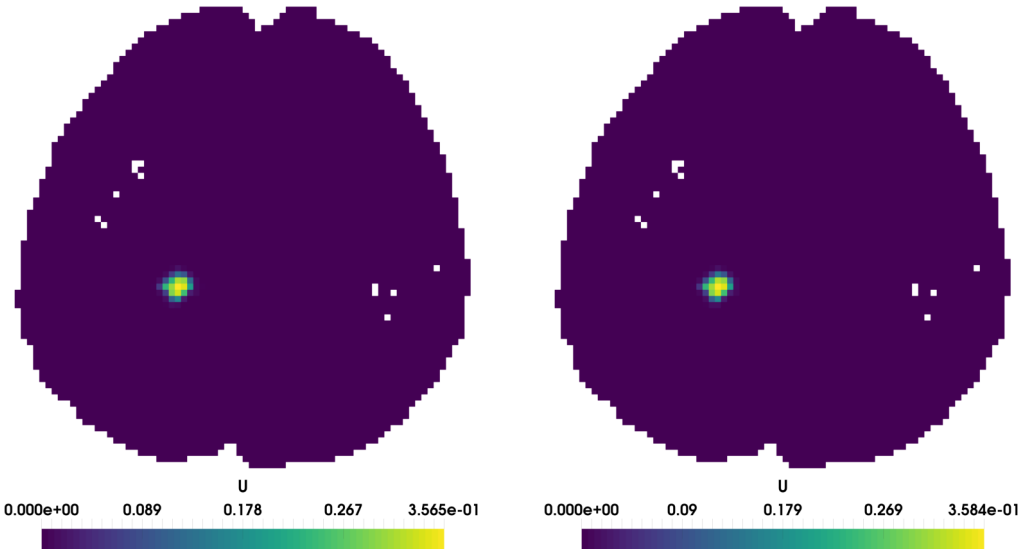

(c) Model (5.5) with only radiotherapy at day 300

(d) Model (5.5) with radiotherapy and concurrent chemotherapy at day 300

Figure 5.1: Simulation results of the model (2.23) described in chapter 2 and the model (5.5) including therapy described in this chapter. Both simulated therapies (only radiotherapy and radiotherapy with concurrent chemotherapy) are effective in the simulation, as the tumour bulk from (b) is reduced drastically. The difference between the simulation outcomes (c) and (d) is more subtle, because we started the therapy immediately with the begin of the simulation and the initial tumour bulk was very small.

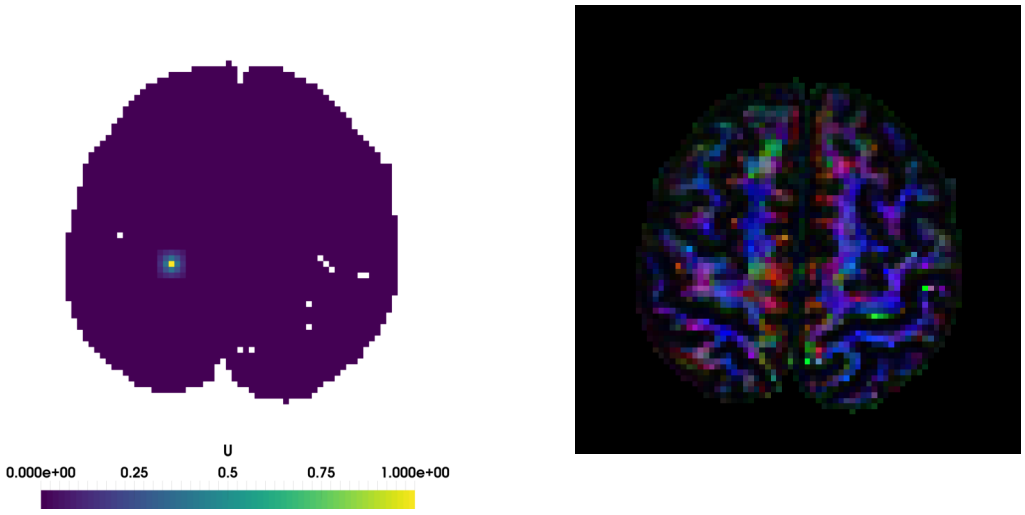

(a) Initial condition on slice 37

(b) Brain structure on slice 37

Figure 5.2: Different initial condition on slice 37 in order to visualize the simulated effectivity of the novel chemotherapy. The image in (a) shows the initial condition and (b) displays the DTI data on this slice.

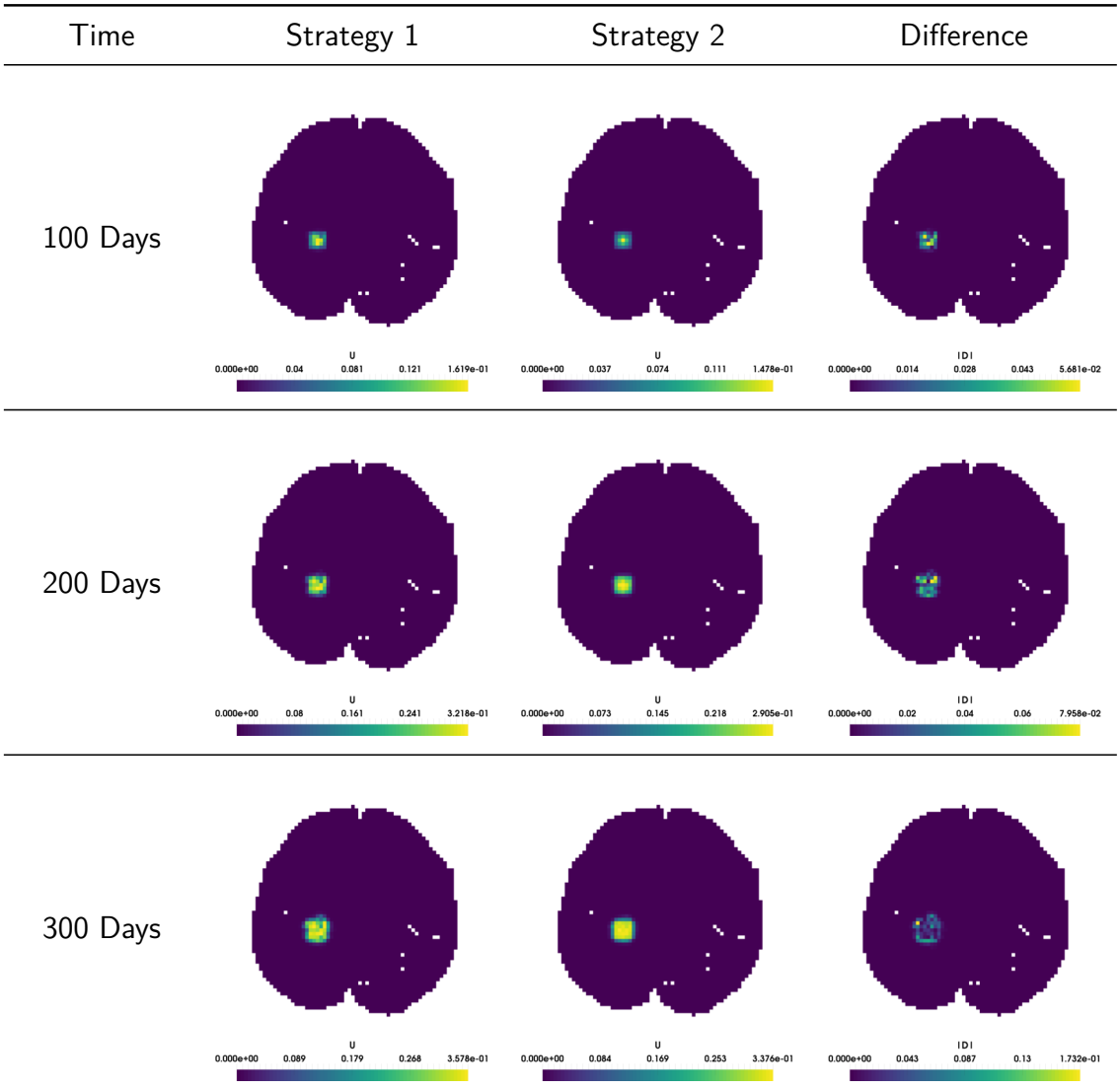

Figure 5.3: Simulations of the different therapy strategies (strategy 1: only radiotherapy, strategy 2: radiotherapy with concurrent chemotherapy) and the difference between both. One can clearly see that the strategy 2 will lead to a smaller and more compact tumour, although therapy is only applied between day 0 and 35.

Chapter 6

Discussion

6.1 Modelling

Multiscale modelling, here based on the previous works [EHKS14, KS12b], enables the combination of substantially different processes into a single model, thus makes it possible to understand cancer migration in greater detail than any single scale model could do. We started from the microscopic cellular scale including sub-cellular dynamics, essential for the migration and proliferation of cells. Here we did not violate physical principles as we used Newton's law of motion. Using averaging procedures, we reached the mesoscopic cell density level, where we modelled proliferation based on recent biological insights. As we need to have a flexible model, we proposed two different stochastic processes promoting migration, the velocity jump process and a Gauß process, both resembling the identical stationary distribution. As the cell densities on the mesoscopic scale involve a high dimensional phase space that is not observable in clinical practice, we employed parabolic scaling in order to extract macroscopic - here spatio-temporal - cell density description, which is well-suited to be used to simulate the evolution of tumour spread into the tissue. We addressed the existence and uniqueness of the relevant model equations.

The main strength of the models presented here is the inclusion of real medical data, not only of high-order detailed data sets, but of generic medical data. So the parameters of the equations (2.23) and (2.40), especially the diffusion tensors D and $\tilde{D}$ therein contain information about the brain structure through the tissue fibre orientation q. Using this medical data, the simulation outcomes resemble existent tumour shapes as seen e. g. in [Hay12], however, a validation of the models presented here is of tremendous importance. On the microscopic scale there is a need to assess cell migration in fibrous networks in detail and to evaluate the behaviour of the cell receptor bindings. This can be used to investigate the driving process and to decide whether a velocity jump process or a Gauß process fits better.

It is also likely that both types are well-suited, but need to be adjusted accordingly. This is not possible without reliable data.

On the mesoscopic scale there is a need to review the proposed proliferation in the light of new biological data. Regarding the growth rate μ, we selected it in a way to find a slightly modified logistic growth, but there are other choices, like e. g. Gompertzian or even exponential growth. Which growth rate is to be preferred is an ongoing debate; it should be assessed from tumour growth data and will surely be specific to different cancer types.

The model validations of the microscopic and mesoscopic scale are of theoretical interest and importance, whereas the validation of the deduced macroscopic description is an urgent need for practical considerations. As we lack time series of patient data, we could not do numerical verification of the results. This is a non-trivial issue, because there is a need for a complete diffusion MRI data set along with a segmentation at an initial time to assess the tumour bulk combined with a segmentation at a later time in order to evaluate the progress. In the best case, there should be no therapy applied in between, a condition seeming quite unrealistic. However, glioblastoma multiforme is sometimes so aggressive that there are cases where no therapy is worth being applied. Moreover, if we restrict ourselves to shorter time intervals (say 1-2 months), data sets without therapy in between do exist and so may be used in the validation process.

Besides the validation of the model, there are some mathematical problems left. So the convergence of the microscopic to the mesoscopic scale and the convergence of the mesoscopic to the macroscopic scale remain for clarification and proof; however, the latter is a non-trivial issue. For a single scale model and a different, much simpler context Chalub et al [CMPS04] proved the convergence in a weak sense, but there is a lot left to do.

For a model extension, there are several parts one may want to add. We modelled the subcellular scale with a single density variable, but due to large variety of cell receptors and their bindings to soluble and unsoluble components on their surrounding as well as mutual cell interactions, it may be necessary to introduce the subcellular scale in the model in another way. Then there are different core features of cell migration left to incorporate: chemotaxis, angiogenesis, and acidity. Chemotaxis can be introduced on the macroscopic scale as an additional drift term along a chemical gradient, either stemming from a time-independent field or from an additional equation in the model, while the introduction of chemotaxis on the mesoscopic or even microscopic scale would lead to novel descriptions. This is not of particular difficulty, when using real data with a voxel size of 2mm, but there are two processes already modelled by other groups, that give rise to problems, when used within a confined resolution:

- **Adhesion**: Cell-cell interactions can lead to correlated or even collective movement in contrary to the single cell movement discussed here. However, the typical incorporation via non-local terms (using sensing radii of the cells) like in the paper [DTGC14] is

problematic with the data available, because the essential sensing radius of maximal $100\ \mu$m is too small compared to a reasonable resolution of the data (around 2 mm side length of a voxel), which just transfers to the resolution of the numerical simulation. So this approach for cell-cell interaction is not possible with existing in-vivo data. Another possibility would be to include the adhesion effect in a hybrid model as in [And05], but with the cost that additional parameters are introduced, what is clearly to avoid, and that the numerical simulations get more involved (and more expensive). Additionally, due to the hybrid nature, the simulation does not stand for an expected value, but only for a single trajectory, giving rise to the question of reliability. So from the viewpoint of data availability none of the approaches known to us can be directly used to incorporate cell-cell adhesion into the multiscale model. Nevertheless cell-cell adhesions may have a remarkable effect on the tumour shape, as noted in [And05, DTGC14].

- **Angiogenesis and nutrient supply**: The formation of new blood vessels at the tumour site is one of the key ingredients for malignancy of a tumour and also metastasis, in brain tumours as well as in all other types of cancer, hence of tremendous importance to include into a mathematical model. While in vivo it is quite clear where a vessel is located, it is incredibly hard to extract this information out of available data. For MRI data there is an algorithm available, that would do this task [KPP$^+$15], but no algorithm can increase the detail; hence for a voxel grid of 2 mm side length, this approach will fail for the fine capillaries that are firstly formed at the tumour site. Nevertheless, one is interested in quantitative information about the nutrients the tumour is provided with, which can be approximated by the blood flow that can be quantified at least for a bit finer data [SRF$^+$08]. This approach may reveal necessary and currently missing information in order to include the effect of angiogenesis and hence of nutrient supply into our model.

  We made the fine distinction between the angiogenesis, namely sprouting and formation of new blood vessels, for which there are several models available [AC98], [HS00] and [MWO04] (all incompatible with the data resolution) and the gross effect of the angiogenesis onto the tumour spread, for which one may not even need to use a variable representing the blood vessels at all. In clinical practice and application only the latter one is of interest and needed.

6.2 Data

We set up a complete working chain ranging from the raw medical data to the personalized numerical simulation on the macroscopic level. To this aim, we relied on the frameworks

Camino and Dune, the missing links were handled with conversion software based on ITK, and the preprocessing toolkit that was used to compute the quantities Q, D, $\tilde{D}$ and U. Most frequent problems like negative eigenvalues of the water diffusion tensor or problems with the segmentation, such as certain voxels containing invalid information, were thereby handled by removing the corresponding voxels of the segmentation. One problem is still to solve: if the diffusion MRI data and the segmentation are given on different, in general non-parallel grids, the code cannot be used, as the transfer of the data between those grids is highly problematic.

We selected estimators for the relevant quantities (Q and q) needed for the simulations. For the fibre orientation q we employed the orientation distribution function (ODF) used in the medical imaging community, which may be estimated from diffusion tensor imaging as well as from high angular resolution imaging data, hence is flexible enough to serve as a building block for further modelling. Moreover, the choice is optimal in the sense that q and ODF are the same quantity, so progress done in estimating ODF directly transfers to a better estimator of q. Nevertheless in future works, the difference of dODF and fODF has to be evaluated in a mathematical modelling framework. We solely used dODF here.

The volume fraction of tissue fibres Q is much more difficult to assess. We introduced a new heuristic estimator, based on diffusion tensor data, but this can be generalized to all mentioned data sets, thus it is also flexible enough for further mathematical modelling frameworks. We demonstrated the strength of the new estimator over the fractional anisotropy proposed in [ALJ$^+$11, EHKS14, EKS16, RMU$^+$13] using a plausibility argument, but a rigorous validation (or disproof) is yet missing, partly due to the extreme difficulty to measure this quantity within the brain.

As all data is inflicted with errors, there may be necessary to use regularization or denoising in order to account for the data error. Recently, a method to denoise full tensors was proposed [BPS16]. Using it has two effects: the data error is minimized and due to the changes in the eigenvalues of the tensors, the numerical simulation behaves better, hence the data smoothing can also be used for accelerating the simulations. This is especially favourable for larger data sets, however, the acceleration is only useful if it does not distort the outcome too much. This will be addressed in forthcoming work.

6.3 Numerics

For the reaction–convection–diffusion equations on the macroscopic level, we set up a numerical method that is able to handle full tensorial diffusion with large differences in the eigenvalues of the diffusion tensor. Moreover, it is locally mass-conservative, hence the discretized convection–diffusion part does not generate nor lose tumour mass. It is also monotone, one of the most crucial, but also most difficult properties to assure. So the numerical method does

not generate negative values and hence the simulation results can be transferred to reality without explaining negative values in a cell density. All in all it is tailored to the problem. The semi–implicit method is fast and thus usable in clinical practice. If one is interested in using a fully implicit method, there is need for parallelization to speed up the computations, as the code we use for the numerical simulation, is at the moment completely serial.

The data preprocessing (estimation of the water diffusion tensors out of the medical data) is very fast and can be done with Camino within half an hour. The processing (estimation of D, $\tilde{D}$ and U) are embarrassingly parallelizable tasks; using enough computational power, this can be done within a day. We parallelized the computation using OpenMP, which is especially well-suited for such tasks. For the data set we used, the estimation of D costs about one and a half minute, whereas estimation of $\tilde{D}$ and U is more intensive, but can be done on a recent computer within one day.

6.4 Therapy

The multiscale model including integrin bindings is especially attractive in view of a new class of chemotherapy targeting the integrin bindings in order to prohibit migration and so the tumour spread. We modelled the therapy carefully, but at the cost of changing the fixed parameters k^+ and k^- to functions depending on the chemotherapy. As foundation, we used another growth model based on the 'go-or-growth' dichotonomy presented in [EKS16] that uses additional, difficult to measure parameters for the starting and stopping of the cells. Of course, the growth may also be modelled by the mesoscopic growth term presented in chapter 2. We still selected the approach via heterogeneity of tumour cell subpopulations, because it is favourable for the inclusion of the novel chemotherapy, as the starting and stopping rates of the cells can be directly modified, which is otherwise not the case. We selected these rates as functions depending on the chemotherapeutic dose intensity. All in all, the therapy model has too many free parameters to use it in clinical practice, but we are looking forward to patient data to evaluate our assumptions and adjust the modelling accordingly.

We did not model resection of the tumour mass (contrary to [HS16]), because the way presented in [HS16] is a computationally perfectly valid approach, but it is unlikely that for this method the required information is available in enough detail. In medical imaging only regions of high cell density are observable, but the complete cell density information is necessary to the resection modelled in [HS16]. Hence further work has to address this issue.

Another desirable model extension, when looking at therapy, is to consider additional chemotherapeutical substances (e.g. temozolomide) aiming at cell death or chemical agents triggering cell sensitization to enhance the overall therapeutic effect of the radiotherapy. This will be done in further work, but careful mathematical modelling will make it feasible to investigate different therapeutic approaches in order to personalize and optimize therapy.

Nevertheless, for this aim, the underlying model has to be validated as previously described in order to generate reliable information.

Bibliography

[Aav02] I. Aavatsmark. An introduction to multipoint flux approximations for quadrilateral grids. *Computational Geosciences*, 6(3-4):405–432, 2002.

[AB05] D. C. Alexander and G. J. Barker. Optimal imaging parameters for fiber-orientation estimation in diffusion MRI. *NeuroImage*, 27(2):357 – 367, 2005.

[AC98] A. R. A. Anderson and M. A. J. Chaplain. Continuous and discrete mathematical models of tumor-induced angiogenesis. *Bulletin of mathematical biology*, 60(5):857–899, 1998.

[ALJ+11] I. Aganj, C. Lenglet, N. Jahanshad, E. Yacoub, N. Harel, P. M. Thompson, and G. Sapiro. A hough transform global probabilistic approach to multiple-subject diffusion MRI tractography. *Medical image analysis*, 15(4):414–425, 2011.

[ALS+10] I. Aganj, C. Lenglet, G. Sapiro, E. Yacoub, K. Ugurbil, and N. Harel. Reconstruction of the orientation distribution function in single- and multiple-shell q-ball imaging within constant solid angle. *Magnetic Resonance in Medicine*, 64(2):554–566, 2010.

[Alt80] W. Alt. Orientation of cells migrating in a chemotactic gradient. *Biological growth and spread*, pages 353–366, 1980.

[And05] A. R. A. Anderson. A hybrid mathematical model of solid tumour invasion: the importance of cell adhesion. *Mathematical Medicine and Biology*, 22(2):163–186, 2005.

[AP08] D. Ambrosi and L. Preziosi. Cell adhesion mechanisms and stress relaxation in the mechanics of tumours. *Biomechanics and Modeling in Mechanobiology*, 8(5):397, 2008.

[ARGQ09] A. R. A. Anderson, K. A. Rejniak, P. Gerlee, and V. Quaranta. Microenvironment driven invasion: a multiscale multimodel investigation. *Journal of mathematical biology*, 58(4-5):579–624, 2009.

[AWLL03] B.-Q. Ai, X.-J. Wang, G.-T. Liu, and L.-G. Liu. Correlated noise in a logistic growth model. *Physical Review E*, 67(2):022903, 2003.

[AZ16] D. Ambrosi and A. Zanzottera. Mechanics and polarity in cell motility. *Physica D: Nonlinear Phenomena*, 330:58 – 66, 2016.

[BB07] M. Blatt and P. Bastian. The iterative solver template library. In Bo Kågström, Erik Elmroth, Jack Dongarra, and Jerzy Waśniewski, editors, *Applied Parallel Computing. State of the Art in Scientific Computing*, volume 4699 of *Lecture Notes in Computer Science*, pages 666–675. Springer, 2007.

[BB08] M. Blatt and P. Bastian. On the generic parallelisation of iterative solvers for the finite element method. *International Journal of Computational Science and Engineering*, 4(1):56–69, 2008.

[BBD+08a] P. Bastian, M. Blatt, A. Dedner, C. Engwer, R. Klöfkorn, R. Kornhuber, M. Ohlberger, and O. Sander. A Generic Grid Interface for Parallel and Adaptive Scientific Computing. Part II: Implementation and Tests in DUNE. *Computing*, 82(2–3):121–138, 2008.

[BBD+08b] P. Bastian, M. Blatt, A. Dedner, C. Engwer, R. Klöfkorn, M. Ohlberger, and O. Sander. A Generic Grid Interface for Parallel and Adaptive Scientific Computing. Part I: Abstract Framework. *Computing*, 82(2–3):103–119, 2008.

[BBNS12] N. Bellomo, A. Bellouquid, J. Nieto, and J. Soler. On the asymptotic theory from microscopic to macroscopic growing tissue models: An overview with perspectives. *Mathematical Models and Methods in Applied Sciences*, 22(01):1130001, 2012.

[BBPSP14] L. Blanchoin, R. Boujemaa-Paterski, C. Sykes, and J. Plastino. Actin dynamics, architecture, and mechanics in cell motility. *Physiological Reviews*, 94(1):235–263, 2014.

[BD08] N. Bellomo and C. Dogbe. On the modelling crowd dynamics from scaling to hyperbolic macroscopic models. *Mathematical Models and Methods in Applied Sciences*, 18(supp01):1317–1345, 2008.

[Bel08] N. Bellomo. *Modeling Complex Living Systems. A Kinetic Theory and Stochastic Game Approach*. Birkhäuser, 2008.

[BG99] M. Berens and A. Giese. "... those left behind." biology and oncology of invasive glioma cells. *Neoplasia*, 1:208–219, 1999.

[BH07] D. J. Brenner and E. J. Hall. Computed tomography — an increasing source of radiation exposure. *New England Journal of Medicine*, 357(22):2277–2284, 2007. PMID: 18046031.

[BHH+95] D. J. Brenner, L. R. Hlatky, P. J. Hahnfeldt, E. J. Hall, and R. K. Sachs. A convenient extension of the linear-quadratic model to include redistribution and reoxygenation. *International Journal of Radiation Oncology - Biology - Physics*, 32(2):379–390, 1995.

[BHM10] P. Bastian, F. Heimann, and S. Marnach. Generic implementation of finite element methods in the distributed and unified numerics environment (dune). *Kybernetika*, 46(2):294–315, 2010.

[BML94] P. J. Basser, J. Mattielo, and D. Lebihan. Estimation of the effective self-diffusion tensor from the nmr spin echo. *Journal of Magnetic Resonance*, 103:247–254, 1994.

[BPS16] R. Bergmann, J. Persch, and G. Steidl. A parallel Douglas–Rachford algorithm for minimizing ROF-like functionals on images with values in symmetric Hadamard manifolds: extended version. *SIAM Journal on Imaging Sciences*, 9(4):901–937, 2016.

[BS15] J. Besserer and U. Schneider. Track-event theory of cell survival with second-order repair. *Radiation and environmental biophysics*, 54(2):167–174, 2015.

[BTZ+05] A. M. Belkin, G. Tsurupa, E. Zemskov, Y. Veklich, J. W. Weisel, and L. Medved. Transglutaminase-mediated oligomerization of the fibrin(ogen) αC domains promotes integrin-dependent cell adhesion and signaling. *Blood*, 105(9):3561–3568, 2005.

[CBG+06] P. A. Cook, Y. Bai, N. S. Gilani, K. K. Seunarine, M. G. Hall, G. J. Parker, and D. C. Alexander. Camino: Open-Source Diffusion-MRI Reconstruction and Processing. In *14th Scientific Meeting of the International Society for Magnetic Resonance in Medicine*, pages 2759+, May 2006.

[CCRW12] M. C. Chamberlain, T. Cloughsey, D. A. Reardon, and P. Y. Wen. A novel treatment for glioblastoma. *Expert Review of Neurotherapeutics*, 12:421–435, 2012.

[CJP05] L.-C. Chang, D. K. Jones, and C. Pierpaoli. Restore: Robust estimation of tensors by outlier rejection. *Magnetic Resonance in Medicine*, 53(5):1088–1095, 2005.

[CMPS04] F. A. C. C. Chalub, P. A. Markowich, B. Perthame, and C. Schmeiser. Kinetic models for chemotaxis and their drift-diffusion limits. In *Nonlinear Differential Equation Models*, pages 123–141. Springer, 2004.

[CS95] M. R. Chicoine and D. L. Silbergeld. Assessment of brain tumor cell motility in vivo and in vitro. *Journal of Neurosurgery*, 82(4):615–622, 1995.

[CS14] M. Cytowski and Z. Szymanska. Large-scale parallel simulations of 3d cell colony dynamics. *Computing in Science & Engineering*, 16(5):86–95, 2014.

[CS15] M. Cytowski and Z. Szymanska. Large-scale parallel simulations of 3d cell colony dynamics: The cellular environment. *Computing in Science & Engineering*, 17(5):44–48, 2015.

[CSD+06] N. Cordes, J. Seidler, R. Durzok, H. Geinitz, and C. Brakebusch. β1-integrin-mediated signaling essentially contributes to cell survival after radiation-induced genotoxic injury. *Oncogene*, 25(9):1378–1390, 2006.

[DC10] J. S. Desgrosellier and D. A. Cheresh. Integrins in cancer: biological implications and therapeutic opportunities. *Nature Reviews Cancer*, 10(1):9–22, 2010.

[Des08] M. Descoteaux. *High angular resolution diffusion MRI: from local estimation to segmentation and tractography (PhD thesis)*. Université Nice Sophia Antipolis, 2008.

[dPGR06] L. G. de Pillis, W. Gu, and A. E. Radunskaya. Mixed immunotherapy and chemotherapy of tumors: modeling, applications and biological interpretations. *Journal of Theoretical Biology*, 238(4):841 – 862, 2006.

[Dro10] J. Droniou. Remarks on discretizations of convection terms in hybrid mimetic mixed methods. *Networks and Heterogeneous Media*, 5(3):545–563, 2010.

[Dro14] J. Droniou. Finite volume schemes for diffusion equations: introduction to and review of modern methods. *Mathematical Models and Methods in Applied Sciences*, 24(08):1575–1619, 2014.

[DTGC14] P. Domschke, D. Trucu, A. Gerisch, and M. A. J. Chaplain. Mathematical modelling of cancer invasion: Implications of cell adhesion variability for tumour infiltrative growth patterns. *Journal of theoretical biology*, 361:41–60, 2014.

[dVDM11] L. B. da Veiga, J. Droniou, and G. Manzini. A unified approach for handling convection terms in finite volumes and mimetic discretization methods for elliptic problems. *IMA journal of numerical analysis*, 31(4):1357–1401, 2011.

[EGH00] R. Eymard, T. Gallouët, and R. Herbin. Finite volume methods. *Handbook of numerical analysis*, 7:713–1018, 2000.

[EHKS14] C. Engwer, T. Hillen, M. Knappitsch, and C. Surulescu. Glioma follow white matter tracts: a multiscale dti-based model. *Journal of Mathematical Biology*, 71(3):551–582, 2014.

[EHS15] C. Engwer, A. Hunt, and C. Surulescu. Effective equations for anisotropic glioma spread with proliferation: a multiscale approach and comparisons with previous settings. *Mathematical Medicine and Biology*, 2015.

[EKS16] C. Engwer, M. Knappitsch, and C. Surulescu. A multiscale model for glioma spread including cell-tissue interactions and proliferation. *Mathematical Biosciences and Engineering*, 13(2):443–460, 2016.

[EO05] R. Erban and H. Othmer. From signal transduction to spatial pattern formation in *e. coli*: a paradigm for multiscale modeling in biology. *Multiscale Modeling and Simulation*, 3(2):362–394, 2005.

[ESZ09] A. Ern, A. F. Stephansen, and P. Zunino. A discontinuous galerkin method with weighted averages for advection–diffusion equations with locally small and anisotropic diffusivity. *IMA Journal of Numerical Analysis*, 29(2):235–256, 2009.

[FBZ+16] M. T. Freitag, S. Bickelhaupt, C. Ziener, K. Meier-Hein, J. P. Radtke, J. Mosebach, T.-A. Kuder, H.-P. Schlemmer, and F. B. Laun. Selected clinically established and scientific techniques of diffusion-weighted MRI. *Der Radiologe*, 56(2):137–147, 2016.

[FCF+07] C. D. Fuller, M. Choi, B. Forthuber, S. J. Wang, N. Rajagiriyil, B. J. Salter, and M. Fuss. Standard fractionation intensity modulated radiation therapy (imrt) of primary and recurrent glioblastoma multiforme. *Radiation Oncology*, 2(1):26, 2007.

[FFB+07] F. B. Furnari, T. Fenton, R. M. Bachoo, A. Mukasa, J. M. Stommel, A. Stegh, W. C. Hahn, K. L. Ligon, D. N. Louis, C. Brennan, et al. Malignant astrocytic glioma: genetics, biology, and paths to treatment. *Genes & development*, 21(21):2683–2710, 2007.

[FM12] W. Freeden and V. Michel. *Multiscale potential theory: with applications to geoscience*. Springer Science & Business Media, 2012.

[Fre12] W. Freeden. *Green's Function Oriented Numerical Integration*. Technische Universität Kaiserslautern, 2012.

[FS08] W. Freeden and M. Schreiner. *Spherical functions of mathematical geosciences: a scalar, vectorial, and tensorial setup*. Springer Science & Business Media, 2008.

[GBBW03] A. Giese, R. Bjerkvig, M. E. Behrens, and M. Westphal. Cost of migration: invasion of malignant gliomas and implications for treatment. *Journal of Clinical Oncology*, 21(8):1624–1636, 2003.

[gdc16] Gdcm web site, 2016. http://gdcm.sourceforge.net.

[GG04] W. Guo and F. G. Giancotti. Integrin signalling during tumour progression. *Nature reviews Molecular cell biology*, 5(10):816–826, 2004.

[GKL+96] A. Giese, L. Kluwe, B. Laube, H. Meissner, M. E. Berens, and M. Westphal. Migration of human glioma cells on myelin. *Neurosurgery*, 38(4):755–764, 1996.

[GO04] M. E. Gracheva and H. G. Othmer. A continuum model of motility in ameboid cells. *Bulletin of Mathematical Biology*, 66(1):167–193, 2004.

[GW96] A. Giese and M. Westphal. Glioma invasion in the central nervous system. *Neurosurgery*, 39(2):235–252, 1996.

[Hay12] M. A. Hayat. *Tumors of the central nervous system*. Springer, 2012.

[HCS+12] C. H. Holdsworth, D. Corwin, R. D. Stewart, R. Rockne, A. D. Trister, K. R. Swanson, and M. Phillips. Adaptive imrt using a multiobjective evolutionary algorithm integrated with a diffusion–invasion model of glioblastoma. *Physics in medicine and biology*, 57(24):8271, 2012.

[HES+08] K. S. Hoek, O. M. Eichhoff, N. C. Schlegel, U. Döbbeling, N. Kobert, L. Schaerer, S. Hemmi, and R. Dummer. In vivo switching of human melanoma cells between proliferative and invasive states. *Cancer research*, 68(3):650–656, 2008.

[HHB+07] S. Höhme, J. G. Hengstler, M. Brulport, M. Schäfer, A. Bauer, R. Gebhardt, and D. Drasdo. Mathematical modelling of liver regeneration after intoxication with CCl4. *Chemico-Biological Interactions*, 168(1):74 – 93, 2007. Hepatocytes and Drug Development.

[HHW10] T Hillen, P. Hinow, and Z. A. Wang. Mathematical analysis of a kinetic model for cell movement in network tissues. *Discrete & Continuous Dynamical Systems - B*, 14(1531-3492_2010_3_1055):1055, 2010.

[Hil05] T. Hillen. On the l^2-moment closure of transport equations: The general case. *Discrete & Continuous Dynamical Systems - B*, 5(1531-3492_2005_2_299):299, 2005.

[Hil06] T. Hillen. M5 mesoscopic and macroscopic models for mesenchymal motion. *Journal of mathematical biology*, 53(4):585–616, 2006.

[HNRW15] R. Y. Huang, M. R. Neagu, D. A. Reardon, and P. Y. Wen. Pitfalls in the neuroimaging of glioblastoma in the era of antiangiogenic and immuno/targeted therapy–detecting illusive disease, defining response. *Frontiers in neurology*, 6:33, 2015.

[HP13] T. Hillen and K. J. Painter. Transport and anisotropic diffusion models for movement in oriented habitats. In *Dispersal, individual movement and spatial ecology*, pages 177–222. Springer, 2013.

[HS00] M. J. Holmes and B. D. Sleeman. A mathematical model of tumour angiogenesis incorporating cellular traction and viscoelastic effects. *Journal of theoretical biology*, 202(2):95–112, 2000.

[HS16] A. Hunt and C. Surulescu. A multiscale modeling approach to glioma invasion with therapy. *Vietnam Journal of Mathematics*, pages 221–240, 2016.

[HW00] D. Hanahan and R. A. Weinberg. The hallmarks of cancer. *Cell*, 100(1):57 – 70, 2000.

[HW03] R. Horwitz and D. Webb. Cell migration. *Current Biology*, 13(19):R756 – R759, 2003.

[HW11] D. Hanahan and R. A. Weinberg. Hallmarks of cancer: the next generation. *Cell*, 144(5):646–674, 2011.

[HWRB75] T. Hoshino, C. B. Wilson, M. L. Rosenblum, and M. Barker. Chemotherapeutic implications of growth fraction and cell cycle time in glioblastomas. *Journal of neurosurgery*, 43(2):127–135, 1975.

[ITK16] Itk - insight segmentation and registration toolkit, 2016. http://www.itk.org/.

[JB04] D. K. Jones and P. J. Basser. "squashing peanuts and smashing pumpkins": How noise distorts diffusion-weighted mr data. *Magnetic Resonance in Medicine*, 52(5):979–993, 2004.

[JJHD+15] P. R. Jackson, J. Juliano, A. Hawkins-Daarud, R. C. Rockne, and K. R. Swanson. Patient-specific mathematical neuro-oncology: using a simple proliferation and invasion tumor model to inform clinical practice. *Bulletin of mathematical biology*, 77(5):846–856, 2015.

[JKT13] D. K. Jones, T. R. Knösche, and R. Turner. White matter integrity, fiber count, and other fallacies: The do's and don'ts of diffusion MRI. *NeuroImage*, 73:239 – 254, 2013.

[JMD+05] S. Jbabdi, E. Mandonnet, H. Duffau, L. Capelle, K. R. Swanson, M. Pelegrini-Issac, R. Guillevin, and H. Benali. Diffusion tensor imaging allows anisotropic growth simulations of low grade gliomas. *Magnetic Resonance in Medicine*, 54:616–624, 2005.

[KIN+01] K. Kono, Y. Inoue, K. Nakayama, M. Shakudo, M. Morino, K. Ohata, K. Wakasa, and R. Yamada. The role of diffusion-weighted imaging in patients with brain tumors. *American Journal of Neuroradiology*, 22(6):1081–1088, 2001.

[KMM08] J. P. Kirkpatrick, J. J. Meyer, and L. B. Marks. The linear-quadratic model is inappropriate to model high dose per fraction effects in radiosurgery. In *Seminars in radiation oncology*, volume 18, pages 240–243. Elsevier, 2008.

[KPP+15] J. Kubicek, M. Penhaker, K. Pavelova, A. Selamat, R. Hudak, and J. Majernik. *Segmentation of MRI Data to Extract the Blood Vessels Based on Fuzzy Thresholding*, pages 43–52. Springer International Publishing, Cham, 2015.

[KS12a] I. Karatzas and S. Shreve. *Brownian motion and stochastic calculus*. Springer Science & Business Media, 2012.

[KS12b] J. Kelkel and C. Surulescu. A multiscale approach to cell migration in tissue networks. *Mathematical Models and Methods in Applied Sciences*, 23(3), 2012.

[LBMP+01] D. Le Bihan, J.-F. Mangin, C. Poupon, C. A. Clark, S. Pappata, N. Molko, and H. Chabriat. Diffusion tensor imaging: concepts and applications. *Journal of magnetic resonance imaging*, 13(4):534–546, 2001.

[LL93] D. A. Lauffenburger and J. Linderman. *Receptors: models for binding, trafficking, and signaling*. Oxford University Press, 1993.

[LMS14] K. Lipnikov, G. Manzini, and M. Shashkov. Mimetic finite difference method. *Journal of Computational Physics*, 257:1163–1227, 2014.

[LS14] T. Lorenz and C. Surulescu. On a class of multiscale cancer cell migration models: Well-posedness in less regular function spaces. *Mathematical Models and Methods in Applied Sciences*, 24(12):2383–2436, 2014.

[MBFVP94] M. Marušić, Ž. Bajzer, J. P. Freyer, and S. Vuk-Pavlović. Analysis of growth of multicellular tumour spheroids by mathematical models. *Cell proliferation*, 27(2):73–94, 1994.

[MBG+06] R. M. H. Merks, S. V. Brodsky, M. S. Goligorksy, S. A. Newman, and J. A. Glazier. Cell elongation is key to in silico replication of in vitro vasculogenesis and subsequent remodeling. *Developmental biology*, 289(1):44–54, 2006.

[mri16] Mricron web site, 2016. http://people.cas.sc.edu/rorden/mricron/index.html.

[MRP+05] R.-H. Mattern, S. B. Read, M. D. Pierschbacher, C.-I Sze, B. P. Eliceri, and C. A. Kruse. Glioma cell integrin expression and their interactions with integrin antagonists. *Cancer Therapy*, 3A:325–340, 2005.

[MWO04] V. N. Mantzaris, S. Webb, and G. H. Othmer. Mathematical modeling of tumor-induced angiogenesis. *Journal of Mathematical Biology*, 49(2):111–187, 2004.

[Nel67] E. Nelson. *Dynamical theories of Brownian motion*, volume 2. Princeton university press, 1967.

[nif12] Niftilib web site, 2012. http://niftilib.sourceforge.net.

[NP12] N. C. Nguyen and J. Peraire. Hybridizable discontinuous galerkin methods for partial differential equations in continuum mechanics. *Journal of Computational Physics*, 231(18):5955–5988, 2012.

[NPC09] N. C. Nguyen, J. Peraire, and B. Cockburn. An implicit high-order hybridizable discontinuous galerkin method for linear convection–diffusion equations. *Journal of Computational Physics*, 228(9):3232–3254, 2009.

[NRR16] Libteem NRRD web page, 2016. http://teem.sourceforge.net/nrrd.

[NU16] J. Nieto and L. Urrutia. A multiscale model of cell mobility: From a kinetic to a hydrodynamic description. *Journal of Mathematical Analysis and Applications*, 433(2):1055–1071, 2016.

[Oel91] K. Oelschläger. On the connection between hamiltonian many-particle systems and the hydrodynamical equations. *Archive for rational mechanics and analysis*, 115(4):297–310, 1991.

[OGR+03] N. B. Ouchi, J. A. Glazier, J.-P. Rieu, A. Upadhyaya, and Y. Sawada. Improving the realism of the cellular potts model in simulations of biological cells. *Physica A: Statistical Mechanics and its Applications*, 329(3–4):451 – 458, 2003.

[Ope16] OpenMP webpage, 2016. http://http://openmp.org/wp/.

[PD99] C. A. Parent and P. N. Devreotes. A cell's sense of direction. *Science*, 284(5415):765–770, 1999.

[PDY09] R. J. Petrie, A. D. Doyle, and K. M. Yamada. Random versus directionally persistent cell migration. *Nature Reviews Molecular Cell Biology*, 10(8):538–549, 2009.

[PH13] K. J. Painter and T. Hillen. Mathematical modelling of glioma growth: the use of diffusion tensor imaging (dti) data to predict the anisotropic pathways of cancer invasion. *Journal of theoretical biology*, 323:25–39, 2013.

[RAJRS09] R. Rockne, E. C. Alvord Jr, J. K. Rockhill, and K. R. Swanson. A mathematical model for brain tumor response to radiation therapy. *Journal of mathematical biology*, 58(4-5):561–578, 2009.

[Rie03] A. Rieder. *Keine Probleme mit Inversen Problemen: Eine Einführung in ihre stabile Lösung*. Vieweg & Teubner Verlag, 2003.

[RK08] B. M. Rubenstein and L. J. Kaufman. The role of extracellular matrix in glioma invasion: A cellular potts model approach. *Biophysical Journal*, 95(12):5661 – 5680, 2008.

[RKD11] M. Reiser, F.-P. Kuhn, and J. Debus. *Radiologie*. Thieme, 2011.

[RMU+13] M. Reisert, I. Mader, R. Umarova, S. Maier, L. Tebartz van Elst, and V. G. Kiselev. Fiber density estimation from single q-shell diffusion imaging by tensor divergence. *NeuroImage*, 77:166 – 176, 2013.

[RR06] M. Renardy and R. C. Rogers. *An introduction to partial differential equations*, volume 13. Springer Science & Business Media, 2006.

[RRM+10] R. Rockne, J. K. Rockhill, M. Mrugala, A. M. Spence, I. Kalet, K. Hendrickson, A. Lai, T. Cloughesy, E. C. Alvord Jr, and K. R. Swanson. Predicting the

efficacy of radiotherapy in individual glioblastoma patients in vivo: a mathematical modeling approach. *Physics in medicine and biology*, 55(12):3271, 2010.

[Ruz06] M. Ruzicka. *Nichtlineare Funktionalanalysis: Eine Einführung*. Springer-Verlag, 2006.

[SAM03] K. R. Swanson, E. C. Alvord, and J. D. Murray. Modeling and simulation of tumor development, treatment, and control virtual resection of gliomas: Effect of extent of resection on recurrence. *Mathematical and Computer Modelling*, 37(11):1177 – 1190, 2003.

[SBMA03] K. R. Swanson, C. Bridge, J. D. Murray, and E. C. Alvord. Virtual and real brain tumors: using mathematical modeling to quantify glioma growth and invasion. *Journal of the neurological sciences*, 216(1):1–10, 2003.

[SC+12] T. Scarabino, F. Caranci, et al. *Imaging Gliomas After Treatment*. Springer, 2012.

[SC16] C. Sanderson and R. Curtin. Armadillo: a template-based c++ library for linear algebra. *Journal of Open Source Software*, 2016.

[Sho11] R. E. Showalter. *Hilbert space methods in partial differential equations*. Courier Corporation, 2011.

[Sho13] R. E. Showalter. *Monotone operators in Banach space and nonlinear partial differential equations*, volume 49. American Mathematical Soc., 2013.

[SLR12] D. Shao, H. Levine, and W.-J. Rappel. Coupling actin flow, adhesion, and morphology in a computational cell motility model. *Proceedings of the National Academy of Sciences*, 109(18):6851–6856, 2012.

[SMAC05] A. Stéphanou, S. R. McDougall, A. R. A. Anderson, and M. A. J. Chaplain. Modelling complex systems in molecular biology and tumor dynamics and control mathematical modelling of flow in 2d and 3d vascular networks: Applications to anti-angiogenic and chemotherapeutic drug strategies. *Mathematical and Computer Modelling*, 41(10):1137 – 1156, 2005.

[SMvdB+05] R. Stupp, W. P. Mason, M. J. van den Bent, M. Weller, B. Fisher, M. J. B. Taphoorn, K. Belanger, A. A. Brandes, C. Marosi, U. Bogdahn, J. Curschmann, R. C. Janzer, S. K. Ludwin, T. Gorlia, A. Allgeier, D. Lacombe, J. G. Cairncross, E. Eisenhauer, and R. O. Mirimanoff. Radiotherapy plus concomitant and

adjuvant temozolomide for glioblastoma. *New England Journal of Medicine*, 352(10):987–996, 2005. PMID: 15758009.

[SP12] M. Scianna and L. Preziosi. Multiscale developments of the cellular potts model. *Multiscale Modeling & Simulation*, 10(2):342–382, 2012.

[SRD+07] S. Sathornsumetee, D. A. Reardon, A. Desjardins, J. A. Quinn, J. J. Vredenburgh, and J. N. Rich. Molecularly targeted therapy for malignant glioma. *Cancer*, 110(1):13–24, 2007.

[SRF+08] A. F. Stalder, M. F. Russe, A. Frydrychowicz, J. Bock, J. Hennig, and M. Markl. Quantitative 2d and 3d phase contrast MRI: optimized analysis of blood flow and vessel wall parameters. *Magnetic resonance in medicine*, 60(5):1218–1231, 2008.

[SS10] C. Surulescu and N. Surulescu. A nonparametric approach to cells dispersal. *International Journal of Biomathematics and Biostatistics*, 1:109–128, 2010.

[SS11] C. Surulescu and N. Surulescu. Modeling and simulation of some cell dispersion problems by a nonparametric method. *Mathematical Biosciences & Engineering*, 8:263–277, 2011.

[SSS02] F. A. Stewart, M. I. Saunders, and G. G. Steel. Basic clinical radiobiology. *Basic clinical radiobiology*, 2002.

[Ste00] A. Stevens. The derivation of chemotaxis equations as limit dynamics of moderately interacting stochastic many-particle systems. *SIAM Journal on Applied Mathematics*, 61(1):183–212, 2000.

[SV07] D. W. Stroock and S. R. S. Varadhan. *Multidimensional diffusion processes*. Springer, 2007.

[Tuc04] D. S. Tuch. Q-ball imaging. *Magnetic Resonance in Medicine*, 52(6):1358–1372, 2004.

[UdJPK09] T. A. Ulrich, E. M. de Juan Pardo, and S. Kumar. The mechanical rigidity of the extracellular matrix regulates the structure, motility, and proliferation of glioma cells. *Cancer Research*, 69:4167–4174, 2009.

[UGR99] J. H. Uhm, C. L. Gladson, and J. S. Rao. The role of integrins in the malignant phenotype of gliomas. *Frontiers in Bioscience*, 4:d188–199, 1999.

[Uni15] Unidata. Network common data form (netcdf) version 4.3.3.1 [software], 2015.

[VA82] V. G. Vaidya and F. J. Alexandro. Evaluation of some mathematical models for tumor growth. *International journal of bio-medical computing*, 13(1):19–35, 1982.

[Var66] S. R. S. Varadhan. Asymptotic probabilities and differential equations. *Communications on Pure and Applied Mathematics*, 19(3):261–286, 1966.

[WO16] Q. Wang and H. G. Othmer. Computational analysis of amoeboid swimming at low reynolds number. *Journal of mathematical biology*, 72(7):1893–1926, 2016.

[WSP+14] C. Weber, B. Stieltjes, J. Polanska, F. Binczyck, R. Tamawski, B. Bobek-Bilewicz, T. Rodi, S. Regnery, and K. H. Maier-Hein. Tumor progression mapping: An intuitive visualization of glioblastoma progression in mr follow-ups. *Proceedings of Annual Meeting ISMRM.*, 2014.

[Yag09] A. Yagi. *Abstract parabolic evolution equations and their applications*. Springer Science & Business Media, 2009.

[YJDS15] R. M. Young, A. Jamshidi, G. Davis, and J. H. Sherman. Current trends in the surgical management and treatment of adult glioblastoma. *Annals of Translational Medicine*, 3(9), 2015.

[ZSH] A. Zhigun, C. Surulescu, and A. Hunt. A strongly degenerate diffusion-haptotaxis model of tumour invasion under the go-or-grow dichotomy hypothesis. *Mathematical Methods in the Applied Sciences*, 41(6):2403–2428.

[ZSU16] A. Zhigun, C. Surulescu, and A. Uatay. Global existence for a degenerate haptotaxis model of cancer invasion. *Zeitschrift für angewandte Mathematik und Physik*, 67(6):146, 2016.

Erklärung

Ich versichere hiermit, dass ich die vorliegende Arbeit mit dem Titel „DTI-Based Multiscale Models for Glioma Invasion“ selbstständig und ohne Benutzung anderer als der angegebenen Quellen und Hilfsmittel angefertigt habe.
Teile dieser Arbeit sind inhaltlich in den Veröffentlichungen
„Effective equations for anisotropic glioma spread with proliferation: a multiscale approach and comparisons with previous settings“ von Christian Engwer, A. H. und Christina Surulescu, Oxford Journal of Mathematical Medicine and Biology (2015)
und
„A Multiscale Modeling Approach to Glioma Invasion with Therapy“ von A. H. und Christina Surulescu, Vietnam Journal of Mathematics (2016)
erschienen.

Alexander Hunt
Kaiserslautern, den 19. Juli 2017

Wissenschaftlicher Werdegang

Oktober 2013 – November 2017	Promotion in Mathematik Technische Universität Kaiserslautern
Oktober 2008 – September 2013	Studium Mathematik Technische Universität Kaiserslautern (September 2011: Bachelor of Science) (September 2013: Master of Science)
März 2008	Allgemeine Hochschulreife Hohenstaufengymnasium Kaiserslautern

Curriculum Vitae

October 2013 – November 2017	Doctoral course in Mathematics Technische Universität Kaiserslautern
October 2008 – September 2013	Study in Mathematics Technische Universität Kaiserslautern (September 2011: Bachelor of Science) (September 2013: Master of Science)
March 2008	Abitur Hohenstaufengymnasium Kaiserslautern